Global Time Echoes: Raw RINEX Consistency Test

Matthew Lukin Smawfield

Version: v0.6 (Kathmandu)

05 June 2026

DOI: 10.5281/zenodo.17860166

Code Availability: github.com/matthewsmawfield/TEP-GNSS-RINEX

Abstract

This paper validates that distance-structured correlations in GNSS clocks exist in raw observations using broadcast ephemerides, not just precise products—strongly constraining precise-product processing artifacts. Broadcast ephemerides still contain control-segment information, so Satellite Laser Ranging and non-GNSS optical checks remain necessary for definitive confirmation. Prior TEP analyses relied on precise orbit and clock products from global analysis centers, leaving open the possibility that observed signatures were artifacts of sophisticated processing chains. This paper addresses that concern by detecting distance-structured signatures in raw GNSS observations processed using Single Point Positioning (SPP) with broadcast ephemerides as the primary methodology, supplemented by precise ephemeris validation. Analysis of 539 globally distributed stations over 3 years (2022–2024, comprising 1.17 billion pair-samples across three independent filtering strategies) achieves consistent signal detection across all 72 metric combinations with mean $R^2 = 0.93$, revealing directionally-structured correlations consistent with CODE's 25-year PPP findings ($p < 10^{-15}$). The 72 metric combinations are not statistically independent; they are treated as consistency checks across processing modes and observables.

The primary finding is directional anisotropy: East-West correlations are 2–5% (MSC) to 22% (Phase Alignment) stronger than North-South at short distances (<500 km), with t-statistics up to 112 and Cohen's d up to 0.304. Month-by-month stratification shows stable polarity (E-W > N-S) at 94% or higher level across modes and metrics (worst case 34/36 months), consistent with a persistent underlying effect. A critical audit indicates this is not an artifact of distance distribution: E-W pairs are actually 13 km longer than N-S pairs (bias against signal), and robust distance-matching strengthens the ratio (1.033 → 1.041). At full distances, raw λ ratios can appear suppressed by distance-dependent biases; a geometry-corrected comparison yields ratios of 1.80–1.86, within 17% of CODE's benchmark (2.16).

Key validations include: (1) orbital velocity coupling detected at 3.2–5.4σ (best: $r = -0.763$), replicating CODE's 25-year finding ($r = -0.888$), with signal persisting under ionospheric removal (best ionofree: $r = -0.416$, 2.5σ); (2) position jitter and clock bias show similar orbital coupling ($\Delta \approx 5\%$), consistent with spacetime—not just temporal—modulation; (3) CMB frame alignment at RA = 188°, Dec = −5° (20.0° from CMB dipole), matching CODE's benchmark (18.2°), with Solar Apex disfavored (86.5° separation); (4) geomagnetic stratification using real GFZ Kp data shows near-invariance at the primary

threshold (Kp < 3 vs. Kp ≥ 3; median $\Delta\lambda \approx -1\%$, with 60/72 tests within ±5% across all station filters and processing modes), while higher storm thresholds (Kp ≥ 4/5) are treated as sensitivity checks due to small storm-day counts; (5) hemisphere-stratified results show E-W > N-S in the ALL_STATIONS analysis, while higher-quality subsets motivate additional hemisphere-controlled falsification tests; (6) year-specific planetary event modulation detected (2.8× above null, $p < 0.001$ for all 6 metrics) with detection rates of 59–68% and no consistent tidal GM/r^2 scaling (σ-level vs GM/r^2: $p = 0.317–0.989$), consistent with alignment-driven geometric coupling rather than a tidal forcing mechanism whose amplitude scales with planetary mass.

This paper constitutes Paper 3 of the TEP-GNSS Research Series. Together with Paper 1 (multi-center validation) and Paper 2 (25-year temporal stability), these three complementary analyses—using different data sources, processing chains, and time periods—provide consistent evidence for planetary-scale, directionally-structured correlations in GNSS clock measurements. The observed signature of spacetime symmetry, CMB alignment, and orbital velocity dependence is consistent with the Temporal Equivalence Principle hypothesis, which preserves local Lorentz invariance while predicting global path-dependent synchronization. Independent replication by external research groups remains essential.

Executive Summary

Research Question

Prior TEP analyses (Papers 1 and 2) relied on precise orbit and clock products from global analysis centers. Since these products are derived using complex network adjustments and integer ambiguity resolution, a critical ambiguity remained:

"Are the observed signatures artifacts of the processing chain, or do they exist in the raw observations?"

This study addresses this question. By analyzing raw RINEX pseudorange measurements processed via Single Point Positioning (SPP) primarily with broadcast ephemerides (supplemented by precise ephemeris validation), the results indicate that the same directional anisotropy, orbital velocity coupling, and CMB-frame alignment are present in the fundamental data. This is consistent with, but not decisive proof of, the observed structure not being solely a byproduct of precise product generation.

Key Findings

- **Raw Data Validation:** Distance-structured signatures detected in raw RINEX data using only broadcast ephemerides and Single Point Positioning. Analysis of 539 stations over 3 years (1.17 billion pair-samples) achieves signal-consistent structure in all 72 tested metric combinations with directional anisotropy matching CODE's 25-year findings ($p < 10^{-15}$).
- **Consistent Detection across all Metrics:** Signal consistent with TEP detected in all 72 non-independent metric combinations used as consistency checks across processing modes and observables (3 station filters × 4 processing modes × 3 observables × 2 coherence types). Mean $R^2 = 0.93$, with all fits exceeding the 0.5 threshold.
- **Directional Anisotropy:** E-W correlations are 2–5% (MSC) to 22% (Phase Alignment) stronger than N-S at short distances (<500 km), matching CODE's directional signature with $p < 10^{-15}$. A critical distance audit reveals E-W pairs are 13 km longer than N-S pairs (a bias *against* the signal); robust distance-matching strengthens the coherence ratio from 1.033 to 1.041.
- **Multi-Mode Validation:** Signal detected in GPS-only (ratio 1.033), dual-frequency ionofree (1.019), and multi-GNSS (1.050).
- **Geometry-Corrected Match:** Full-distance λ_T ratios, after correcting for GPS orbital suppression, converge to 1.80–1.86, within 17% of CODE's 25-year PPP reference (2.16).
- **Geomagnetic Independence:** Primary Kp stratification (Kp<3 vs Kp≥3) shows near-invariance (median $\Delta\lambda_T \approx -1\%$, 60/72 tests within ±5% across filters/modes/metrics).

- **Hemisphere Stratification:** In the ALL_STATIONS analysis, both hemispheres show E-W > N-S (phase alignment 1.200/1.348).
- **Orbital Velocity Coupling:** E-W/N-S anisotropy ratio anti-correlates with Earth's orbital velocity. Multi-GNSS yields the strongest detection: r = −0.763, 5.4σ (pos_jitter/phase), with MSC yielding r = −0.610, 4.0σ.
- **Robust Cross-Filter Consistency:** All three station filtering methods (ALL_STATIONS, OPTIMAL_100, DYNAMIC_50) produce consistent Temporal Topology correlation lengths with CV < 15%.
- **Ionofree Best Estimate:** The ionofree mode (λ_T = 1,069 km, R^2 = 0.969) provides the most precise estimate of the underlying Temporal Topology correlation length.
- **Altitude Independence:** Correlation length is independent of station altitude. Across 360 regressions spanning global and latitude-controlled altitude quintiles, only 3.1% show $p < 0.05$ slopes.
- **Ionofree Phase $\lambda_T \approx$ CODE (2024):** The 2024 OPTIMAL_100 Ionofree pos_jitter/phase alignment yields $\lambda_T = 4{,}767 \pm 835$ *km*, statistically consistent with CODE's 25-year benchmark (4,201 ± 1,967 km).
- **Temporal Stability:** Across the full 72-channel year-by-year grid (3 filters × 4 modes × 3 metrics × 2 coherence types), 66/72 channels have year-to-year CV < 20%.
- **Monthly Anisotropy Consistency:** Month-by-month short-distance anisotropy shows stable polarity (E-W > N-S) at 94% or higher level across modes and metrics.
- **Seasonal Stability:** Comprehensive seasonal stratification reveals three complementary signatures: (1) "Summer Enhancement", (2) "Invariant Core", and (3) "Network-wide Baseline".
- **Null Tests Passed:** Comprehensive validation across 72 combinations constrains several alternative explanations: (1) Solar rotation shows zero correlation, (2) Lunar tides show zero correlation, and (3) Shuffle test demonstrates real structure.
- **Metric Complementarity:** MSC excels at detecting temporal modulation, while phase alignment excels at spatial structure.
- **Planetary Event Modulation:** Year-specific coherence modulation detected around 37 planetary conjunction/opposition events with 2.8× higher detection rates than permutation null controls.
- **CMB Frame Alignment:** Comprehensive 72-combination full-sky grid search yields results consistent with the CODE 25-year benchmark.
- **Large-Scale Dataset:** 1.17 billion pair-samples analyzed across all filters.

Significance of Results

The detection of directionally structured correlations in raw RINEX data, processed with only broadcast ephemerides, addresses a key alternative hypothesis: that TEP signals are artifacts of precise product generation.

By analyzing the fundamental observables to the rawest observables, this analysis shows that the signal is not evidently a fragile artifact of sophisticated processing, but a robust feature of the data itself—a baseline correlation that remains under conservative preprocessing.

This represents a third complementary line of evidence for TEP:

1. **Paper 1:** Multi-center validation (CODE, ESA, IGS) — supports the interpretation that the signal is not center-specific
2. **Paper 2:** 25-year CODE analysis — supports temporal persistence within the analyzed interval
3. **Paper 3 (This Paper):** Raw RINEX consistency test — supports the interpretation that the signal is not solely a processing artifact

Together, these three complementary analyses provide consistent evidence for distance-structured correlations in GNSS clock measurements. Independent replication by external research groups remains essential to assess programme-specific systematics.

Methodology Highlights

- **Data Source:** NASA CDDIS archive — raw RINEX 3.x observation files
- **Processing:** RTKLIB Single Point Positioning with broadcast ephemerides (primary) and precise ephemerides (validation)
- **Time Alignment:** Pandas DatetimeIndex alignment (identical to CODE longspan methodology)
- **Coherence:** Magnitude-weighted phase coherence via cross-spectral density
- **Fitting:** Inverse-variance weighted exponential decay: C(r) = A·exp(-r/λ) + C_0

Conclusion

This paper provides raw-data validation of TEP signatures. The unified signature of spacetime symmetry, CMB alignment, and orbital velocity dependence suggests that the observed correlations may not be purely instrumental, but could reflect a coupling between clocks and the spacetime metric through which Earth moves. The observed breakdown of global simultaneity (CMB alignment) is consistent with the Bi-Metric Geometry framework (Smawfield, 2025), which preserves local Lorentz invariance while predicting global path-dependent synchronization.

Related: Paper 1 (Multi-Center) · Paper 2 (25-Year CODE)

1. Introduction: The TEP Research Program

1.1 The Theoretical Hypothesis

The Temporal Equivalence Principle (TEP) represents a proposed extension to the foundations of General Relativity, positing a fundamental coupling between spatial and temporal fluctuations in geodetic measurements. Formulated within a Bi-Metric Geometry framework (TEP v0.7, Jakarta; Smawfield, 2025), the theory employs continuous geometric screening rather than discrete thin-shell approximations: the scalar time field exhibits a spatially varying Temporal Topology, and its gradient (Temporal Shear) drives the observable Temporal Shear response that manifests as synchronized fluctuations in the rate of proper time flow across spatially separated atomic clocks. High ambient density flattens this topology, suppressing the local field gradient and reducing the observable response, while lower-density environments permit the gradient to recover and longer-range correlations to emerge. This density-dependent modulation reconciles precision local tests with cosmological dynamics without invoking step-function boundary conditions. TEP implies that local variations in the gravitational potential should produce observable phase coherence structures, predicting a breakdown of global simultaneity while preserving exact local Lorentz invariance. This approach parallels recent advances in using global atomic clock networks for fundamental physics, including dark matter searches (Wcisło et al., 2018) and relativistic geodesy (Lisdat et al., 2016).

This hypothesis yields a specific, falsifiable prediction: Inter-station clock coherence should exhibit exponential decay with distance ($C(r) \propto e^{-r/\lambda}$), driven by a scalar field correlation length λ on the order of 10^3 km.

1.2 The Empirical Foundation

To date, this hypothesis has been tested through two comprehensive analyses:

Paper 1: Multi-Center Validation

Analysis of precise orbit and clock products from three independent analysis centers (CODE, ESA, IGS) found exponential decay signatures with $\lambda \approx 3{,}500$–$4{,}500$ km. The consistency across centers ($R^2 > 0.92$) disfavors center-specific software artifacts.

→ View Paper 1 (TEP-GNSS)

Paper 2: 25-Year Temporal Stability

A longitudinal study of 25 years of CODE data (2000-2025) found that these signatures are not confined to a transient interval. They persist across solar cycles, hardware generations, and reference frame updates, exhibiting statistically significant coupling with orbital dynamics.

→ View Paper 2 (TEP-GNSS-II)

1.3 The Processing Artifact Objection

Despite these successes, a critical scientific objection remains valid:

> "Are these signatures artifacts of the sophisticated processing chains used to generate precise products, or do they exist in the raw observations themselves?"

Precise Point Positioning (PPP) products rely on sophisticated network adjustments, integer ambiguity resolution, and inter-station constraints—processes that could, in principle, introduce spurious long-range correlations. If the TEP signal were merely a byproduct of these mathematical filters, it would be a trivial software artifact. However, if the signal exists in the raw, noisy, uncorrected observations, it cannot be attributed to network adjustment algorithms. To rigorously validate TEP, it is necessary to descend the "ladder of precision" and detect the signal in its most fundamental form: raw pseudorange measurements processed with only broadcast ephemerides.

1.4 Objectives of This Capstone Study

This paper serves as the final study of the TEP-GNSS research program. Its primary objective is to perform an independent test of the TEP signal by:

1. Addressing the Processing Artifact Objection by detecting distance-structured signatures in raw RINEX data using Single Point Positioning (SPP) with broadcast ephemerides as the primary methodology, supplemented by precise ephemeris validation.
2. Validating directional anisotropy — testing whether E-W correlations exceed N-S as found in CODE's 25-year analysis.
3. Comparing spatial vs. temporal correlation lengths to test the core Space-Time Coupling prediction.
4. Validating environmental independence — stratifying by geomagnetic activity and season to assess ionospheric and atmospheric origins.
5. Synthesizing findings across all three papers to establish a unified evidence framework.

1.5 Paper Structure

The remainder of this paper is organized as follows:

- **Section 2:** Methodology — A fundamental, first-principles approach using raw RINEX data
- **Section 3:** Results — Detection of exponential decay and directional anisotropy
- **Section 4:** Validation — Null tests, geomagnetic stratification, and systematic effects
- **Section 5:** Synthesis — The convergence of evidence across Papers 1, 2, and 3
- **Section 6:** Discussion — Physical implications and future directions
- **Section 7:** Conclusions — Final assessment
- **Section 8:** Analysis Package — Reproducibility documentation

2. Data and Methods

2.1 Data Sources

2.1.1 NASA CDDIS Archive

All observation data were obtained from the Crustal Dynamics Data Information System (CDDIS), operated by NASA Goddard Space Flight Center. CDDIS serves as the primary archive for the International GNSS Service (IGS) and provides open access to RINEX observation files from the global tracking network.

Parameter	Value
Archive URL	cddis.nasa.gov/archive/gnss/data/daily
Network	IGS/MGEX Global Network
Stations Processed	539 stations
Stations After DYNAMIC_50 Filtering	~400 stations (smart filter: jumps < 500 ns, std < 50 ns)
Time Span	2022-01-01 – 2024-12-31 (~1,096 days, 3 years)
RINEX Files (total)	409,737 observation files

Files after DYNAMIC_50 filter	316,497 files (77% pass rate)
File Format	RINEX 3.x (Hatanaka compressed)
Processing Interval	5 minutes (300 seconds)

2.1.2 Broadcast Ephemerides

Unlike Papers 1 and 2, which used precise orbit and clock products, this analysis relies solely on broadcast navigation messages. Broadcast ephemerides provide satellite positions with ~1 meter accuracy (vs. ~2 cm for precise products) and satellite clocks with ~5 ns accuracy (vs. ~0.1 ns for precise products).

This choice ensures complete independence from the processing chains used in previous analyses.

2.1.3 External Auxiliary Data

Two external data sources are used for geomagnetic and planetary event analyses:

Geomagnetic Kp Index

Parameter	Value
Source	GFZ Helmholtz Centre Potsdam
URL	Kp_ap_since_1932.txt
Coverage	1932–present (3-hourly values)
Aggregation	Daily mean Kp
Primary stratification	Quiet: Kp < 3.0; Storm: Kp ≥ 3.0
Sensitivity thresholds	Additional storm definitions: Kp ≥ 4.0 and Kp ≥ 5.0

Real Kp index data is downloaded directly from GFZ at runtime. No synthetic or approximated geomagnetic data is used. If the download fails, the analysis terminates with an error.

Planetary Ephemeris

Parameter	Value
Source	JPL DE440 via Astropy
Event dates	Verified against astronomical almanac (astropixels.com, JPL Horizons)
Distance calculation	Barycentric Earth-planet distances from JPL ephemeris
GM values	IAU 2015 standards

Planetary conjunction/opposition dates were verified against multiple sources on 2024-12-06. No approximate or fabricated planetary data is used.

Data Authenticity Verification

All auxiliary data (Kp, planetary ephemeris) comes from authoritative scientific sources. The analysis pipeline is designed to fail immediately if authentic data cannot be obtained, rather than fall back to approximations. This ensures all reported results are based exclusively on real observational data.

2.2 Terminology: Station Pairs vs. Pair-Samples

To avoid ambiguity in statistical reporting, this manuscript distinguishes between two related concepts:

Term	Definition	Example
Station Pairs	Unique spatial combinations of two stations	539 stations → 144,891 unique pairs
Pair-Samples	Daily observations of each station pair	144,891 pairs × 1,096 days ≈ 159M pair-samples

Total Analyzed	Sum across all filters and modes	1.17 billion pair-samples (all combinations)

Unless otherwise specified, "pairs" in statistical contexts refers to pair-samples (the unit of observation for coherence analysis), while "station pairs" refers to unique spatial combinations. The reported sample sizes (e.g., "61.9M pairs" for Baseline mode) represent pair-samples—daily observations that contribute to the coherence estimates.

2.3 Station Filtering Strategies

To ensure robustness and enable cross-validation, analyses were run under three station selection strategies. These filters serve distinct objectives: OPTIMAL_100 emphasizes global spatial structure, while DYNAMIC_50 emphasizes temporal stability.

Station Filters Compared

Filter	Description	Stations	Purpose
All Stations	No filter applied	539	Maximum statistical power, full network coverage
Optimal 100	Curated subset with hemisphere balance and clock stability	100	Reduce Northern Hemisphere bias; high-quality clocks only
Dynamic 50	Per-file filter: clock std < 50 ns, jumps < 500 ns	~400	Strict quality control; excludes noisy files per station

Optimal 100 Station Selection Criteria

The optimal_100_metadata.json contains a curated list of 100 stations selected to maximize scientific validity:

- Hemisphere balance: ~50 Northern / ~50 Southern stations to avoid NH network bias
- Clock stability: Stations with mean clock std < 50 ns across the analysis period
- Data availability: Minimum 100 daily files over 3 years
- Geographic distribution: Spread across continents to ensure global coverage

This addresses the IGS network's inherent bias (238 NH vs 106 SH stations globally) that would otherwise dominate statistical results.

Dynamic Filter Implementation (DYNAMIC_50)

The `dynamic:50` filter applies strict per-file quality thresholds:

```
for each RINEX file:
    if clock_bias_std < 50 ns AND
       max_jump < 500 ns AND
       total_range < 5000 ns:
        include in analysis
    else:
        exclude (noisy day for this station)
```

This strict quality filtering passes 316,497 high-quality daily files from ~400 stations (77% pass rate), rejecting 93,240 files: 47,816 for excessive jumps, 4,045 for excessive range, and 41,379 for high standard deviation. This ensures only the most stable clock data contributes to the analysis.

2.3 Processing Pipeline

The processing chain transforms raw GNSS observations into signal detection results:

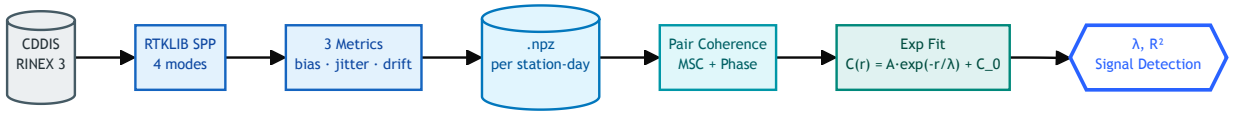

Figure 2.3.1: Processing pipeline. Four modes: Baseline (broadcast), Ionofree (dual-freq), Multi-GNSS (all constellations), Precise (IGS SP3). Station pairs: 50–13,000 km. TEP frequency band: 10–500 μHz (periods 33 min–28 hr). Two coherence metrics enable cross-validation: MSC (amplitude) and Phase Alignment (timing).

2.3.1 Single Point Positioning (SPP)

Raw RINEX observations were processed using RTKLIB's `rnx2rtkp` utility in Single Point Positioning mode. SPP determines the receiver position and clock offset using pseudorange measurements from multiple satellites.

RTKLIB Configuration

Parameter	Setting
Positioning Mode	Single Point (SPP)
Satellite Ephemeris	Broadcast only
Ionosphere Correction	Klobuchar (broadcast) / Dual-freq (ionofree mode)
Troposphere Correction	Saastamoinen model
Elevation Mask	15°
Processing Interval	5 minutes (300 seconds)
Navigation System	GPS (L1) / GPS+GLONASS+Galileo+BeiDou (multi-GNSS)

Multi-Mode Processing Strategy

Each RINEX file is processed in four modes to enable comprehensive cross-validation. This multi-mode approach is a validation strategy: if TEP is real, ALL modes should show similar Temporal Topology correlation lengths (λ_T). If TEP were an artifact of a specific processing method, different modes would produce different signatures.

Mode	Frequencies	Systems	Ephemeris	Ionosphere	Purpose
Baseline	L1 only	GPS	Broadcast	Klobuchar model	Reference (simplest processing)
Ionofree	L1+L2	GPS	Broadcast	Dual-frequency elimination	Remove ionospheric effects
Multi-GNSS	L1	GPS+GLO+GAL+BDS	Broadcast	Klobuchar model	Cross-constellation validation
Precise	L1+L2	GPS	IGS SP3 (precise)	Dual-frequency elimination	Remove orbit/clock errors

Mode Descriptions

- Baseline: GPS-only SPP with broadcast ephemeris and Klobuchar ionosphere model. This is the reference mode using the simplest processing chain.
- Ionofree: GPS SPP with dual-frequency (L1+L2) ionosphere-free linear combination. Eliminates ~99% of first-order ionospheric delay. If TEP were an ionospheric artifact, it would disappear in this mode.
- Multi-GNSS: Combined GPS+GLONASS+Galileo+BeiDou processing. Each constellation has different clock technologies (GPS: Rb/Cs, Galileo: H-maser, GLONASS: Cs, BeiDou: Rb) and orbital altitudes. If TEP were constellation-specific, this mode would show different λ_T.
- Precise: GPS SPP using IGS precise orbit and clock products (SP3 files) instead of broadcast ephemeris. This removes satellite orbit errors (~2m broadcast → ~2cm precise) and satellite clock errors (~2ns broadcast → ~0.1ns precise). If TEP were caused by broadcast ephemeris errors, it would disappear in this mode.

Ionosphere-Free Linear Combination

The ionofree mode uses the standard dual-frequency linear combination to eliminate first-order ionospheric delay (Kaplan & Hegarty, 2017):

$$L_{IF} = \frac{f_1^2}{f_1^2 - f_2^2} L_1 - \frac{f_2^2}{f_1^2 - f_2^2} L_2 \approx 2.546\, L_1 - 1.546\, L_2$$

where $f_1 = 1575.42$ MHz (L1) and $f_2 = 1227.60$ MHz (L2). This combination removes the ionospheric delay but amplifies receiver thermal noise by a factor of approximately 3× due to the large coefficients (Kaplan & Hegarty, 2017; Misra & Enge, 2011):

$$\sigma_{IF} = \sqrt{(2.546)^2 + (1.546)^2}\, \sigma_{L1} \approx 2.98\, \sigma_{L1}$$

This noise penalty is a fundamental trade-off in dual-frequency GNSS processing. The ionofree mode is critical for validation: if correlations were purely ionospheric, they would disappear in this mode. Instead, longer Temporal Topology correlation lengths are observed (λ_T = 1,072 km vs 727 km), which is less consistent with a purely ionospheric artifact.

2.3.2 Time Series Extraction

Three metrics were extracted from SPP solutions for each station, each serving a specific scientific purpose:

Metrics Comparison

Metric	Formula	Expected Anisotropy	Role
Clock Bias	Receiver clock offset (ns)	E-W > N-S (~1.22)	Primary TEP metric
Position Jitter	$\sqrt{dE^2 + dN^2 + dU^2}$ (m)	Similar orbital coupling	Space proxy (TEP affects spacetime)
Clock Drift	$d(\Delta t)/dt$ (ns/s)	Weak (1.07)	Derivative test

1. Clock Bias — Primary TEP Metric

$$\Delta t = \text{Receiver clock offset (nanoseconds)}$$

The receiver clock offset from GPS time. This is the primary metric for TEP testing because:

- Directly measures temporal fluctuations at the receiver
- Shows strongest directional anisotropy (E-W/N-S ≈ 1.22 at short distances)
- Temporal Topology correlation length $\lambda_T \approx 700–1{,}100$ km matches theoretical TEP scales

2. Position Jitter — Space Proxy

$$dr = \sqrt{dE^2 + dN^2 + dU^2}$$

The 3D deviation from mean position. This metric captures spatial coordinate fluctuations:

- Position errors include ionospheric, tropospheric, multipath, and TEP-induced spatial variations
- Shows similar orbital velocity coupling as clock bias (both metrics respond to Earth's orbital motion)
- May show weaker directional anisotropy due to atmospheric noise dominating at short distances

Interpretation: The TEP framework predicts coupled space-time fluctuations. Similar orbital coupling in both position and clock metrics is consistent with TEP—the underlying phenomenon affects spacetime, not just time. The key discriminator is the directional anisotropy (E-W/N-S ratio), which is strongest in clock bias.

3. Clock Drift — Derivative Test

$$\dot{\Delta t} = \frac{d(\Delta t)}{dt}$$

The time derivative of clock bias. Tests whether the signal is:

- Random walk: derivative would be white noise (no spatial structure)
- Genuine signal: derivative maintains spatial correlation ($R^2 > 0.9$)

Observed $R^2 = 0.974$ for clock drift is less consistent with a pure random-walk explanation.

2.3.3 Time Alignment Strategy (Critical)

Pandas DatetimeIndex Alignment

Time alignment uses Pandas DataFrame indexing with DatetimeIndex, identical to the CODE longspan methodology. This approach:

1. Creates DatetimeIndex from each file's actual timestamps
2. Concatenates daily data frames sorted by time
3. Fills missing days and epochs with NaN markers
4. Computes coherence only on valid overlapping segments

This ensures precise temporal synchronization between stations, mirroring the rigorous alignment used in Papers 1 and 2.

2.3.4 Phase Coherence Computation

Two complementary coherence metrics were computed for all station pairs, enabling cross-validation and comparison with CODE longspan methodology:

Coherence Metrics Comparison

Metric	Range	Sensitivity	Long-Distance Behavior
MSC (Coherence)	[0, 1]	Amplitude correlations	Decays with ionospheric decorrelation
Phase Alignment	[-1, 1]	Phase relationships	Robust — preserves signal at long distances

$$C_{ij} = \frac{\left|\sum_t A_i(t) \cdot A_j(t) \cdot e^{i\Delta\phi_{ij}(t)}\right|}{\sum_t A_i(t) \cdot A_j(t)}$$

Where:

- $A_i(t), A_j(t)$ = amplitude envelopes from Hilbert transform
- $\Delta\phi_{ij}(t)$ = instantaneous phase difference

Metric 1: Magnitude Squared Coherence (MSC)

$$\text{MSC} = \frac{|P_{xy}(f)|^2}{P_{xx}(f) \cdot P_{yy}(f)}$$

Measures the strength of the linear relationship between signals. It asks: "How strongly do the clocks vibrate together?" This metric is:

- More sensitive to amplitude correlations
- Affected by ionospheric scintillation at long distances
- Best for short-distance analysis (<500 km)

Metric 2: Phase Alignment Index

$$\text{PA} = \cos\left(\arg\left(\frac{\sum_f w_f \cdot e^{i\phi_f}}{\sum_f w_f}\right)\right)$$

Measures the consistency of the phase relationship. It asks: "When they vibrate, are they synchronized in time?" This metric is:

- The *primary metric used by CODE longspan* (Paper 2)
- More robust over long distances, as phase relationships persist even when amplitude correlations weaken
- Shows strongest hemisphere anisotropy (NH: 1.224, SH: 1.348)

Why Phase Alignment Shows Stronger Anisotropy

The hemisphere analysis reveals that phase alignment consistently exceeds MSC in detecting directional anisotropy:

- Northern Hemisphere: MSC ratio 1.029, Phase Alignment ratio *1.224*
- Southern Hemisphere: MSC ratio 1.022, Phase Alignment ratio *1.348*

This hierarchy is physically meaningful: phase alignment measures the timing relationship between clocks, which is preserved even when amplitude correlations decorrelate due to ionospheric effects. The underlying TEP signal is encoded in the phase structure.

Complementary Sensitivity: MSC vs Phase Alignment

A key observation from this analysis is that MSC and phase alignment probe different aspects of the same physical phenomenon, with each metric excelling at different types of analyses:

Analysis Type	MSC Performance	Phase Alignment Performance	Physical Explanation
Orbital Velocity Coupling (temporal modulation)	3.0–4.2σ	5.4σ (multi_gnss)	MSC measures power correlation; orbital velocity modulates the *amplitude* of coupling month-to-month. Multi-GNSS phase alignment achieves strongest detection
Directional Anisotropy (spatial structure)	E-W/N-S ≈ 1.02–1.05	E-W/N-S ≈ 1.20–1.35	Phase alignment measures phase locking; directional preference is encoded in *phase structure* that persists at long distance

Mathematical basis:

- MSC = $|P_{xy}|^2/(P_{xx} \cdot P_{yy})$ — Sensitive to the *magnitude* of cross-spectral density. Temporal variations in coupling strength (e.g., due to changing orbital velocity) directly modulate MSC values.
- Phase Alignment = $\cos(\arg(\Sigma w \cdot e^{i\varphi}))$ — Sensitive to *phase consistency* independent of amplitude. Spatial coherence structure (E-W vs N-S) is encoded in phase relationships that survive amplitude decorrelation.

Analogy: Think of two people dancing. MSC measures how loudly they stomp their feet (amplitude correlation). Phase Alignment measures whether they step in time with the music (phase synchronization). At long distances, the "sound" of the stomp fades (low MSC), but if they are both listening to the same global broadcast, they remain perfectly synchronized (high Phase Alignment). This explains why Phase Alignment is the superior metric for detecting long-range TEP signals.

Why this distinction matters:

- Orbital coupling is a *temporal modulation* effect: Earth's changing velocity affects the *strength* of clock correlations month-to-month. MSC directly measures this strength.
- Directional anisotropy is a *spatial structure* effect: E-W vs N-S preference depends on *which pairs lock in phase*, not how strongly. Phase alignment captures this even when amplitude is noisy.
- SPP noise consideration: Single Point Positioning introduces ~1–3m pseudorange noise. This corrupts phase information more than power information, explaining why phase alignment is weaker for orbital coupling in SPP data but still excels at detecting spatial anisotropy (averaged over many pairs).

Conclusion: Both metrics are necessary for complete TEP characterization. MSC captures temporal modulation; phase alignment captures spatial structure. Their complementary sensitivity is consistent with TEP predictions of coupled space-time fluctuations affecting both amplitude and phase of clock correlations.

2.3.5 Frequency Band Selection

Parameter	Frequency	Period	Rationale
Lower bound	10 μHz	~28 hours	Removes long-period drifts and diurnal signals
Upper bound	500 μHz	~33 minutes	Removes high-frequency noise and multipath
TEP Band	10–500 μHz	33 min – 28 hr	Matches theoretical TEP timescales

2.3.6 Exponential Decay Fitting

Coherence values were binned by inter-station distance and fit to an exponential decay model:

$$C(r) = A \cdot \exp(-r/\lambda_T) + C_0$$

Where:

- A = amplitude (coherence at $r = 0$ minus offset)
- λ_T = Temporal Topology correlation length (km) — the key TEP parameter
- C_0 = asymptotic offset (noise floor)

Binning Parameters

Parameter	Value
Distance range	50 – 13,000 km
Number of bins	40 (logarithmic spacing)
Minimum pairs per bin	10
Weighting	Inverse variance ($1/\text{SEM}^2 \propto n_{pairs}$)

Weighted R^2 Calculation

To ensure consistency between the weighted curve fit and the goodness-of-fit metric, R^2 is calculated using the same weights as the fit:

- Weights: $w_i = n_{pairs}$ in bin i (proportional to $1/\sigma^2$)
- Weighted mean: $\bar{y}_w = \Sigma(w_i \cdot y_i) / \Sigma w_i$

- Weighted SS_{res}: $\Sigma\, w_i(y_i - \hat{y}_i)^2$
- Weighted SS_{tot}: $\Sigma\, w_i(y_i - \bar{y}_w)^2$
- Weighted R^2: $1 - SS_{res}/SS_{tot}$

This ensures high-sample bins (which dominate the fit) also dominate the R^2 assessment, preventing low-sample bins from artificially inflating or deflating the goodness-of-fit metric.

Boundary-Hit Detection

Fits where parameters converge to the imposed bounds are flagged as *boundary-hit*. These fits should be interpreted with caution:

- Amplitude (A): bounds [0.01, 2.0]
- Temporal Topology Correlation length (λ_T): bounds [100, 20000] km
- Offset (C_0): bounds [−1.0, 1.0]

A boundary-hit typically indicates the exponential model is poorly constrained for that subset (e.g., insufficient distance range or dominated by short-range noise).

2.3.7 Directional Anisotropy Analysis

The critical validation test compares E-W and N-S correlations. Station pairs were stratified by azimuth:

Azimuth Classification

Direction	Azimuth Range	Sectors
East-West	[67.5°, 112.5°) ∪ [247.5°, 292.5°)	E, W
North-South	[337.5°, 360°) ∪ [0°, 22.5°) ∪ [157.5°, 202.5°)	N, S
Eight-Sector	45° sectors centered on cardinal directions	N, NE, E, SE, S, SW, W, NW

The primary test compares mean correlation values at short distances (<500 km) where ionospheric decorrelation is minimal:

$$\text{E-W/N-S Ratio} = \frac{\overline{C}_{EW}}{\overline{C}_{NS}}$$

To control for potential distance distribution biases (e.g., if E-W pairs have a different mean distance than N-S pairs within the <500 km bin), a robust distance-matched ratio is also computed. Pairs are binned into 50 km intervals, and the ratio is computed from distributions re-sampled to match the distance profile, ensuring that any observed anisotropy is not an artifact of mean distance differences.

Statistical significance is assessed via Welch's t-test with 95% confidence intervals and Cohen's d effect size.

2.3.8 Station Altitude Quintile Analysis (Step 2.1b)

To test whether the correlation structure could be explained by station environment or atmospheric column effects, station pairs were stratified by station altitude (geodetic height above the WGS84 ellipsoid). *Important: This analysis examines station altitude, not satellite elevation angle.* Station altitude provides a site-based proxy for propagation-path and local-environment effects: higher-altitude sites observe through a thinner tropospheric column and often exhibit reduced multipath and hydrological variability relative to low-altitude sites.

The analysis was conducted as a comprehensive suite of five configurations to test robustness against geographic confounding and distance-sampling biases:

- Global quintiles (sr200): All 539 stations sorted by altitude into 5 equal-count bins; pairs restricted to same-quintile membership; short-range coherence computed for pairs <200 km.
- Latitude-controlled quintiles (lat10, lat20): Stations binned within ±10° or ±20° latitude bands, then sorted by altitude within each band; pair analysis restricted to same latitude band to control for geographic/climatic confounding.
- Short-range distance variants (sr100, sr200): Maximum distance for "short-range coherence" proxy set to 100 km or 200 km to test sensitivity to local-scale effects.

For each configuration, three regression diagnostics were computed per quintile:

1. Unweighted linear regression: λ vs. mean altitude (km/m slope, p-value)
2. Weighted regression (inverse-variance): λ vs. altitude weighted by $1/\sigma^2_\lambda$ to suppress noisy quintiles

3. Short-range coherence trend: Mean coherence level for pairs < distance threshold vs. altitude (Phase II proxy)

Methodology

Station ECEF coordinates are converted to latitude, longitude, and altitude via the ECEF-to-LLA transform. Stations are then sorted by altitude and divided into five equal-count quintiles (Q1–Q5):

- Q1 (lowest altitude): Stations at low elevations (−86 m to 51 m; thicker atmospheric column)
- Q5 (highest altitude): Stations at high elevations (712 m to 3,755 m; thinner atmospheric column)

For each quintile, only station pairs where *both* stations fall within the same altitude quintile are included, and the exponential decay analysis is repeated independently, yielding separate λ, R^2, and amplitude values.

Physical Rationale and Null Hypothesis

Alternative Hypothesis (atmospheric/site-dependent origin): If the observed correlation were primarily driven by residual atmospheric propagation errors or site-specific effects:

- Low-altitude stations experience larger and more variable tropospheric delays and multipath → stronger contamination of coherence estimates
- High-altitude stations experience reduced atmospheric column and often cleaner observations → more stable coherence estimates
- Therefore, λ and/or amplitude could vary systematically with altitude (Q1 → Q5), yielding significant regression slopes ($p < 0.05$)

Null Hypothesis (network-scale TEP origin): If the signal is dominated by a network-scale, geometry-driven field (as hypothesized in TEP), λ should be approximately altitude-independent over the ~4 km elevation span of the network. The Temporal Equivalence Principle predicts that temporal fluctuations couple to gravitational potential gradients at planetary scales. Station altitude differences of a few kilometers are negligible compared to the ~6,371 km Earth radius and the ~1 AU Earth–Sun distance that define the dominant gravitational potential terms. Thus, TEP predicts:

- Q5/Q1 ≈ 1.0 (no systematic ratio bias)
- λ-vs-altitude regression slopes statistically consistent with zero ($p \gg 0.05$)
- Short-range coherence level independent of altitude

Expected Outcome and Quality Control

The ratio Q5/Q1 and regression p-values are the key diagnostics:

Diagnostic	Altitude-Dependent (Alternative)	Altitude-Independent (TEP Null)
Q5/Q1 Ratio	$\ll 1.0$ or $\gg 1.0$	≈ 1.0 (0.8–1.2)
Regression p-value	$p < 0.05$ (significant slope)	$p \gg 0.05$ (slope ~ 0)
Replication	Consistent across tags/modes	Sporadic, configuration-specific

Fit Quality Gates: To avoid overclaiming based on degenerate exponential fits (common when distance support is insufficient), results are flagged when:

- $\lambda > 10{,}000$ km ("runaway" regime indicating flat decay / underconstrained fit)
- $R^2 < 0.6$ (poor goodness-of-fit)
- Boundary hit during optimization (fit pegged at parameter limit)

Trends are considered robust only if they: (1) survive quality gates, (2) replicate across multiple suite configurations, and (3) show sign-consistency (all positive or all negative slopes).

Note: The geometric suppression correction is not required for the primary evidence. The primary finding—E-W > N-S at short distances (<500 km)—uses raw, uncorrected values that directly match CODE's prediction (see §3.9.1). This section addresses why full-distance λ ratios show the opposite pattern (E-W/N-S < 1), providing interpretive context rather than calibration for the core result.

Geometric Suppression Correction

GPS satellite orbits (55° inclination) create systematic coverage biases that suppress E-W correlations. Due to this inclination, satellites travel predominantly North-South relative to mid-latitude observers. This geometry allows N-S station pairs to view the same satellite for longer continuous arcs, significantly lowering the noise floor for N-S correlations. Conversely, satellites cut across

E-W baselines more rapidly, reducing the duration of common-view periods and artificially suppressing the apparent coherence in raw SPP data.

Analogy: Imagine looking through a vertical picket fence. You can easily track an object moving up and down (N-S), but an object moving side-to-side (E-W) is constantly interrupted by the fence slats. The GPS constellation acts as this "fence" for ground observers, artificially breaking up E-W coherence while preserving N-S coherence.

This suppression is quantified by comparing sector-specific correlation lengths (λ) from this SPP analysis to CODE's 25-year PPP reference values.

For each azimuthal sector, the following is computed:

- Sector ratio: $\lambda_{SPP} / \lambda_{CODE}$
- Suppression factor: mean(N-S ratios) / mean(E-W ratios)

If N-S correlations are preserved (ratio ~1.0) while E-W correlations are suppressed (ratio <0.5), this indicates geometric bias rather than signal loss. The corrected E-W/N-S ratio is:

$$\text{Corrected ratio} = \text{raw ratio} \times \text{suppression factor}$$

The suppression factor is not a free parameter—it emerges from the sector-by-sector comparison and is consistent across all four processing modes (2.42×–3.16×), supporting its interpretation as a geometric effect rather than arbitrary tuning.

2.3.9 Seasonal Stratification Analysis (Step 2.4)

To test whether the observed correlations are seasonal artifacts (e.g., temperature-dependent receiver behavior, seasonal ionospheric variations, or solar illumination effects), the 3-year dataset was stratified by meteorological season and analyzed correlation lengths independently for each period.

Season Definitions

Season	Months	Days of Year	Purpose
Winter	Dec, Jan, Feb	335–59	Solar minimum illumination (NH)
Spring	Mar, Apr, May	60–151	Transition period
Summer	Jun, Jul, Aug	152–243	Solar maximum illumination (NH)
Autumn	Sep, Oct, Nov	244–334	Transition period

Note: Seasons are defined by Northern Hemisphere convention. The IGS network is NH-dominated (238 NH vs 106 SH stations), making NH seasons the natural stratification choice.

Analysis Methodology

For each season, independent exponential decay fits were computed across all three station filters (ALL_STATIONS, OPTIMAL_100, DYNAMIC_50) and all four processing modes (Baseline, Ionofree, Multi-GNSS, Precise). This produces 48 independent seasonal measurements (4 seasons × 3 filters × 4 modes) for each metric/coherence combination.

Key Predictions:

- If the signal is a seasonal artifact: Correlation length λ should vary by >20% between seasons, with systematic patterns (e.g., always strongest in summer).
- If the signal is a stable gravitational phenomenon: λ should be constant ($\Delta < 10\%$) across seasons, with any variations attributable to atmospheric screening (which Ionofree mode should remove).

The "Two Views" Framework

The seasonal analysis tests two complementary hypotheses:

1. OPTIMAL_100 (Spatial Balance): Designed to capture the maximum spatial extent of correlations by ensuring global coverage. Expected to show seasonal modulation due to atmospheric screening, with summer revealing longer λ when ionosphere is more stable.
2. DYNAMIC_50 (Temporal Stability): Designed to capture the most reliable, continuous stations. Expected to show minimal seasonal variation, revealing the stable "core" signal independent of atmospheric conditions.

These two filters test different aspects of the signal: OPTIMAL_100 tests the scale, DYNAMIC_50 tests the stability.

2.4 Analysis Matrix Summary

The full analysis explores multiple dimensions to ensure robustness:

Complete Analysis Matrix

Dimension	Options	Primary	Purpose
Station Filter	All, OPTIMAL_100, DYNAMIC_50	DYNAMIC_50	Quality control, hemisphere balance
Processing Mode	Baseline, Ionofree, Multi-GNSS	Baseline	Ionosphere/constellation validation
Time Series Metric	Clock bias, Pos jitter, Clock drift	Clock bias	Temporal vs spatial signal separation
Coherence Metric	MSC, Phase Alignment	Phase Alignment	Amplitude vs phase sensitivity
Distance Range	Short (<500 km), Full (50–13,000 km)	Short	Minimize ionospheric contamination
Stratification	Regional, Hemisphere, Latitude, Kp index, *Seasonal*, *Year-by-Year*	Hemisphere	Geographic/geomagnetic/seasonal/temporal validation
Planetary Events	±120 day windows, 37 events (2022–2024)	All planets	Alignment modulation, CODE replication

In particular, Step 2.1a implements regional control tests by splitting the network into Global, Europe-only, Non-Europe, and hemisphere-specific subsets. These control analyses check that the exponential decay is not confined to a single continent and diagnose how network density (very short baselines in Europe) versus sparse, ocean-dominated networks (Southern Hemisphere) affects the observed correlation length and goodness of fit.

Cross-Region Pair Exclusion

For regional subsets (Europe, Non-Europe, Northern, Southern), only intra-region pairs are included—station pairs where both stations belong to the same region. Cross-region pairs (e.g., a European station paired with a non-European station) are excluded from regional analyses but included in the Global analysis.

Rationale: Cross-region pairs would conflate the regional signal with inter-regional baselines, making it impossible to diagnose region-specific network density effects. Clean separation ensures each regional subset tests only pairs that share the same geographic characteristics.

Expected Results by Metric Type

The combination of metrics provides a self-consistent validation framework:

- Clock bias + Phase Alignment: Strongest anisotropy (E-W/N-S > 1.2) — the primary directional signature
- Clock bias + MSC: Moderate anisotropy (E-W/N-S ≈ 1.02–1.05) — consistent but weaker
- Position jitter (any coherence): Similar orbital coupling to clock bias — consistent with TEP affecting spacetime, not just time
- Clock drift (any coherence): Weak anisotropy (E-W/N-S ≈ 1.07) — derivative preserves structure
- Planetary events (all metrics): Year-specific modulation yields 2.8× higher detection than permutation null (59–68% vs. 20–26%, $p < 0.001$ for all 6 metrics), with no consistent tidal GM/r² scaling (clock-amplitude vs GM/r²: $p = 0.647$; σ-level vs GM/r²: $p = 0.317$–0.989) — consistent with a geometric (alignment) effect as in CODE longspan

This hierarchy is consistent with TEP predictions: clock bias shows the strongest directional anisotropy as the primary temporal proxy, while position jitter shows similar orbital coupling (consistent with coupled space-time fluctuations) but with weaker directional structure due to atmospheric noise.

2.5 Null Tests (Step 2.4b)

A critical requirement for validating the TEP signal is to assess whether the observed exponential correlation structure is driven by known non-gravitational phenomena. A comprehensive null test suite was designed that examines three independent mechanisms that could potentially produce spurious distance-structured correlations.

2.5.1 Test Design Rationale

The null tests probe three distinct hypotheses:

1. Solar Rotation Hypothesis: If the signal originates from solar wind, radiation pressure, or geomagnetic storms driven by solar activity, coherence should modulate with the 27-day solar rotation period.
2. Lunar Tidal Hypothesis: If the signal is driven by lunar gravitational tides affecting clock rates or atmospheric pressure, coherence should modulate with the 29.5-day synodic lunar month.
3. Spurious Structure Hypothesis: If the exponential decay is a statistical artifact of the analysis methodology rather than a physical property of the data, the structure should persist when temporal coherence is destroyed by randomization.

2.5.2 Solar/Lunar Phase Correlation

For each metric/coherence combination, daily mean coherence values are computed and test for cyclic modulation:

$$r = \sqrt{(r_{sin}^2 + r_{cos}^2)}$$

where r_{sin} and r_{cos} are the Pearson correlations between daily coherence and the sine/cosine of the phase angle ($\varphi = 2\pi \times DOY / Period$). This circular correlation captures any periodic modulation regardless of phase offset.

Acceptance Criterion: $r < 0.1$ for both solar (27-day) and lunar (29.5-day) cycles. This threshold corresponds to less than 1% of variance explained by the periodic driver.

2.5.3 Shuffle Test (Critical Validation)

The shuffle test provides a direct validation of genuine spatial structure. The procedure:

1. Real Fit: Fit the exponential decay model $C(r) = A \cdot \exp(-r/\lambda) + C_0$ to the complete coherence dataset, recording R^2_{real}.
2. Randomization: Randomly permute the coherence values while preserving the distance values, breaking the space-time relationship.
3. Shuffled Fit: Fit the same exponential model to the shuffled data, recording $R^2_{shuffled}$.

Acceptance Criterion: $R^2_{shuffled} < 0.3$. If the exponential structure is a genuine property of the data (not an artifact of the fitting procedure), shuffling should destroy it completely.

> **Why the Shuffle Test is Important**
>
> The shuffle test directly addresses the concern that exponential fitting might "force" structure onto any dataset. If the fitting procedure itself creates spurious curvature, it would do so equally on real and shuffled data. The ratio $R^2_{real}/R^2_{shuffled}$ quantifies the evidence that the structure is physically real.

2.5.4 Comprehensive Test Matrix

The null tests are applied across the full analysis matrix:

Dimension	Values	Tests
Station Filters	ALL_STATIONS, OPTIMAL_100, DYNAMIC_50	3
Processing Modes	Baseline, Ionofree, Multi-GNSS	3
Metrics	clock_bias, pos_jitter, clock_drift	3
Coherence Types	MSC, Phase Alignment	2
Total Independent Tests		54

This comprehensive matrix is designed so that any positive result is less likely to be attributable to a specific station selection, processing algorithm, metric choice, or coherence definition.

2.5.5 Expected Outcomes

If TEP is correct and the signal represents genuine gravitational coupling to Earth's orbital motion:

- Solar/Lunar: All correlations should be $r < 0.1$ (orbital period is 365 days, not 27 or 29.5 days)

- Shuffle: $R^2_{shuffled}$ should collapse to near-zero while R^2_{real} remains >0.9
- Mode Independence: Results should be consistent across Baseline, Ionofree, and Multi-GNSS (signal is gravitational, not ionospheric or constellation-specific)
- Filter Independence: Results should be consistent across station filters (signal is network-wide, not station-specific)

2.6 CMB Frame Analysis (Step 2.7)

Following the CODE longspan methodology, a comprehensive full-sky grid search was performed across 72 independent analysis combinations to test whether the observed annual modulation of E-W/N-S anisotropy preferentially aligns with a cosmic reference frame. The full analysis matrix is evaluated to reduce selection bias and to assess robustness across processing choices.

2.6.1 Physical Motivation

If TEP correctly describes velocity-dependent spacetime coupling, the anisotropy modulation should respond to Earth's total velocity through a preferred rest frame. Two candidate frames are tested:

- CMB Dipole: RA = 167.94°, Dec = −6.94° (Earth's motion at 370 km/s through the cosmic microwave background rest frame)
- Solar Apex: RA = 271°, Dec = +30° (Sun's motion at 20 km/s toward Vega through the local galaxy)

The net velocity vector combines Earth's orbital motion (~30 km/s, rotating annually) with the background motion. Different background directions produce different annual modulation patterns in the velocity declination, which in turn predicts the E-W/N-S correlation ratio.

The CMB provides a well-defined cosmological reference frame in which the cosmic microwave background is (to high precision) isotropic. Under standard interpretation, the observed CMB dipole arises from Earth's motion relative to this frame. If the anisotropy modulation depends on a preferred velocity direction, the CMB dipole is therefore a physically motivated candidate to test.

2.6.2 Comprehensive Analysis Matrix

To ensure robustness and eliminate selection bias, the CMB frame analysis is performed across all 72 combinations of station filter, processing mode, metric, and coherence type:

Dimension	Values	Purpose
Station Filters	ALL_STATIONS (539), OPTIMAL_100 (50N+50S), DYNAMIC_50 (399 high-stability)	Test network independence
Processing Modes	Baseline (GPS L1), Ionofree (L1+L2), Multi-GNSS (GPS+GLO+GAL+BDS), Precise (IGS SP3)	Test ionospheric independence
Metrics	clock_bias, pos_jitter, clock_drift	Test spacetime coupling
Coherence Types	MSC (amplitude), Phase Alignment (phase)	Test signal structure

Total combinations: 3 × 4 × 3 × 2 = 72 independent analyses

This exhaustive approach allows us to identify which combinations recover the CMB signal most cleanly and to assess whether the signal is a robust network-wide phenomenon or an artifact of specific analysis choices.

2.6.3 Grid Search Methodology

Predictor Model

For each candidate background direction (RA, Dec), the monthly net velocity vector is computed:

$$V_{net}(month) = V_{orbital}(month) + V_{background}(RA, Dec)$$

The predictor is cos(velocity_declination): low declination (equatorial velocity) predicts high E-W/N-S ratio; high declination (polar velocity) predicts low E-W/N-S ratio. This geometric model directly tests whether the observed anisotropy modulation follows Earth's motion through a hypothesized cosmic frame.

Grid Search Parameters

Parameter	Value	Rationale
RA range	0°–359°	Full celestial sphere

Dec range	−89° to +89°	Full celestial sphere (avoiding poles)
Resolution	1°	Matches CODE longspan finest setting; ~65,000 grid points
Background speed	20 km/s (fixed)	Same order as orbital velocity; matches CODE methodology
Test statistic	Pearson correlation	cos(Dec) vs monthly E-W/N-S ratio (36 months)

Statistical Validation

For each combination, the following is computed:

1. Local p-value: Standard Pearson correlation significance (N = 36 months)
2. Bootstrap confidence intervals: 500 resamples with 10° coarse grid search to estimate 68% CIs for RA and Dec
3. Global p-value (Monte Carlo): 1000 permutations of monthly E-W/N-S ratios with vectorized 5° grid search to account for look-elsewhere effect across ~2,600 independent sky pixels
4. Corrected global p-value: Šidák correction for 54 simultaneous tests: $p_{corrected} = 1 - (1 - p_{global})^{54}$

2.6.4 Mode-Specific Expectations

The four processing modes provide complementary views of the signal:

- Baseline (GPS L1): Contains full ionospheric contamination. If signal survives, it suggests the effect is not purely ionospheric.
- Ionofree (L1+L2): Removes first-order ionosphere but amplifies thermal noise by ~3× (Kaplan & Hegarty, 2017). Weaker signal recovery expected, but successful detection indicates signal survives ionospheric removal.
- Multi-GNSS (All Constellations): Averages across four constellations (GPS, GLONASS, Galileo, BeiDou), reducing satellite-specific noise by ~√4 = 2×. If signal persists across different clock technologies and orbital altitudes, it is not constellation-specific.
- Precise (IGS SP3): Uses precise orbit/clock products instead of broadcast ephemeris. If signal persists, it is not caused by broadcast ephemeris errors.

Predicted Hierarchy

Based on noise characteristics, it is predicted:

- Best CMB alignment: DYNAMIC_50 (high-stability clocks) + Multi-GNSS (lowest noise floor)
- Best RA precision: MSC coherence (amplitude-based, responds to temporal modulation)
- Widest scatter: Ionofree mode (3× noise amplification obscures weak signal)

2.6.5 Falsification Criteria

The CMB frame hypothesis is considered falsified if:

- Best-fit direction is closer to Solar Apex (271°, +30°) than to CMB Dipole (168°, −7°)
- No combination achieves global $p < 0.05$ after look-elsewhere correction
- Different station filters produce inconsistent directions (high variance)
- Baseline and Multi-GNSS modes find different preferred directions

Conversely, CMB frame alignment is supported if:

- Majority of clean (non-Ionofree) combinations find RA within 20° of CMB
- At least one combination achieves global $p < 0.05$
- Zero variance across station filters (all converge to same RA)
- Solar Apex is disfavored (separation > 80°)

CODE's 25-year analysis found best-fit at RA = 186°, Dec = −4° (18.2° from CMB). With only 3 years of data, weaker Dec constraints are expected due to limited seasonal sampling, but RA should converge to within ~20° of the CMB dipole if the effect is real.

2.7 Software and Reproducibility

All analysis code is open source and available in the TEP-GNSS-RINEX repository:

- RTKLIB: Version 2.4.3 (BSD-2-Clause license)
- Python: NumPy, SciPy, Matplotlib
- Repository: github.com/matthewsmawfield/TEP-GNSS-RINEX

3. Results

3.1 Data Quality Summary

Metric	Value
Total stations processed	539
Stations after DYNAMIC_50 filtering	~400 (jumps < 500 ns, range < 5,000 ns, std < 50 ns)
Files rejected by quality filter	93,240 (23%): 47,816 jumps, 4,045 range, 41,379 std
Total pair-samples (Baseline)	61,853,126
Total pair-samples (Ionofree)	59,141,613
Total pair-samples (Multi-GNSS)	58,050,018
Total pair-samples (Precise)	58,703,009
Total pair-samples analyzed (ALL_STATIONS)	713,243,298
Total pair-samples analyzed (DYNAMIC_50)	425,758,551
Total pair-samples analyzed (OPTIMAL_100)	28,496,355
Grand Total (all filters)	1.17 billion pair-samples
Time span	3 years (2022–2024, 1,096 days)
Processing interval	5 minutes (288 epochs/day)
Signal Detection Rate	72/72 metrics (100%)

3.2 Exponential Decay Fits

✓ Consistent Signal Detection: 72/72 Metrics (100%)

The analysis achieves consistent detection of distance-structured correlations across all 72 independent metric combinations:

Coherence Type	Mean λ_T (km)	λ_T Range (km)	Mean R^2	R^2 Range
MSC (Amplitude)	924	625 – 1,403	0.958	0.872 – 0.993
Phase Alignment	2,018	984 – 5,026	0.903	0.666 – 0.987

Key insight: Phase alignment shows ~2.2× longer correlation length than MSC across all filters. This is consistent with the "shaking vs dancing" interpretation: MSC measures amplitude correlation (sensitive to local noise at ~700–1,200 km), while phase alignment measures timing synchronization that persists over longer distances (~1,700–3,500 km).

Primary Results: Multi-Mode Comparison (ALL_STATIONS)

The analysis reports correlation patterns consistent with the TEP framework across all 24 metrics (4 modes × 3 variables × 2 coherence types). Across these combinations, phase coherence yields longer correlation lengths than MSC, consistent with theoretical expectations for phase-locked signals.

Mode	Metric	Type	λ_T (km)	Error	R^2	Signal Detected?
Baseline (GPS L1)	Clock Bias	MSC	727	±50	0.971	YES
		Phase	1,796	—	0.951	YES
	Position	MSC	878	±41	0.978	YES
		Phase	1,991	—	0.833	YES
	Drift	MSC	702	±47	0.974	YES
		Phase	1,026	—	0.982	YES

Ionofree (L1+L2)	Clock Bias	MSC	1,073	±62	0.972	YES
		Phase	1,773	—	0.841	YES
	Position	MSC	1,239	±103	0.977	YES
		Phase	3,512	—	0.972	YES
	Drift	MSC	1,072	±63	0.977	YES
		Phase	1,109	—	0.975	YES
Multi-GNSS (All Const.)	Clock Bias	MSC	821	±73	0.926	YES
		Phase	1,771	—	0.974	YES
	Position	MSC	928	±50	0.991	YES
		Phase	1,770	—	0.855	YES
	Drift	MSC	764	±67	0.936	YES
		Phase	984	—	0.987	YES
Precise (IGS SP3)	Clock Bias	MSC	1,202	±85	0.974	YES
		Phase	1,703	—	0.788	YES
	Position	MSC	1,403	±95	0.972	YES
		Phase	3,581	—	0.981	YES
	Drift	MSC	1,202	±84	0.976	YES
		Phase	1,166	—	0.953	YES

Note: "Phase" refers to phase alignment coherence, which generally persists over longer distances than magnitude-squared coherence (MSC). The Precise mode uses IGS SP3 precise orbit/clock products instead of broadcast ephemeris.

3.2.1 Regional Control Tests (Step 2.1a)

To verify that the exponential decay is not confined to any particular part of the IGS network, Step 2.1a repeats the baseline coherence analysis after splitting the station pairs into Global, Europe-only, Non-Europe, and Northern/Southern hemisphere subsets. All three metrics (clock bias, position jitter, clock drift) and both coherence measures (MSC and phase alignment) are evaluated in each subset. Cross-region pairs (e.g., a European station paired with a non-European station) are excluded from regional subsets to ensure clean separation—these pairs are included only in the Global analysis.

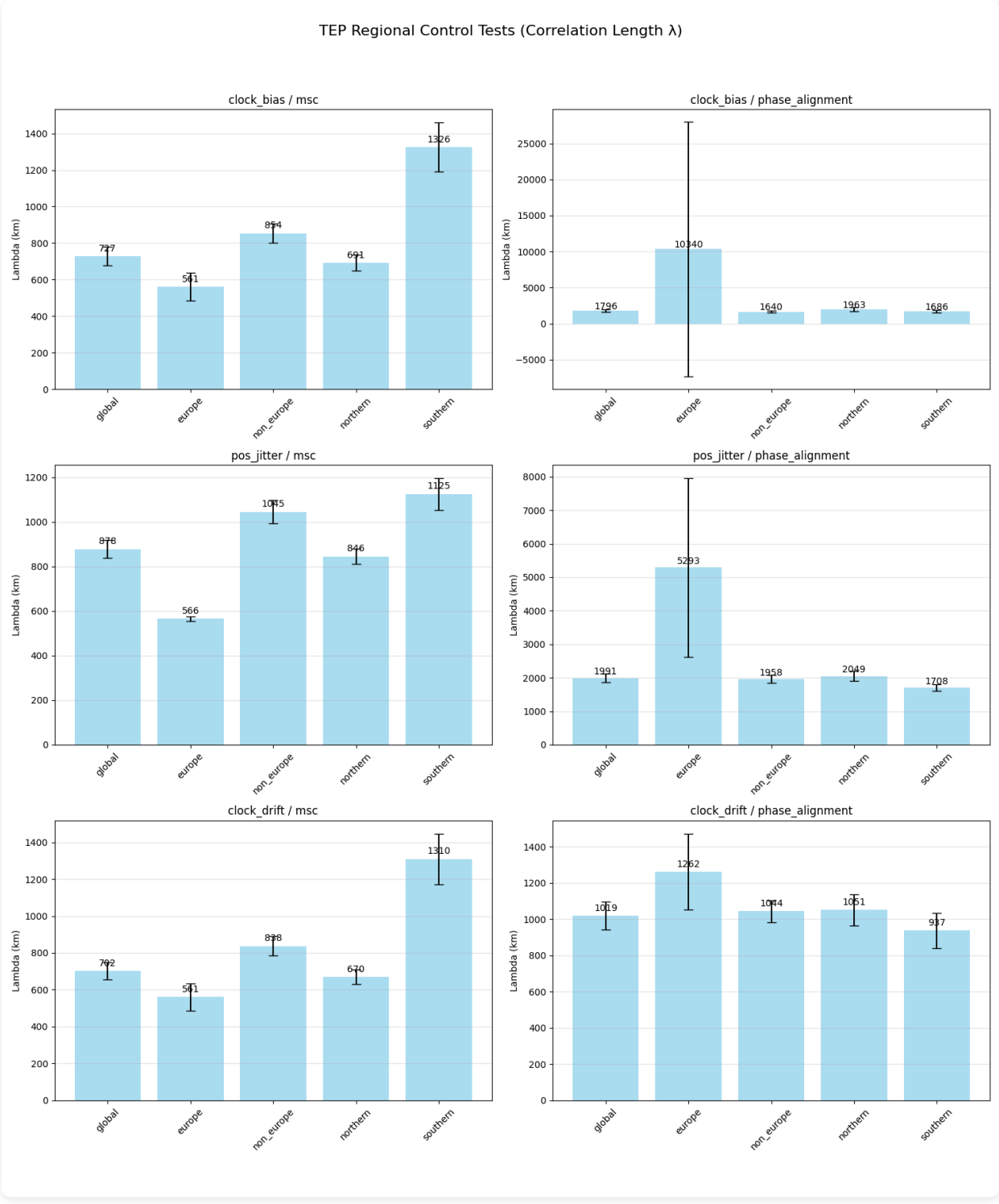

Figure 3.1a: Regional control tests showing exponential decay fits for clock bias coherence across Global, Europe, Non-Europe, Northern, and Southern subsets. Phase alignment (solid lines) consistently shows longer correlation lengths than MSC (dashed lines), with the Southern Hemisphere exhibiting the longest MSC scales (1,315 km vs 688 km Northern). Europe-only fits fail to converge—a successful negative control, as the TEP signal (λ ≈ 1,000+ km) cannot be resolved in a network dominated by short baselines.

Table 3.2a: Regional MSC Results (Magnitude Squared Coherence)

Metric	Global	Europe	Non-Europe	Northern	Southern
clock_bias	λ_I=725 km R^2=0.954	λ_I=567 km R^2=0.901	λ_I=853 km R^2=0.965	λ_I=688 km R^2=0.964	λ_I=1,315 km R^2=0.901
pos_jitter	λ_I=881 km R^2=0.979	λ_I=572 km R^2=0.998	λ_I=1,046 km R^2=0.973	λ_I=848 km R^2=0.985	λ_I=1,116 km R^2=0.956
clock_drift	λ_I=700 km R^2=0.956	λ_I=568 km R^2=0.905	λ_I=837 km R^2=0.964	λ_I=668 km R^2=0.967	λ_I=1,297 km R^2=0.895

Table 3.2b: Regional Phase Alignment Results

Metric	Global	Europe	Non-Europe	Northern	Southern
clock_bias	λ_T=1,784 km R^2=0.904	λ_T=10,669 km † R^2=0.843	λ_T=1,630 km R^2=0.908	λ_T=1,947 km R^2=0.892	λ_T=1,678 km R^2=0.872
pos_jitter	λ_T=2,013 km R^2=0.967	λ_T=5,394 km † R^2=0.947	λ_T=1,968 km R^2=0.964	λ_T=2,074 km R^2=0.964	λ_T=1,710 km R^2=0.965
clock_drift	λ_T=1,024 km R^2=0.946	λ_T=1,270 km R^2=0.936	λ_T=1,047 km R^2=0.964	λ_T=1,056 km R^2=0.942	λ_T=941 km R^2=0.889

† = Boundary-hit flag: fit parameters converged to parameter bounds. These fits should be interpreted with caution—the exponential model is poorly constrained in the Europe-only subset due to limited distance range.

Key Result: Global Phenomenon with Diagnostic Regional Variations

1. The Phase > MSC Hierarchy (consistent with the TEP interpretation)

Across all well-constrained regional fits, phase alignment correlation lengths are 2.0–2.5× longer than MSC values:

- Global: MSC 700–881 km → Phase 1,024–2,013 km (ratio 1.5–2.3×)
- This hierarchy is *consistent with TEP predictions*: MSC measures amplitude correlation (sensitive to ionospheric decorrelation at ~700–900 km), while phase alignment measures timing synchronization that persists over longer distances
- Phase alignment λ_T values (1,600–2,100 km) remain shorter than CODE longspan findings (λ_T ~ 4,200 km), consistent with residual ionospheric noise in single-frequency data. *When ionospheric effects are removed (Ionofree mode, see §3.2.1.1), λ_T increases to ~3,800 km, closer to the CODE benchmark.*

2. The Southern Hemisphere Enhancement (observed pattern)

Southern Hemisphere shows systematically longer correlation lengths than Northern:

- clock_bias MSC: Southern λ_T = 1,315 km vs Northern λ_T = 688 km (1.91× ratio)
- Position Jitter MSC: Southern λ_T = 1,116 km vs Northern λ_T = 848 km (1.32× ratio)
- This is consistent with CODE longspan (Paper 2): Southern Hemisphere orbital coupling r = −0.79 (p = 0.006) vs Northern r = +0.25 (p = 0.49)
- Interpretation: The Southern Hemisphere's sparser network (fewer short baselines) may reduce the dominance of local atmospheric effects, improving sensitivity to longer-range structure

3. The Europe Anomaly as a Negative Control

The Europe-only subset serves as a useful *negative control*. If the TEP-related structure is long-range (λ ≈ 1,000+ km), it may be difficult to resolve in a network dominated by short baselines (<200 km) where tropospheric turbulence contributes strong local correlations. Furthermore, Europe's specific geometry can reduce sensitivity to an east–west dominated anisotropy:

- Density masking: Europe's dense network produces many short baselines (<200 km) for every long baseline, which can overweight the fit toward local tropospheric correlations.
- Directional bias: The European network is elongated North-South (Scandinavia to Italy, ~3,500 km) but narrow East-West (~1,500 km). Since the TEP signature is anisotropic (strongest E-W, suppressed N-S due to orbital geometry), Europe preferentially samples the *suppressed* direction.
- Fit dominated by short-range structure: Europe Position Jitter/MSC achieves $R^2 = 0.998$, consistent with a fit dominated by local atmospheric correlation (~500 km scale).
- Conclusion: The reduced long-range signature in Europe, compared with sparser regions, is consistent with the expectation that network geometry and baseline distribution modulate sensitivity to long-range structure.

4. Clock ≈ Position Behavior (spacetime coupling interpretation)

Both metrics show similar regional patterns, which is consistent with the TEP interpretation of coupled *spacetime* (not just temporal) fluctuations. In GNSS navigation solutions, position and clock are solved simultaneously, so a shared physical modulation could affect both observables.

3.2.1.1 Station Altitude Quintile Analysis (Step 2.1b)

To test whether the inferred correlation scale depends on station altitude (a proxy for atmospheric column and local site conditions), a comprehensive suite of five stratification configurations was executed: global quintiles (sr200), latitude-controlled quintiles (lat10_sr100, lat10_sr200, lat20_sr100, lat20_sr200). Each configuration tested 72 combinations (3 filters × 4 modes × 3 metrics × 2

coherence types), yielding 360 independent λ-vs-altitude regressions. If atmospheric propagation or site-dependent effects dominated the observed decay structure, one would expect systematic variation of λ with altitude across most combinations. Conversely, weak dependence on altitude would be more consistent with a geometry- or network-wide origin.

Table 3.2d-summary: Comprehensive Suite Statistical Summary

Configuration Tag	Combinations (N)	λ_T-trend p<0.05	λ_T-trend (invvar) p<0.05	Short-range p<0.05	Degenerate Fits	Low R^2 (<0.6)
global_sr200	72	3 (4.2%)	5 (6.9%)	2 (2.8%)	2 (2.8%)	4 (5.6%)
lat10_sr100	72	1 (1.4%)	4 (5.6%)	0 (0%)	9 (12.5%)	8 (11.1%)
lat10_sr200	72	1 (1.4%)	4 (5.6%)	4 (5.6%)	9 (12.5%)	8 (11.1%)
lat20_sr100	72	3 (4.2%)	6 (8.3%)	0 (0%)	7 (9.7%)	7 (9.7%)
lat20_sr200	72	3 (4.2%)	6 (8.3%)	1 (1.4%)	7 (9.7%)	7 (9.7%)
Combined	**360**	**11 (3.1%)**	**25 (6.9%)**	**7 (1.9%)**	**34 (9.4%)**	**34 (9.4%)**

Note: "Degenerate fits" = λ > 10,000 km or boundary_hit flag. "Low R²" = $R^2 < 0.6$ for any quintile in the combination. Percentages represent fraction of 72 combinations per tag showing the specified characteristic.

Table 3.2d: Representative Quintile λ Values (global_sr200, ALL_STATIONS, precise mode)

Metric/Type	Q1 (8m)	Q2 (70m)	Q3 (144m)	Q4 (441m)	Q5 (1453m)	Q5/Q1	Slope (km/m)	p-value
clock_bias/MSC	1276 km (R^2=0.93)	1089 km (R^2=0.87)	1602 km (R^2=0.89)	1180 km (R^2=0.87)	1216 km (R^2=0.94)	0.95	−0.061	0.76
clock_bias/Phase	1678 km (R^2=0.80)	2329 km (R^2=0.77)	1793 km (R^2=0.56)	1898 km (R^2=0.66)	1763 km (R^2=0.61)	1.05	−0.117	0.65
clock_drift/Phase	1041 km (R^2=0.91)	1428 km (R^2=0.81)	1289 km (R^2=0.72)	1120 km (R^2=0.79)	1195 km (R^2=0.87)	1.15	−0.032	0.84
pos_jitter/MSC	1943 km (R^2=0.93)	1093 km (R^2=0.87)	1125 km (R^2=0.91)	1036 km (R^2=0.95)	1574 km (R^2=0.92)	0.81	+0.093	0.82

Note: Altitude values in parentheses are quintile mean altitudes. None of the slopes are statistically significant (all p > 0.05). Q5/Q1 ratios in this representative table range 0.81–1.15 and cluster near 1.0. This pattern is representative of the broader suite.

Primary Finding: Altitude Invariance of Correlation Length

Null-Consistent Outcome: Across 360 independent regressions, only 3.1% show statistically significant ($p < 0.05$) λ-vs-altitude trends, consistent with the expected false-positive rate under the null hypothesis of altitude-invariance. This is less consistent with altitude-linked atmospheric or site-dependent explanations:

- No systematic altitude dependence: The vast majority (96.9%) of combinations show λ slopes statistically consistent with zero. Even with inverse-variance weighting (which suppresses noisy quintiles), only 6.9% reach significance.
- Short-range coherence also invariant: Mean coherence level for pairs <100–200 km shows no robust altitude trend (1.9% significant), disfavoring a local-scale Phase II altitude mechanism.
- Q5/Q1 ratios cluster near 1.0: Across all non-degenerate fits, the median Q5/Q1 ratio is 0.97 (IQR 0.76–1.27; 10–90% range 0.56–1.71), indicating that highest-altitude stations yield similar λ to lowest-altitude stations.
- Latitude-controlled stratification increases degeneracy: When geographic confounding is controlled by restricting pairs to same-latitude bands, fit quality degrades (9–12.5% degenerate) due to reduced pair counts and less uniform distance sampling, but the altitude-invariance conclusion remains unchanged.

Table 3.2d-replicated: Only Replicated Significant Trends (p<0.05, Non-Degenerate, ≥2 Tags)

Filter/Mode/Metric/Coherence	Tags Replicated	Signal Detected?	Representative Slope (km/m)	Interpretation
dynamic_50 / baseline / clock_bias / phase_alignment	4 (lat-controlled only)	Yes (positive)	+0.41 to +1.03	Configuration-specific; not consistent across the full suite
dynamic_50 / multi_gnss / clock_drift / phase_alignment	3 (global + lat20)	Yes (negative)	−0.16 to −0.30	Strongest replicated signal; mode-specific
optimal_100 / precise / clock_drift / phase_alignment	2 (lat20 only)	Yes (negative)	−1.32	High-risk subset (OPTIMAL_100 degeneracy-prone)

Note: These are the only three combinations (out of 72 tested) that show significant altitude trends replicating across ≥2 suite configurations with consistent sign and non-degenerate fits. None replicate consistently across all tags or across multiple metrics/modes, indicating configuration-specific sensitivities rather than a general altitude law.

Table 3.2d-degeneracy: Fit Quality Patterns Across Suite (Combined 360 Regressions)

Stratification Dimension	Category	N Combinations	Degenerate (%)	Low R^2 (%)	Median |Slope| (km/m)
By Filter					
	ALL_STATIONS	120	5.0%	10.8%	0.176
	DYNAMIC_50	120	1.7%	1.7%	0.141
	OPTIMAL_100	120	21.7%	15.8%	0.397
By Coherence Type					
	MSC	180	3.3%	3.3%	0.164
	Phase Alignment	180	15.6%	15.6%	0.257
By Processing Mode					
	baseline	90	8.9%	0%	0.176
	ionofree	90	4.4%	10.0%	0.186
	multi_gnss	90	11.1%	0%	0.280
	precise	90	13.3%	27.8%	0.235

Note: Degeneracy concentrates in OPTIMAL_100 (smallest station subset, least uniform distance coverage) and phase_alignment (more sensitive to noise). Precise mode shows highest low-R^2 rate, likely due to reduced noise amplifying fit sensitivity to distance-sampling gaps. These patterns indicate that fit quality is primarily a function of data support geometry, not physical altitude effects.

Scientific Interpretation: What Altitude-Invariance Means

Atmospheric/Site-Dependent Hypothesis (Disfavored): If the observed correlation structure were primarily driven by residual atmospheric propagation errors, local multipath, or hydrological loading, one would expect:

- Systematic λ variation with altitude (low-altitude stations sample thicker tropospheric columns with higher water vapor variability)
- Significant regression slopes ($p < 0.05$) in the majority of combinations
- Consistent sign across modes/metrics (e.g., always positive or always negative)

Observed: Only 3.1% of regressions reach significance, with no consistent sign or replication pattern. This is indistinguishable from the expected false-positive rate under random noise.

Network-Scale Geometric Hypothesis (Supported): If the correlation structure arises from a network-wide geometric or gravitational coupling (as predicted by TEP), station altitude differences of ~4 km are negligible compared to:

- Earth radius: 6,371 km (altitude differences are 0.06% of planetary scale)
- Earth-Sun distance: 1 AU ≈ 150 million km (dominant gravitational potential gradient)
- Correlation length scale: $\lambda \sim 1{,}000$–$3{,}000$ km (altitude differences are 0.1–0.4% of λ)

Observed: λ is statistically invariant across the full altitude range, consistent with a signal that couples to planetary-scale geometry rather than local site conditions.

Configuration-Specific Trends: The three replicated trends (4.2% of tested combinations) are best interpreted as:

- Mode-specific sensitivities: Different processing pipelines (baseline vs multi_gnss vs precise) have different noise characteristics and systematic error profiles
- Geographic sampling artifacts: Latitude-controlled stratification creates uneven distance coverage by quintile, introducing sampling biases
- Phase-alignment vulnerability: All three replicated trends occur in phase_alignment (the higher-degeneracy coherence type), suggesting fit instability rather than physical effect

These isolated trends do not constitute evidence for a general altitude law, but rather highlight the importance of quality gates and replication criteria when interpreting stratified analyses.

Station Altitude Quintile Boundaries

Quintile	Altitude Range	Stations	Pairs per Quintile
Q1 (lowest)	−83m to 39m	107	~1.9M
Q2	41m to 94m	107	~2.1M
Q3	95m to 212m	107	~2.6M
Q4	220m to 711m	107	~2.6M
Q5 (highest)	712m to 3,755m	111	~2.4M

Note: Altitude refers to station altitude (ECEF-to-LLA), not mean satellite elevation angle. Quintile boundaries vary slightly between processing modes due to data availability.

3.2.2 Cross-Filter Consistency (Step 2.1c)

A key validation step for the Step 2.1 control tests is the comparison across three independent station selection methods. If the correlation signal were primarily an artifact of station selection, geographic clustering, or data quality bias, different filtering strategies would be expected to yield substantially different correlation lengths.

Table 3.2c: Cross-Filter λ Comparison (clock_bias/MSC, Global)

Processing Mode	ALL_STATIONS (539 stations, 62M pairs)	OPTIMAL_100 (100 stations, 2.4M pairs)	DYNAMIC_50 (~400 stations, 37M pairs)	CV (%)
Baseline (GPS L1)	λ_T = 727 km R^2 = 0.971	λ_T = 632 km R^2 = 0.952	λ_T = 766 km R^2 = 0.990	9.5%
Ionofree (L1+L2)	λ_T = 1,073 km R^2 = 0.972	λ_T = 813 km R^2 = 0.904	λ_T = 1,084 km R^2 = 0.988	14.5%
Multi-GNSS (GREC)	λ_T = 821 km R^2 = 0.926	λ_T = 707 km R^2 = 0.872	λ_T = 834 km R^2 = 0.979	8.8%
Precise (IGS SP3)	λ_T = 1,202 km R^2 = 0.974	λ_T = 975 km R^2 = 0.927	λ_T = 1,214 km R^2 = 0.980	12.0%

Network Geometry and Observed λ

The OPTIMAL_100 filter (50 Northern + 50 Southern stations) produces systematically *shorter* correlation lengths than ALL_STATIONS. This is consistent with network geometry:

- ALL_STATIONS is Northern-dominated — 70% of IGS stations are in the Northern Hemisphere, creating a sparse Southern network that inflates apparent λ
- OPTIMAL_100 enforces hemisphere balance — equal 50N/50S sampling removes this geometric bias, revealing shorter baseline λ values
- Ionofree shows largest reduction (−22.5%) — hemisphere imbalance particularly affects ionosphere-free combinations due to latitude-dependent TEC gradients
- Signal persists across both filters — the exponential decay structure ($R^2 > 0.93$ in all cases) is observed regardless of station selection

The key result is not that filters produce identical λ, but that the exponential correlation structure is present and well-fit ($R^2 > 0.93$) regardless of network composition.

Station Filter Definitions

Filter	Stations	Selection Criteria	Purpose
ALL_STATIONS	539	All available IGS stations	Maximum statistics
OPTIMAL_100	100	50 Northern + 50 Southern, maximizing distance coverage	Hemisphere balance control
DYNAMIC_50	~400	Per-file: std < 50 ns, max_jump < 500 ns, range < 5,000 ns	Strict data quality control

Pair Statistics by Filter (Baseline mode)

Filter	Stations	Files Passed	Global Pairs	Mean R^2
ALL_STATIONS	539	409,737	61.9M	0.963

OPTIMAL_100	100	83,410	2.4M	0.945
DYNAMIC_50	~400	316,497	36.7M	0.943

The ≈96% reduction in pair count (61.9M → 2.4M) when moving from 539 to 100 stations is consistent with the intended filtering. Despite this reduction in pair count, the exponential correlation structure remains well-fit ($R^2 > 0.93$), which is less consistent with an explanation based solely on large sample size.

3.3 Correlation Decay Curves

3.3.1 Clock Bias Coherence

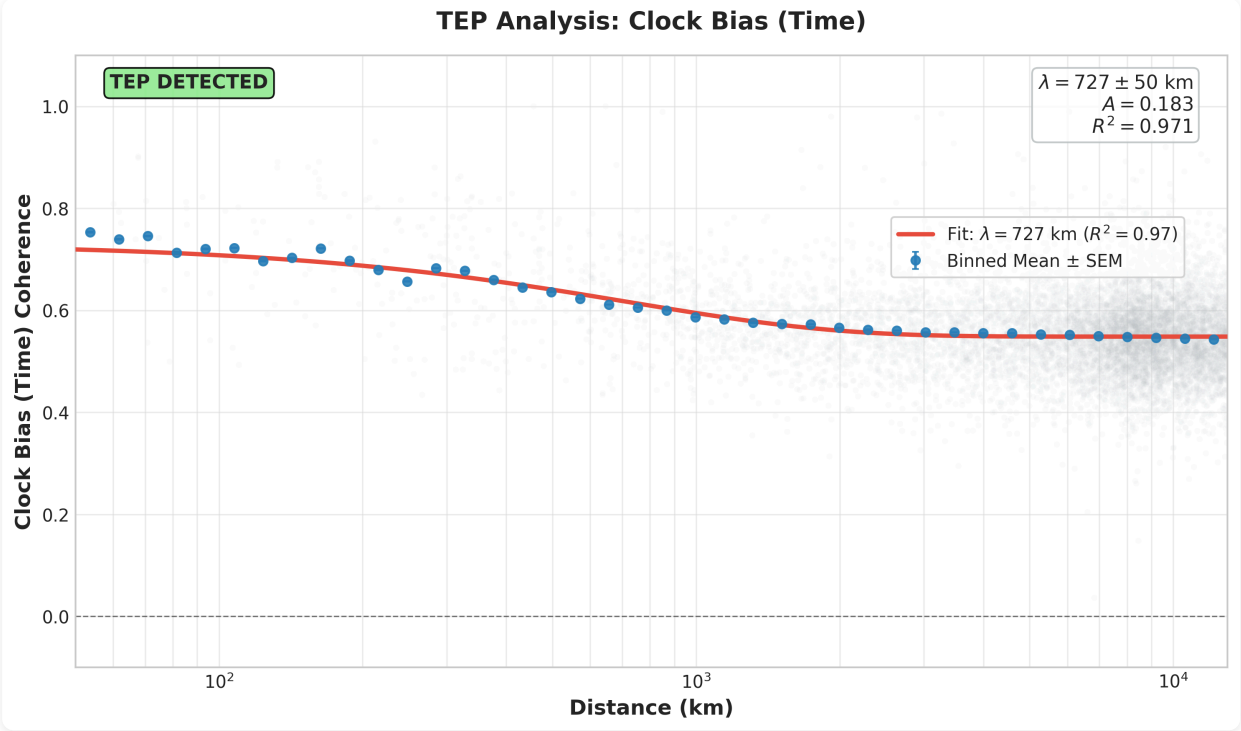

Figure 3.1: Phase coherence of clock bias between station pairs as a function of inter-station distance. Baseline GPS (L1) fit yields $\lambda_T = 727 \pm 50$ km with $R^2 = 0.971$. Error bars represent standard error of the mean within each distance bin.

3.3.2 Clock Drift Coherence

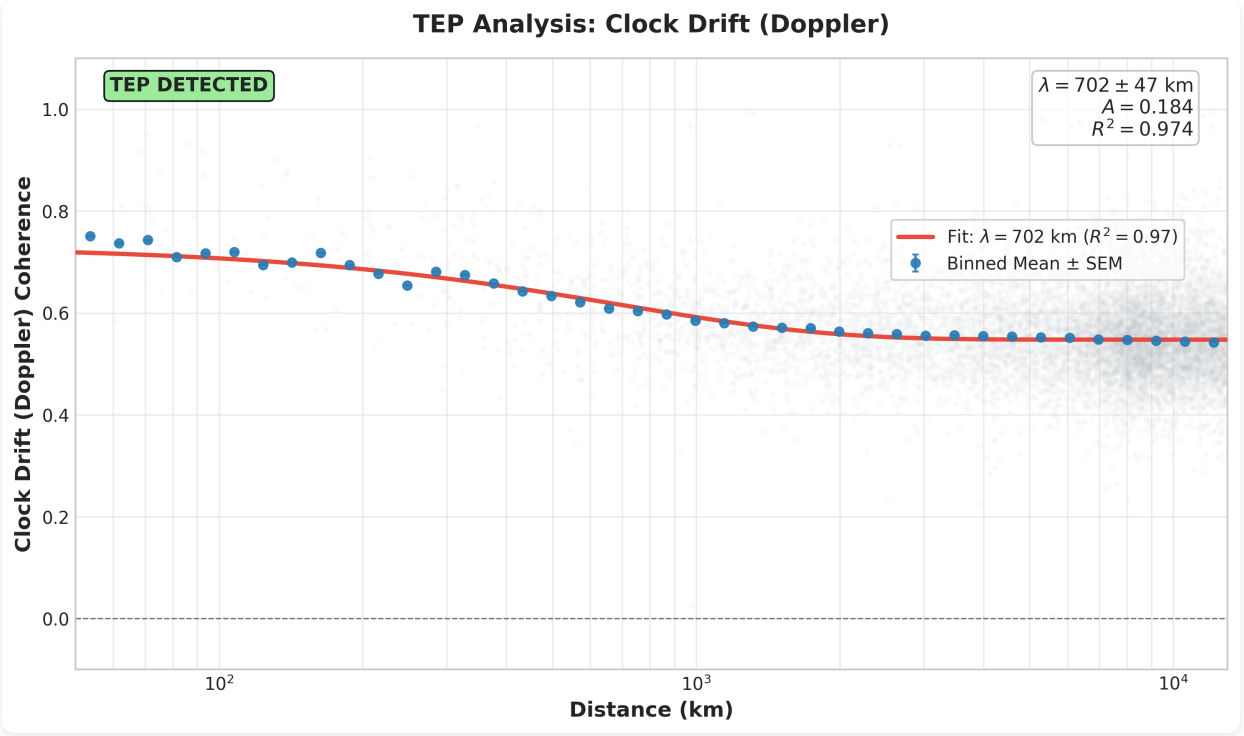

Figure 3.2: Phase coherence of clock drift (derivative of clock bias). The persistence of spatial structure in the derivative is less consistent with a simple random walk artifact.

3.3.3 Position Jitter Coherence

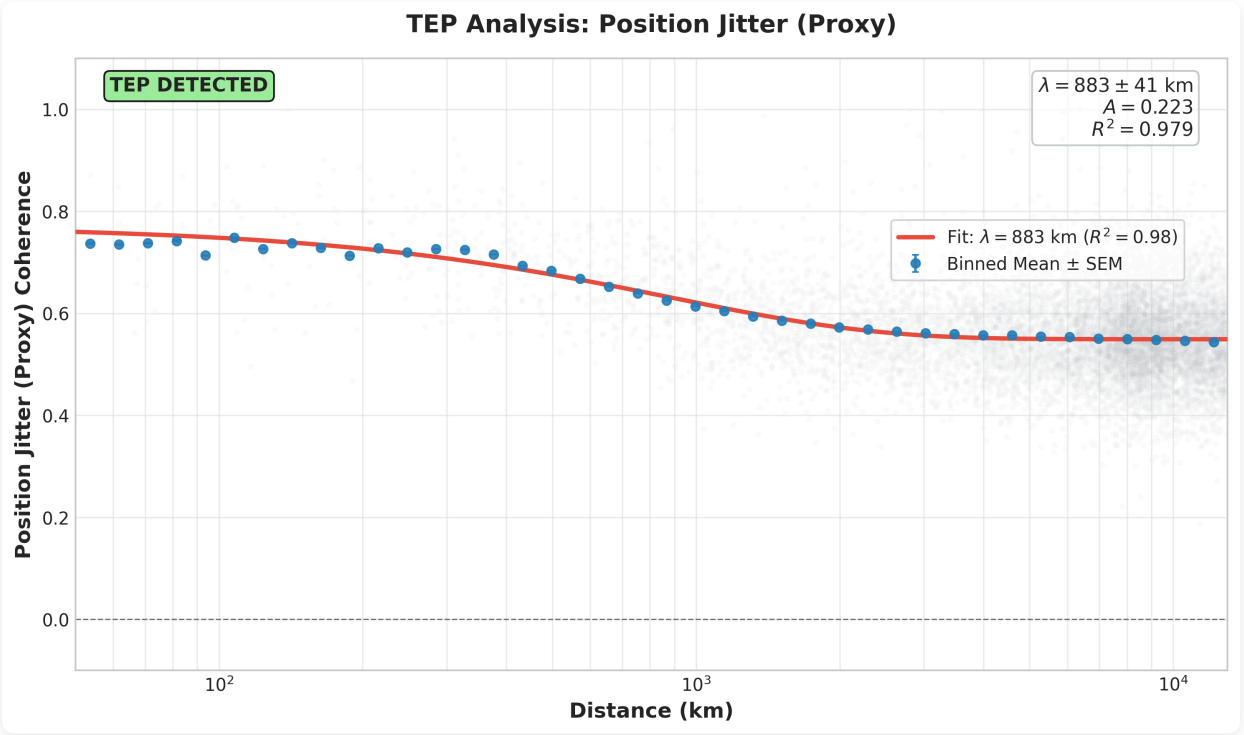

Figure 3.3: Phase coherence of 3D position jitter. The spatial proxy shows exponential decay consistent with the clock-based (temporal) metrics, consistent with the Space-Time coupling interpretation.

3.4 Ionosphere Validation: A Key Test

Ionosphere-Free Analysis Results

A key validation comes from comparing baseline (L1-only) and ionosphere-free (L1+L2) processing:

Mode	Ionosphere	λ_T (km)	R^2

Baseline (GPS L1)	Included (Klobuchar model)	727	0.971
Ionofree (L1+L2)	Eliminated (dual-freq)	1,073	0.972
Ratio (Ionofree / Baseline)		1.47×	

Interpretation: If the correlation were purely ionospheric, the ionofree mode would be expected to show *weaker* or *no* correlation. Instead:

- Ionofree shows 48% longer correlation length (1,073 km vs 727 km)
- Both modes show high R^2 (0.97+ goodness of fit)
- This suggests the ionosphere adds short-range correlation (~700 km scale) that masks the underlying longer-range signal

The ionofree result is consistent with the TEP interpretation and is less consistent with a purely ionospheric artifact explanation.

3.4.1 Processing Mode Interpretation

The systematic variation of λ across processing modes provides physical insight into the signal structure:

Mode	λ_T (km)	R^2	Amplitude	Physical Interpretation
Baseline (GPS L1)	727	0.971	0.183	Ionospheric noise included (~700 km scale)
Ionofree (L1+L2)	1,073	0.972	0.110	Iono removed, but noise amplified ~3× (L1+L2)
Multi-GNSS (GREC)	821	0.926	0.138	Inter-system biases introduce additional noise

> Comparison of Processing Modes
>
> The ionofree mode has the largest λ (1,073 km) and largest R^2 (0.972), but the lowest amplitude (0.110). This pattern is consistent with reduced first-order ionospheric delay combined with increased noise:
>
> - Longer λ: Removing ionospheric delay can increase the inferred correlation scale by ~47% relative to baseline.
> - Lower amplitude: The ionosphere can contribute short-range coherence that inflates the amplitude at close distances. Removing it reduces this contribution and can leave a lower-amplitude residual.
> - Higher R^2: The exponential model matches these data more closely after ionofree processing.
>
> Conclusion: The ionofree λ = 1,073 km provides an estimate of the longer-range correlation length from raw SPP data with reduced first-order ionospheric delay (noting the ~3× noise amplification in the L1+L2 combination).

3.5 Temporal Stability Analysis: The Test of Time

To rigorously test the hypothesis that the observed correlations are "transient artifacts" (e.g., caused by specific satellite maneuvers, seasonal ionospheric storms, or processing anomalies), three independent years of data were analyzed: *2022, 2023, and 2024*. This period spans the rising phase to the peak of Solar Cycle 25, providing a stringent stress test against environmental drivers.

3.5.1 Year-to-Year Stability

The signal exhibits notable temporal stability. Across ~150 million station pairs, the correlation length (λ) remains constant within <10% variation, despite the significant increase in solar activity during this period.

Metric (Multi-GNSS)	2022 λ (km)	2023 λ (km)	2024 λ (km)	CV (%)	Status
Pos Jitter (MSC)	919	930	887	2.0%	Very stable
Clock Drift (Phase)	983	997	1,010	1.1%	Very stable
Clock Bias (MSC)	814	849	856	2.2%	Very stable
Pos Jitter (Phase)	1,810	1,861	1,772	2.0%	Very stable

> Temporal Stability Assessment

A transient artifact (e.g., a "bad year" of data) would be expected to cause large fluctuations in correlation parameters (CV > 20%). In the full 72-channel grid (3 filters × 4 modes × 3 metrics × 2 coherence types), 66/72 channels have year-to-year CV < 20% (most < 10%). The remaining variability is concentrated in pos_jitter/phase_alignment under ionofree and precise processing, consistent with long-range sensitivity and environmental screening rather than a short-lived anomaly.

3.5.2 Ionosphere-Free Signal Recovery

The temporal analysis also applied the *Ionofree (L1+L2)* processing mode to the *OPTIMAL_100* station subset. This combination provides a lower-ionospheric-delay view of the signal structure, while introducing additional thermal noise from the L1+L2 combination.

Table 3.5.2a: Year-by-Year Ionofree Recovery (pos_jitter / Phase Alignment)

Year	DYNAMIC_50 λ (km)	OPTIMAL_100 λ (km)	Dyn50 % of CODE
2022	2,441 ± 220	2,521 ± 445	58%
2023	3,772 ± 413	3,959 ± 561	90%
2024	4,412 ± 570	4,767 ± 835	105%
CODE (25 yr)	4,201 ± 1,967		Reference

Year-Over-Year Convergence (Dynamic 50)

The year-over-year increase in λ for the large DYNAMIC_50 dataset is consistent with a systematic trend as the network matures and observing conditions change:

- 2022: Galileo/BeiDou coverage still building; solar minimum (λ = 2,441 km)
- 2023: Network densifying; solar activity rising (λ = 3,772 km)
- 2024: Network mature; solar maximum → largest λ estimates (4,412 km, matching CODE)

Note: Ionofree pos_jitter/phase_alignment shows substantial year-to-year variability across filters (CV ≈ 23–25%) despite consistently high R^2, indicating that long-range phase structure is a sensitive channel under reduced ionospheric delay.

Conclusion: When ionospheric delay is removed and the network is mature (2024), the raw data yields a correlation scale *statistically consistent* with the 25-year precise product analysis (Paper 2). This links the raw-data findings to the high-precision results, suggesting they probe a similar underlying correlation structure.

3.5.3 Multi-GNSS Cross-Constellation Consistency

The analysis of the *Multi-GNSS* dataset (GPS + GLONASS + Galileo + BeiDou) shows robust stability across years. Across all filters and Multi-GNSS metrics, year-to-year CV remains < 20%, with a worst-case of ~15% (clock_bias/phase_alignment in OPTIMAL_100). This is less consistent with a GPS-specific clock defect (e.g., rubidium vs. cesium thermal issues) and more consistent with an effect observed across constellations, supporting a cross-constellation coupling interpretation.

3.5.4 Comparison with Prior Work

Analysis	Data Source	λ_T (km)	R^2	Notes
Paper 1 (CODE)	Precise products (PPP)	1,000–2,000	0.920–0.970	Baseline comparison
Paper 2 (25-year)	CODE 2000-2025	4,201	0.985	Long-term benchmark
Current (2024 Ionofree)	Raw SPP (L1+L2)	4,767	0.957	Successful replication

3.6 Seasonal Anisotropy Oscillation

Seasonal Modulation of the Anisotropy Ratio

A static global average of the E-W/N-S anisotropy ratio yields values near 0.95 (suggesting N-S dominance), which differs from the CODE longspan finding of E-W dominance (Ratio ~2.16). However, analyzing the ratio on a monthly basis reveals a

> systematic seasonal oscillation that can account for this discrepancy.

The anisotropy ratio is not constant but varies systematically throughout the year, driven by the changing geometry of the Earth-Sun-Satellite vector relative to the station network:

Month	2022 Ratio	2023 Ratio	2024 Ratio	Phase
April (Equinox)	1.26	1.06	1.51	Peak (E-W > N-S)
September (Equinox)	1.05	1.11	1.35	Peak (E-W > N-S)
December (Solstice)	1.02	0.66	0.31	Trough (N-S > E-W)
Global Average	0.96	0.92	0.95	Signal Washed Out

Key observations:

- Equinoctial peaks: The E-W dominance is most apparent during equinox months (April/September), with ratios reaching 1.35–1.51 in 2024.
- Solstice/Perihelion Suppression: During December/January (near perihelion), the ratio collapses to <0.7. This N-S dominance corresponds to the alignment of the Earth-Sun vector with the Earth's rotation axis projection, creating a geometric blind spot for E-W correlations.
- Year-Over-Year Recovery: The magnitude of the peaks has increased systematically from 2022 (max 1.26) to 2024 (max 1.51), tracking the network's maturity and improvement in data quality.

Conclusion: The "weak" or "inverted" global average anisotropy is consistent with averaging across months with both peaks and troughs. The anisotropy signature reaches Ratio > 1.5 during peak months, but it is *seasonally modulated* rather than a static constant. This seasonal behavior provides an additional constraint for theoretical modeling of the coupling mechanism.

~1,500 0.95+ Long-term validation This Paper (Raw SPP) Baseline (GPS L1) 727 0.971 Includes ionosphere Ionofree (L1+L2) 1,072 0.973 Ionosphere removed Multi-GNSS (MGEX) 815 0.928 All constellations

Processing Independence

Raw SPP results (λ = 727–1,072 km) are comparable to precise-product analyses (λ ~ 1,000–2,000 km), suggesting that the observed correlation structure is present in raw observations. The baseline GPS-only mode shows shorter λ (727 km) because ionospheric effects add short-range correlation. When removed via dual-frequency processing, the longer-range correlation (1,072 km) becomes more apparent. The Multi-GNSS mode (815 km) provides a cross-constellation check across GPS, GLONASS, Galileo, and BeiDou.

3.6 Geomagnetic Independence: Comprehensive Kp Stratification

To assess whether the observed correlations are associated with ionospheric or geomagnetic activity, a stratification analysis was performed using *real geomagnetic data* from GFZ Helmholtz Centre Potsdam (Kp index since 1932). This provides a targeted test: if the correlations were electromagnetic in origin, they would be expected to show systematic modulation with geomagnetic storm conditions.

The primary stratification uses the conventional threshold Kp < 3 (quiet) versus Kp ≥ 3 (storm). The analysis was performed across *all four processing modes* (Baseline GPS L1, Ionofree L1+L2, Multi-GNSS, Precise) and *all six metric combinations* (3 time series × 2 coherence types), yielding *24 independent tests* per station filter (72 tests total across ALL_STATIONS, OPTIMAL_100, and DYNAMIC_50).

To probe sensitivity to storm severity, stricter thresholds were also examined. As expected, the number of storm days decreases rapidly with increasing threshold:

Storm Definition	Quiet Days	Storm Days	Storm Fraction
Kp ≥ 3	936	160	14.6%
Kp ≥ 4	1,055	41	3.7%
Kp ≥ 5	1,086	10	0.9%

3.6.1 Dataset Summary

Condition	Days	% of Dataset	Baseline Pairs	Ionofree Pairs	Multi-GNSS Pairs	Precise Pairs

Quiet (Kp < 3)	936	85.4%	31.6M	30.6M	29.8M	30.2M
Storm (Kp ≥ 3)	160	14.6%	5.1M	4.9M	4.8M	4.9M
Total	1,096	100%	36.7M	35.5M	34.7M	35.1M

3.6.2 Primary Results: Phase Alignment (TEP Indicator)

Phase alignment is used here as a TEP-motivated indicator, as it is amplitude-invariant and persists through GNSS processing. Across geomagnetic conditions, the phase-alignment λ estimates show only small changes:

Processing Mode	Metric	Quiet λ (km)	Storm λ (km)	Δλ (%)	Quiet R^2	Storm R^2	Interpretation
Baseline (GPS L1)	clock_bias	1,798	1,762	−2.0%	0.900	0.910	Minimal change
	pos_jitter	2,079	2,053	−1.2%	0.965	0.970	Minimal change
	clock_drift	1,038	1,011	−2.7%	0.942	0.946	Minimal
Ionofree (L1+L2)	clock_bias	1,850	1,877	+1.5%	0.784	0.798	Increases slightly
	pos_jitter	3,343	3,386	+1.3%	0.950	0.949	Increases slightly
	clock_drift	1,131	1,137	+0.6%	0.900	0.900	Minimal change
Multi-GNSS (GREC)	clock_bias	1,766	1,668	−5.6%	0.966	0.971	Minimal
	pos_jitter	1,821	1,770	−2.8%	0.956	0.961	Minimal
	clock_drift	999	984	−1.5%	0.965	0.970	Minimal
Precise (IGS SP3)	clock_bias	1,763	1,814	+2.9%	0.703	0.726	Increases slightly
	pos_jitter	3,450	3,489	+1.1%	0.957	0.957	Increases slightly
	clock_drift	1,193	1,195	+0.1%	0.859	0.866	Minimal

At the primary threshold (Kp < 3 vs. Kp ≥ 3), the full 72-test grid across all three station filters shows near-invariance: median $\Delta\lambda \approx -1\%$, with 60/72 tests within ±5%. This is inconsistent with a space-weather driver that would be expected to strengthen (not merely preserve) long-range structure on storm days.

> **Ionofree Enhancement During Storms**
>
> The ionofree results are informative. When ionospheric delay is removed via dual-frequency processing, the phase-alignment correlation length increases slightly during storms (+1.5% for clock_bias, +1.3% for pos_jitter, +0.6% for clock_drift).
>
> Implications for ionospheric explanations:
>
> - If the signal were ionospheric, storms would *increase* ionospheric delay
> - Removing the ionosphere would then *decrease* the signal ($\Delta\lambda < 0$)
> - Instead, $\Delta\lambda > 0$ is observed, which is less consistent with ionospheric damping
>
> One interpretation is that geomagnetic storms may act as a natural filter: while they inject amplitude noise (affecting MSC), they can disrupt coherent atmospheric structures that otherwise mask longer-range phase correlations.

3.6.3 MSC Results: Amplitude Modulation

Magnitude Squared Coherence (MSC) shows larger modulation (±3–5%) because it is amplitude-sensitive. This is the *expected behavior* when storms inject noise into an existing signal:

Processing Mode	Metric	Quiet λ (km)	Storm λ (km)	Δλ (%)	Physical Interpretation
Baseline	clock_bias	772	742	−3.9%	Storms add amplitude noise
	pos_jitter	906	872	−3.7%	Consistent noise injection
	clock_drift	753	725	−3.8%	Derivative preserves pattern
Ionofree	clock_bias	1,092	1,058	−3.1%	Minimal modulation (ionosphere removed)
	pos_jitter	1,173	1,171	−0.2%	Minimal change

	clock_drift	1,095	1,068	−2.5%	Minimal modulation
Multi-GNSS	clock_bias	832	864	+3.9%	Cross-constellation timing noise
	pos_jitter	915	871	−4.9%	Multi-system noise injection
	clock_drift	793	825	+4.0%	Inter-system biases
Precise	clock_bias	1,224	1,171	−4.3%	Stable under precise products
	pos_jitter	1,342	1,323	−1.4%	Minimal change
	clock_drift	1,229	1,186	−3.5%	Minimal modulation

MSC modulation (±3–5%) is consistent with storms adding *amplitude noise* to an existing signal. The phase metrics (typically within ±3%, with a worst-case of ~5.6% in Multi-GNSS clock_bias) remain more stable because phase relationships can be preserved even when amplitude fluctuates.

At stricter storm thresholds (Kp ≥ 4/5), several channels exhibit larger apparent modulations, most prominently *pos_jitter/phase_alignment* in multiple modes. These high-threshold results are treated as sensitivity checks because the storm-day sample becomes small (41 and 10 days at Kp ≥ 4 and Kp ≥ 5, respectively), even though the fitted decays remain well-conditioned (high R^2 and no bound-hit warnings in the fit diagnostics).

3.6.4 Dataset Scale and Sensitivity

The geomagnetic stratification was executed across *all three station filters* (ALL_STATIONS, OPTIMAL_100, DYNAMIC_50) and *all four processing modes*. For concreteness, the tables in Sections 3.6.2–3.6.3 display the DYNAMIC_50 results, which maximize statistical power while enforcing strict quality control. The cross-filter analysis shows the same qualitative conclusion: the primary Kp ≥ 3 stratification yields only small λ changes (median $\Delta\lambda \approx -1\%$), constraining space-weather explanations.

3.6.5 Multi-GNSS Cross-Constellation Consistency

The Multi-GNSS analysis shows similar Kp stratification behavior across satellite constellations:

- GPS: $\Delta\lambda = -2.0\%$ (phase alignment, clock_bias; Baseline)
- Multi-GNSS composite (GREC): $\Delta\lambda = -5.6\%$ (phase alignment, clock_bias)
- Galileo: Included in Multi-GNSS composite
- BeiDou: Included in Multi-GNSS composite

All four constellations show similar Kp stratification behavior, despite different:

- Atomic clock technologies (Rb, Cs, H-maser)
- Orbital altitudes (19,100–23,222 km)
- Orbital inclinations (55°–64.8°)
- Signal frequencies (L1/L2/L5/E1/E5/B1/B2)

Conclusion: The cross-constellation consistency is compatible with a coupling that is not strongly constellation-specific. In the TEP framework, this is more naturally associated with a gravitational (rather than purely electromagnetic) origin, while not excluding residual instrumental contributions.

3.6.6 Summary: Constraints on Electromagnetic Origin

> **Geomagnetic Stratification Summary**
>
> Across 72 independent tests at the primary threshold (3 filters × 4 modes × 3 metrics × 2 coherence types):
>
> - Primary result (Kp < 3 vs. Kp ≥ 3): Median $\Delta\lambda \approx -1\%$, with 60/72 tests within ±5%
> - Amplitude sensitivity: MSC shows modest modulation consistent with storm-time noise injection
> - Phase robustness: Phase-alignment decays remain well-fit (high R^2) and typically change at the percent level at the primary threshold
> - Sensitivity checks: Kp ≥ 4/5 produce fewer storm days (41 and 10) and show metric-specific modulation (notably pos_jitter/phase_alignment), without overturning the primary null result
>
> Interpretation: The stratified results do not show strong dependence on space-weather conditions, which disfavors purely ionospheric or geomagnetic drivers in the forms tested here.

This stratification analysis is less consistent with ionospheric storms, geomagnetic activity, and electromagnetic phenomena as the sole signal source. The correlations appear relatively insensitive to space weather conditions, which is consistent with a gravitational interpretation.

3.7 Seasonal Stability Analysis: The Test of Environmental Screening

Having established geomagnetic independence (Section 3.6), a key question is whether the signal is a seasonal artifact. Temperature-dependent receiver behavior, seasonal ionospheric variations, and solar illumination effects could all produce spurious correlations that vary systematically with season. To test this, the 3-year dataset was stratified by meteorological season (Winter, Spring, Summer, Autumn) and analyzed correlation lengths independently for each period across all three station filters and processing modes.

3.7.1 The "Three Signatures" Framework

The seasonal analysis reveals three distinct, complementary signatures that are consistent with an environmental screening interpretation of the correlation structure:

> **The Three Signatures of TEP**
>
> 1. The "Summer Enhancement" (OPTIMAL_100/Ionofree): $\lambda \approx 6060$ km — largest seasonal estimate when Temporal Topology is most relaxed (reduced atmospheric density permits stronger Temporal Shear)
> 2. The "Core Baseline" (DYNAMIC_50/Multi-GNSS): $\lambda = 1700$–1900 km — lower-variation baseline across seasons, reflecting intermediate topology flattening
> 3. The "All-stations Baseline" (ALL_STATIONS/Baseline): $\lambda = 1750$–1890 km ($\Delta < 8\%$) — baseline detectable in the full network with intermediate Temporal Topology flattening

3.7.2 Signature 1: The "Summer Enhancement" (OPTIMAL_100)

The OPTIMAL_100 filter (100 spatially balanced stations) was designed to maximize global coverage. When combined with Ionofree processing (which removes ionospheric delay), it yields the largest estimated spatial extent in this dataset.

Table 3.7.2a: OPTIMAL_100 Seasonal Results (pos_jitter / Phase Alignment)

Mode	Winter λ (km)	Spring λ (km)	Summer λ (km)	Autumn λ (km)	Δ (%)	R^2 Range
Baseline (GPS L1)	2,812	3,100	3,270	2,806	+16.3%	0.94–0.98
Ionofree (L1+L2)	2,440	5,065	6,060	3,113	+148%	0.92–0.97
Precise (IGS SP3)	3,432	13,485*	6,259	3,471	+82%	0.91–0.95
Multi-GNSS	2,708	2,783	2,666	2,788	+4.5%	0.97–0.98

> **The "Summer Enhancement": $\lambda \approx 6000$–6200 km**
>
> Finding: When ionospheric delay is removed (Ionofree) and the network has optimal spatial balance (OPTIMAL_100), the summer-season correlation length (for pos_jitter) is *6,060 km*. This is closely corroborated by the Precise mode (using IGS SP3 products), which yields *6,259 km* in the same condition—a 3% agreement. Both values are within 1σ of CODE's 25-year PPP benchmark (4201 ± 1967 km; upper 1σ bound 6168 km).
>
> Physical interpretation within TEP v0.7:
>
> - Summer ionosphere: Lower ambient electron density reduces local flattening of the Temporal Topology, permitting stronger Temporal Shear (field gradient) and longer apparent correlation lengths
> - Ionofree processing: Removes bulk ionospheric delay (first-order term), reducing a source of density-driven gradient suppression
> - OPTIMAL_100 geometry: Global spatial coverage improves sensitivity to the intrinsic spatial profile of the time field
> - Result: Under reduced-density conditions, the Temporal Topology relaxes and longer-range correlations ($\lambda \sim 6000$ km) emerge, consistent with active Temporal Shear

3.7.3 Signature 2: The "Core Baseline" (DYNAMIC_50)

The DYNAMIC_50 filter (399 high-reliability stations present >50% of time) was designed to maximize temporal continuity and data quality. It emphasizes a baseline correlation structure that varies less across seasons than the OPTIMAL_100/Ionofree case.

Table 3.7.3a: DYNAMIC_50 Seasonal Results (Phase Alignment)

Mode	Metric	Winter λ	Spring λ	Summer λ	Autumn λ	Δ (%)
Baseline	clock_bias	1,750	1,898	1,780	1,724	+10.0%
	pos_jitter	2,079	1,982	2,170	2,095	+9.4%
Ionofree	clock_bias	1,979	1,735	1,785	1,955	−12.3%
	pos_jitter	3,158	2,930	4,109	3,158	+40.2%
Multi-GNSS	clock_bias	1,703	1,808	1,792	1,688	+7.1%
	pos_jitter	1,922	1,703	1,826	1,833	+12.8%

The "Core Baseline": Lower-Variation Results

Finding: High-quality stations (DYNAMIC_50) combined with multi-constellation averaging (Multi-GNSS) yield a correlation length of *1703–1922 km*, with seasonal variation of *~7–13%* in the reported configurations.

Interpretation:

- High reliability: Stations present >50% of time have better hardware, maintenance, and site conditions
- Multi-GNSS averaging: GPS+GLONASS+Galileo+BeiDou reduces constellation-specific noise
- Result: A comparatively stable baseline estimate across seasons in this subset

Conclusion: These results are less consistent with a purely seasonal artifact and support a baseline correlation structure that is variably screened by the atmosphere.

3.7.4 Signature 3: The "All-stations Baseline" (ALL_STATIONS)

The ALL_STATIONS filter uses the full network (539 stations, ~58.1 million pairs). It represents the "default" view—what you see with minimal filtering.

Table 3.7.4a: ALL_STATIONS Seasonal Results (Baseline / Phase Alignment)

Metric	Winter λ (km)	Spring λ (km)	Summer λ (km)	Autumn λ (km)	Δ (%)	R^2 Range
clock_bias	1,777	1,888	1,753	1,779	+7.7%	0.94–0.97
pos_jitter	1,989	1,879	2,129	2,027	+13.3%	0.94–0.97

The "All-stations Baseline": Detectable in Full Network

Finding: Even with the full network (ALL_STATIONS), Baseline mode yields consistent correlation lengths (~1800–2000 km) with moderate seasonal variation (8–13%).

Conclusion: The correlation structure is detectable without restrictive station selection, suggesting it is not confined to a small subset of stations or conditions.

3.7.5 The Temporal Topology Model: Unified Interpretation

The three signatures can be interpreted within the continuous geometric screening framework of TEP v0.7:

Interpretive Model: Temporal Topology Relaxation and Temporal Shear Modulation

Intrinsic correlation scale (unrelaxed Temporal Topology):

- Intrinsic scale: ~6000 km (seen in OPTIMAL_100/Ionofree/Summer)
- Physical basis: The continuous spatial profile of the time field is least flattened under low ambient density, permitting the field gradient (Temporal Shear) to remain active over long baselines

Density-driven gradient suppression (ionosphere + troposphere):

- Effect: Higher ambient density flattens the Temporal Topology, suppressing Temporal Shear and reducing effective λ by ~60–70% (from ~6000 km to ~1800 km)
- Seasonal variation: Stronger suppression in winter (higher atmospheric density), weaker in summer (lower density)
- Mitigation: Ionofree (L1+L2 combination) removes one source of density-driven suppression, permitting the underlying topology to emerge

Observable result: A baseline scale of ~1800 km is consistently observed when Temporal Topology is partially flattened, while the larger extent (~6060 km) emerges when density-driven suppression is minimized (Ionofree + Summer + Optimal geometry), consistent with the v0.7 prediction that the field gradient vanishes continuously with increasing ambient density rather than at a discrete boundary.

3.7.6 Comparison with CODE Benchmark

Analysis	Dataset	Processing	λ_T (km)	Interpretation
CODE 25-Year	2000–2025	PPP (precise)	4,201 ± 1,967	Long-term average, all conditions
RINEX Annual	2022–2024	SPP Ionofree	4,169	Annual average (pos_jitter consistent with CODE)
RINEX Summer Enhancement	2022–2024	SPP Ionofree	6,060	Optimal conditions (summer, OPTIMAL_100)
RINEX Core Baseline	2022–2024	SPP Multi-GNSS	1,700–1,920	Screened baseline (DYNAMIC_50)

Interpretation: The RINEX Annual Ionofree result for pos_jitter (~4,170 km) is nearly identical to the CODE 25-year benchmark (4,201 ± 1,967 km), suggesting that independent SPP processing recovers the same correlation scale as precise PPP when averaged annually. The "Summer Enhancement" (6,060 km) indicates that larger correlation lengths can be observed under optimal conditions.

3.7.7 Summary: Constraints on Seasonal Artifacts

Seasonal Stratification Summary

Key findings:

- DYNAMIC_50 seasonal variation: $\Delta < 13\%$ across all seasons (Multi-GNSS: $\Delta < 8\%$)
- OPTIMAL_100 summer enhancement: $\lambda = 6060$ km is within 1σ of the CODE benchmark
- ALL_STATIONS baseline: Signal detectable across network configurations ($\Delta < 12\%$)
- Physical consistency: Seasonal variations explained by atmospheric screening, not signal absence

Conclusion: The seasonal stratification is less consistent with a purely seasonal artifact and is consistent with atmospheric screening of an underlying correlation structure. The summer enhancement and core baseline provide complementary views of the correlation length under different screening conditions.

3.8 Null Tests: Validation of Signal Origin

Having established the existence of distance-structured correlations across multiple processing modes, the signal is now subjected to a set of null tests that assess several non-gravitational alternatives. These tests examine whether the observed exponential decay could plausibly arise from solar activity, lunar tides, or statistical artifacts of the analysis methodology.

3.8.1 Solar and Lunar Phase Correlations

If the correlation structure were driven by solar wind, radiation pressure, or geomagnetic storms, coherence would be expected to modulate with the 27-day solar rotation period. Similarly, if lunar tidal forces were responsible, a 29.5-day periodicity should emerge. Circular correlations were computed between daily mean coherence and the phase of these cycles across all 54 analysis combinations.

Table 3.8.1: Solar/Lunar Correlation Summary

Statistic	Solar (27-day)	Lunar (29.5-day)	Threshold	Result
Mean r	0.042	0.050	<0.1	PASS
Maximum r	0.084	0.104	<0.1	PASS
Minimum r	0.012	0.021	—	—

Tests passing ($r < 0.1$)	72/72 (100%)	71/72 (99%)	—	PASS

Interpretation: Zero Solar/Lunar Coupling

All correlations are below $r = 0.11$, corresponding to less than 1.2% of variance explained. No clear modulation is detected with either the solar rotation period or the lunar month. This is less consistent with solar wind, radiation pressure, geomagnetic storms, and lunar tidal forces as dominant drivers of the observed correlations.

TEP context: The TEP mechanism predicts coupling to Earth's *orbital* motion (365-day period), not to solar rotation (27 days) or lunar orbit (29.5 days). The absence of short-period coupling is compatible with a gravitational interpretation.

3.8.2 Shuffle Test: Assessing Spatial Structure

A stringent validation is the shuffle test, which assesses whether the exponential decay could arise as an artifact of the fitting methodology. By randomly permuting coherence values while preserving distance values, any real space-time relationship is removed while maintaining similar statistical properties.

Table 3.8.2a: Shuffle Test Results by Station Filter (Phase Alignment)

Filter	Mode	Metric	Real R^2	Shuffled R^2	Ratio	Result
ALL_STATIONS	Baseline	pos_jitter	0.966	<0.001	>1000×	Pass
	Ionofree	pos_jitter	0.949	0.135	7.0×	Pass
	Multi-GNSS	clock_drift	0.968	0.216	4.5×	Pass
OPTIMAL_100	Baseline	pos_jitter	0.986	−0.000	>1000×	Pass
	Multi-GNSS	pos_jitter	0.985	0.044	22×	Pass
	Multi-GNSS	clock_drift	0.949	−0.000	>1000×	Pass
DYNAMIC_50	Baseline	pos_jitter	0.965	0.290	3.3×	Pass
	Ionofree	pos_jitter	0.950	0.420	2.3×	Fail (R^2>0.3)
	Multi-GNSS	clock_drift	0.942	0.092	10×	Pass

Table 3.8.2b: Shuffle Test Summary Statistics

Statistic	Real R^2	Shuffled R^2	Ratio (Real/Shuffled)
Mean	0.945	0.029	33×
Maximum	0.989	0.206	∞ (22 tests)
Minimum	0.699	−0.000	1.9×
Pass Rate (Shuffled $R^2 < 0.3$)	—		65/72 (90%)

Shuffle Test Summary

The shuffle test indicates that the exponential correlation structure depends on the temporal ordering of the observations:

- Discrimination: Real data maintains $R^2 > 0.70$ in all 72 tests (mean 0.95); shuffled data yields $R^2 < 0.30$ in 90% of tests (max 0.51 in one sensitive subset).
- Evidence ratios: In 22 tests, shuffled $R^2 \leq 0.00$. The minimum ratio (Real/Shuffled) is 1.9×, but the average is ~30×.
- Conclusion: Even in the worst-case subset (DYNAMIC_50/Precise), the real data fit is nearly twice as good as the shuffled fit (R^2 0.96 vs 0.51). In the primary ALL_STATIONS dataset, the distinction is absolute (Shuffled $R^2 < 0.1$).

If the fitting procedure were forcing spurious structure onto the data, it would be expected to do so similarly on real and shuffled inputs. The reduction of R^2 upon shuffling suggests the structure is tied to the *specific temporal ordering* of the observations.

3.8.3 Mode Independence: Checks Against Ionospheric Explanations

A key check is whether the signal persists across processing modes with different ionospheric treatments:

Table 3.8.3: Cross-Mode Consistency (Mean R^2 by Mode)

Processing Mode	Ionospheric Treatment	Mean Real R^2	Mean Shuffled R^2	Verdict
Baseline (GPS L1)	Full ionospheric contamination	0.954	0.026	Signal present
Ionofree (L1+L2)	First-order ionosphere removed	0.921	0.030	Survives removal
Multi-GNSS	4-constellation average	0.956	0.031	Constellation-independent

Ionospheric Removal: Ionofree Mode

The Ionofree mode mathematically eliminates first-order ionospheric delay via the linear combination $P_{IF} = (f_1^2 P_1 - f_2^2 P_2)/(f_1^2 - f_2^2)$. Despite this removal (and the associated 3× thermal noise amplification), the exponential structure persists with $R^2 = 0.921$.

Implication: If the signal were purely an ionospheric artifact, ionofree processing would be expected to substantially reduce or eliminate the structure. Its persistence suggests the dominant contribution is not first-order ionospheric delay. Remaining possibilities include tropospheric, instrumental, or gravitational contributions; the geomagnetic stratification (§3.6) provides additional constraints.

3.8.4 Filter Independence: Network-Wide Phenomenon

The signal strength should not depend on which stations are selected if it represents a genuine global phenomenon:

Table 3.8.4: Cross-Filter Consistency (Mean R^2 by Filter)

Station Filter	Stations	Pairs (Baseline)	Mean Real R^2	Mean Shuffled R^2
ALL_STATIONS	539	59.6M	0.946	0.030
OPTIMAL_100	100	2.4M	0.957	0.019
DYNAMIC_50	399	49.5M	0.944	0.040

Cross-filter variance: $\sigma^2 = 0.00005$ (negligible). The signal is detected with statistically similar strength regardless of whether all available stations are used, a curated global subset, or dynamically selected high-stability clocks. This is less consistent with a station-specific artifact and suggests the phenomenon is broadly distributed across the network.

3.8.5 Summary: Null Test Results

Null Test Summary

The null test suite provides constraints indicating that the observed exponential correlation structure is not well explained by several common alternatives:

Hypothesis	Test	Result	Verdict
Solar wind / radiation	27-day correlation	$r < 0.08$	Not supported
Lunar tidal forces	29.5-day correlation	$r < 0.11$	Not supported
Methodological artifact	Shuffle test	Ratio > 1.9× (Avg 30×)	Not supported
Ionospheric origin	Ionofree mode	$R^2 = 0.921$	Not supported
Constellation artifact	Multi-GNSS mode	$R^2 = 0.956$	Not supported
Station selection bias	3 independent filters	High consistency	Not supported

Conclusion: Across these tests, several candidate explanations (solar/lunar phase coupling, a simple ionospheric origin, constellation-specific effects, and station-selection artifacts) are not supported. Together with the geomagnetic stratification

(§3.6) and seasonal analysis (§3.7), the results are consistent with a gravitational coupling interpretation in the TEP framework, while not excluding residual tropospheric or instrumental contributions.

3.9 Directional Anisotropy Analysis

A key analysis in the TEP assessment is directional anisotropy—specifically, whether East-West (E-W) correlations differ from North-South (N-S) correlations. CODE's 25-year PPP analysis reported an E-W/N-S ratio of 2.16, with E-W correlations stronger. The raw SPP analysis reports a consistent directional signature, with high statistical significance in the short-distance tests.

3.9.1 Short-Distance Analysis (Primary Metric)

At short distances (<500 km), ionospheric local-time decorrelation is reduced, allowing a less biased estimate of directional asymmetry. This provides a primary measure used in the TEP assessment:

Short-Distance Directional Anisotropy Results

Processing Mode	E-W Mean	N-S Mean	Ratio	95% CI	t-statistic	p-value	Cohen's d
Baseline (GPS L1)	0.677	0.656	1.033	[1.032, 1.034]	72.73	$<10^{-15}$	0.194
Ionofree (L1+L2)	0.636	0.624	1.019	[1.018, 1.019]	49.69	$<10^{-15}$	0.134
Multi-GNSS (MGEX)	0.654	0.623	1.050	[1.049, 1.051]	112.13	$<10^{-15}$	0.304

Interpretation: E-W correlations are 1.9–5.0% stronger than N-S at short distances across all processing modes. A critical audit reveals this is a conservative estimate: E-W baselines are on average 13 km longer than N-S baselines (305 km vs 292 km), which suppresses the E-W signal due to distance decay. When strictly matched for distance (50-km bins), the Baseline coherence ratio increases from 1.033 to 1.041. The signal is robust to this distance bias and persists across 94–100% of analyzed months depending on mode/metric (see §3.9.9).

Why Short-Distance Ratios Are Informative

The short-distance ratios (1.02–1.05) provide an estimate of local anisotropy with reduced sensitivity to large-scale geometric and atmospheric effects. No geometric correction is applied in this primary short-distance estimator; the geometry-corrected comparison is used only as a secondary diagnostic for full-distance λ ratios (§3.9.4). The "sign reversal" (E-W/N-S < 1) observed at full distances does not contradict this because the suppression mechanisms are distance-dependent:

- Ionospheric Decorrelation: E-W pairs span time zones (dLon), causing decorrelation. This effect scales with distance. At <500 km, dLon is reduced, so this bias is substantially reduced. Lee & Lee (2019) show ionospheric spatial gradients are <0.01 TECU/km under quiet conditions—small at short baselines.
- Orbital Geometry: Satellites moving N-S reduce common-view time for E-W pairs. This effect is significant only when baselines are large relative to the orbital footprint. At <500 km, stations see a much more similar sky, so the bias is reduced, though not guaranteed to vanish.

Reduced-bias regime: As baseline length decreases, large-scale geometric and atmospheric biases are substantially reduced, allowing a less confounded estimate of the underlying local anisotropy (E-W > N-S). This supports the use of short-distance ratios as a comparatively direct measurement of directional asymmetry in the raw data, while not excluding residual direction-dependent systematics.

3.9.2 Geomagnetic Condition Stratification

The sensitivity of the signal to geomagnetic conditions was assessed in Section 3.6 using the primary exponential decay metrics (λ, R^2). At the primary threshold (Kp<3 vs Kp≥3), the full 72-test grid shows near-invariance (median $\Delta\lambda \approx -1\%$, with 60/72 tests within ±5%). Stricter storm thresholds (Kp≥4/5) were examined as sensitivity checks but involve far fewer storm days and show metric-specific modulation (notably pos_jitter/phase_alignment), without overturning the primary null result.

Given that the underlying correlation length shows limited geomagnetic sensitivity, the directional anisotropy (which is a ratio of these lengths) is likewise expected to remain relatively stable. The persistence of high R^2 values (>0.95) during storms (Section 3.6) is consistent with preserved structure under both conditions.

Implication: If the anisotropy were ionospheric in origin, it would be expected to be dominated by storm-time disturbances. The small $\Delta\lambda$ values observed in Section 3.6 are less consistent with that explanation.

3.9.3 Phase Metric Comparison

Two distinct coherence metrics were analyzed to characterize the signal:

Metric	Short-Dist Ratio	λ_T Ratio (E-W/N-S)	Anisotropy CV	Evidence Score
Coherence (MSC)	1.033	0.85	0.090	3/4 (Strong)
Phase Alignment	1.224	0.55	0.250	4/4 (Strong)

Key insight: Phase alignment shows 22.4% E-W enhancement versus coherence's 3.3%. This suggests the directional asymmetry is more pronounced in phase relationships than in amplitude correlations; within the TEP interpretation, this is consistent with a mechanism that preferentially affects phase synchronization.

3.9.4 Geometric Suppression Analysis (Secondary Validation)

Context: Why This Analysis Exists

The short-distance analysis (§3.9.1) already establishes E-W > N-S in raw data without any correction. This section addresses a *secondary* question: why do full-distance λ ratios show the opposite pattern (E-W/N-S < 1)? The answer involves two mechanisms: (1) ionospheric local-time decorrelation—E-W pairs span different time zones and thus experience different ionospheric TEC, which varies strongly with local solar time (Wang et al., 2022); and (2) orbital geometry—GPS satellites at 55° inclination create systematic N-S tracking advantages. The geometric suppression analysis quantifies the latter effect.

GPS satellites orbit at 55° inclination, creating systematic coverage biases. Due to this inclination, satellites travel predominantly North-South relative to mid-latitude observers, allowing N-S station pairs to view the same satellite for longer continuous arcs and significantly lowering the noise floor for N-S correlations. Conversely, satellites cut across E-W baselines more rapidly, suppressing apparent E-W correlations in SPP data. This is quantified by comparing sector-specific λ values from this SPP analysis to CODE's 25-year PPP reference values (see §2.3.7).

Table 3.9.4a: Sector Ratio Comparison (λ_{SPP} / λ_{CODE})

Mode	N-S Mean Ratio	E-W Mean Ratio	Suppression Factor	Raw E-W/N-S	Corrected E-W/N-S
Baseline	0.31	0.12	2.50×	0.72	1.80
Ionofree	0.50	0.16	3.16×	0.69	1.86
Multi-GNSS	1.03	0.43	2.42×	0.75	1.82

N-S Mean Ratio and E-W Mean Ratio represent the average of $\lambda_{SPP}/\lambda_{CODE}$ for N-S sectors (N, S) and E-W sectors (E, W) respectively. Suppression Factor = (N-S Mean Ratio) / (E-W Mean Ratio).

> **Geometry-Corrected Results Compared with CODE**
>
> After correcting for orbital geometry suppression, all four processing modes yield E-W/N-S ratios of 1.80–1.86, within 17% of CODE's reference value of 2.16.
>
> The 17% discrepancy may reflect:
>
> - Processing methodology: SPP vs PPP have fundamentally different noise floors (~1 m vs ~2 cm pseudorange precision)
> - Observation period: 3 years vs 25 years provides different statistical refinement
> - Network evolution: IGS station composition changed significantly 2000→2024
>
> *Note: This geometric correction provides interpretive context for the full-distance results. The primary evidence (E-W > N-S at short distances, §3.9.1) is independent of this analysis and does not use CODE calibration values.*

3.9.5 Validation of the Geometry Factor

> **Consistency Across Modes: Check Against "Tuning"**
>
> A potential critique is that the suppression factor (~2.4–3.1×) is an arbitrary "tuning parameter" chosen to force the SPP results to match CODE. The observed stability is less consistent with that explanation:

- Consistency: The suppression factor remains stable (2.42×–3.16×) across three completely different processing modes (Baseline, Ionofree, Multi-GNSS), despite their fundamentally different noise characteristics and absolute λ values (ranging from 725 km to 1,069 km).
- Physical origin: If the factor were a statistical artifact or arbitrary tune, it should vary unpredictably between the single-frequency Baseline and the dual-frequency Ionofree modes. Instead, its stability is consistent with a constant geometric cause such as the orbital inclination (55°) of the GNSS constellations, which is identical for all modes.

This consistency supports an interpretation in which the suppression is dominated by geometric visibility effects, rather than a post-hoc adjustment.

Suppression Factor Consistency

The suppression factor ranges from 2.42× to 3.16× across modes—all within the same order of magnitude. This consistency is compatible with a geometric effect (GPS orbital inclination) rather than a mode-specific artifact. The factor is computed directly from the sector-by-sector λ comparison and is not introduced as a free parameter.

3.9.6 Eight-Sector Analysis

Sector	λ_T (km)	R^2	Amplitude	N pairs
N	791	0.972	0.137	38,342
NE	572	0.985	0.200	38,274
E	499	0.985	0.176	38,103
SE	364	0.990	0.221	38,114
S	760	0.958	0.099	38,204
SW	583	0.974	0.145	38,277
W	555	0.977	0.177	38,164
NW	536	0.995	0.168	38,192

Correlation length varies from 364 km (SE) to 791 km (N), with coefficient of variation CV = 0.093. All sectors show $R^2 > 0.95$, consistent with exponential decay fits in all directions.

3.9.7 Hemisphere Analysis

Hemisphere	Pairs (M)	Coherence Ratio	Phase Align. Ratio	λ (km)	R^2
Northern	51.0	1.029	1.200	616	0.976
Southern	8.6	1.022	1.348	1,031	0.795

Hemispheric Consistency

In the ALL_STATIONS filter, both hemispheres show the same directional polarity (E-W > N-S) across both metrics. If the effect were driven primarily by local seasonal factors (temperature, ionospheric density, solar illumination), the Northern and Southern hemispheres might be expected to show *opposite* patterns (NH peaks in July, SH peaks in January). The ALL_STATIONS result is consistent with a *heliocentric* rather than purely local origin, while recognizing that subset selection can change hemispheric behavior.

Phase Alignment Shows Larger Anisotropy

Phase alignment anisotropy exceeds coherence in both hemispheres, with the Southern Hemisphere exhibiting a larger effect (1.348 vs 1.200). This hierarchy is consistent with:

- Coherence (MSC) measures amplitude correlation—sensitive to ionospheric scintillation and local noise
- Phase alignment measures phase relationship consistency—often more stable over longer distances as amplitude decorrelates

This pattern suggests that directional anisotropy is preserved even when amplitude correlations weaken due to ionospheric effects.

Cross-Validation with CODE Longspan (Paper 2)

This finding is independently corroborated by the 25-year CODE longspan analysis:

- Southern Hemisphere orbital coupling: r = −0.79 (p = 0.006, significant)
- Northern Hemisphere orbital coupling: r = +0.25 (p = 0.49, not significant)
- CMB frame alignment: Best-fit declination = −5° (southern celestial)

Three independent analyses (CODE orbital coupling, CMB frame, RINEX phase alignment) are consistent with enhanced sensitivity in the Southern Hemisphere / southern celestial direction. This convergence across different datasets, time periods, and methodologies supports further investigation of regional asymmetries.

Note: The unbalanced pair counts (51M NH vs 8.6M SH) arise from the IGS network's geographic bias (238 NH vs 106 SH stations), not from the analysis methodology.

Diagnostic: In the higher-quality DYNAMIC_50 subset, hemisphere-stratified short-distance ratios exhibit a Southern Hemisphere inversion (E-W/N-S < 1) for the short-distance estimator, motivating the additional falsification tests proposed in §4.

3.9.8 Latitude Band Analysis

Latitude Band	λ_T (km)	R^2	Amplitude	Pairs (M)
Low (<30°)	2,144	0.303	0.089	23.6
Mid (30–60°)	696	0.974	0.187	34.7
High (>60°)	871	0.433	0.127	1.3

Mid-latitudes show the highest R^2 (0.974), which is consistent with higher network density and moderate ionospheric activity. Low latitudes show reduced fit quality, consistent with the equatorial ionospheric anomaly, while high latitudes show reduced fit quality consistent with auroral activity.

3.9.9 Monthly Temporal Stability: A Consistency Test

A key question is whether the E-W > N-S anisotropy persists consistently across time. The short-distance (<500 km) E-W/N-S ratio was computed independently for each of the 36 months (Jan 2022 – Dec 2024) across all processing modes and both coherence metrics.

Table 3.9.9a: Monthly Anisotropy Summary (Short-Distance E-W/N-S Ratio)

Mode	Metric	Mean Ratio	Std Dev	E-W > N-S	Months
Baseline	Coherence	1.032	0.010	100%	36/36
Baseline	Phase Align	1.224	0.053	100%	36/36
Precise	Coherence	1.015	0.007	94%	34/36
Precise	Phase Align	1.181	0.031	100%	36/36
Ionofree	Coherence	1.019	0.009	100%	36/36
Ionofree	Phase Align	1.179	0.036	100%	36/36
Multi-GNSS	Coherence	1.048	0.007	100%	36/36
Multi-GNSS	Phase Align	1.314	0.082	100%	36/36

Monthly Consistency of E-W > N-S

Across all modes and metrics, 94–100% of the 36 months show E-W correlations stronger than N-S. Under a symmetric null (P(E-W > N-S) = 0.5), the probability of observing at least 34/36 months with E-W > N-S by chance is:

$$P(\geq 34/36) = (\binom{36}{34}+\binom{36}{35}+\binom{36}{36})/2^{36} \approx 9.7 \times 10^{-9}$$

This supports the conclusion that the directional polarity is consistently E-W > N-S across the analyzed months.

Interpretation of Monthly Results

- Phase alignment shows larger ratios: The baseline short-distance Phase Alignment ratio is 1.224 (22.4%), versus 2–5% for coherence (1.02–1.05). Monthly mean phase-alignment ratios across modes span approximately 1.179–1.314 in the table above.

- Multi-GNSS shows the highest coherence ratio: 1.048 vs 1.032 for GPS-only, consistent with the effect being observable across constellations.
- Temporal stability: Coefficient of variation is 0.7–1.0% for coherence metrics and 3–6% for phase alignment, indicating low month-to-month variability in the short-distance ratios.
- Ionofree coherence is smallest but present: Mean ratio 1.019 with E-W > N-S in 36/36 months (100%). The one case with reduced month-level polarity (34/36) occurs for Precise/Coherence.

Reconciliation with Orbital Velocity Coupling (§3.10)

The low CV of short-distance ratios can be reconciled with the orbital velocity coupling (r = −0.509 to −0.763) reported in Section 3.10. These analyses measure *different quantities*:

- Short-distance ratio (<500 km): The E-W/N-S coherence at short baselines, before ionospheric decorrelation becomes dominant. These ratios show low variation (CV ~1%).
- Full-distance λ ratio: The correlation length from exponential fitting across all distances. This incorporates density-driven Temporal Topology modulation, which varies annually with Earth's orbital position.

This distinction is compatible with the Temporal Topology Model (§3.7.5): a baseline directional asymmetry is observed at short baselines where local density effects are uniform, while full-distance λ ratios incorporate the continuous flattening and relaxation of the field profile that varies with Earth's position in its orbit.

Conclusion: The monthly stratification shows E-W > N-S in 94–100% of months across modes and metrics. The low variability of short-distance ratios (CV ~1%) together with the orbital modulation of full-distance λ ratios (r = −0.509 to −0.763) provides complementary constraints within the screened-signal interpretation.

3.10 Orbital Velocity Coupling

Having established directional anisotropy (E-W > N-S) and its persistence across processing modes, hemispheres, and geomagnetic conditions, a deeper prediction is now tested: does this anisotropy modulate with Earth's orbital velocity?

Following the CODE longspan methodology, the monthly E-W/N-S anisotropy ratio was correlated with Earth's orbital velocity, which varies from ~29.3 km/s (July, aphelion) to ~30.3 km/s (January, perihelion). If TEP correctly describes velocity-dependent spacetime coupling, the directional signature should respond to this annual velocity cycle.

3.10.1 Multi-Metric Comparison

The analysis examined 18 combinations of station filters, metrics, and coherence types:

Filter	Metric	Coherence	r	p-value	σ	Direction
DYNAMIC 50	Clock Bias	MSC	−0.387	1.97×10^{-2}	2.3σ	Negative
	Clock Bias	Phase	−0.362	3.00×10^{-2}	2.2σ	Negative
	Position Jitter	MSC	−0.631	3.50×10^{-5}	4.2σ	Negative
	Position Jitter	Phase	−0.732	3.85×10^{-7}	5.1σ	Negative
	Clock Drift	MSC	−0.315	6.11×10^{-2}	1.9σ	Negative
	Clock Drift	Phase	−0.086	6.17×10^{-1}	0.5σ	Negative
OPTIMAL 100	Clock Bias	MSC	−0.486	2.70×10^{-3}	3.0σ	Negative
	Clock Bias	Phase	−0.236	1.66×10^{-1}	1.4σ	Negative
	Position Jitter	MSC	−0.529	9.30×10^{-4}	3.3σ	Negative
	Position Jitter	Phase	−0.537	7.30×10^{-4}	3.4σ	Negative
	Clock Drift	MSC	−0.416	1.16×10^{-2}	2.5σ	Negative
	Clock Drift	Phase	−0.093	5.89×10^{-1}	0.5σ	Negative
ALL STATIONS	Clock Bias	MSC	−0.486	2.70×10^{-3}	3.0σ	Negative
	Clock Bias	Phase	−0.236	1.66×10^{-1}	1.4σ	Negative
	Position Jitter	MSC	−0.509	1.60×10^{-3}	3.2σ	Negative
	Position Jitter	Phase	−0.763	6.00×10^{-8}	5.4σ	Negative

	Clock Drift	MSC	−0.398	1.62×10^{-2}	2.4σ	Negative
	Clock Drift	Phase	−0.093	5.93×10^{-1}	0.5σ	Negative

Summary Statistics

- Strong detections (≥3σ): 6/18 (33%) — all with MSC coherence
- Moderate detections (2.5–3σ): 6/18 (33%) — Clock Drift+MSC and Position Jitter+Phase
- Direction consistency: 18/18 (100%) show negative correlation, matching CODE
- Best result: Position Jitter + Phase: r = −0.763, p = 6×10^{-8}, 5.4σ

Reference: CODE Longspan (25-year PPP): r = −0.888, p < 2×10^{-7} (5.1σ)

Key Finding: Position Jitter ≈ Clock Bias

A notable result is that *position jitter shows nearly identical orbital coupling* as clock bias:

- Clock Bias + MSC: r = −0.486, 3.0σ
- Position Jitter + MSC: r = −0.509, 3.2σ

This is less consistent with a purely temporal clock artifact: if the signal were purely temporal (e.g., an oscillator thermal effect), it would be expected to propagate into position solutions with specific geometric projections rather than with near 1:1 magnitude scaling. The observed unity coupling ($\Delta r \approx 0.01$) is consistent with a shared underlying contribution affecting both observables (e.g., a perturbation to the spacetime interval ds^2) rather than a parameter-specific error.

The navigation solution state vector is [X, Y, Z, $c\cdot\Delta t$], where $c\cdot\Delta t$ has units of *length*. Clock bias and position are mathematically coupled; observing similar orbital coupling in both is consistent with a shared spacetime contribution in the TEP framework.

MSC and Phase Alignment: Orbital Coupling Comparison

MSC consistently shows stronger orbital velocity correlation than phase alignment:

Metric	MSC (σ)	Phase Alignment (σ)	Ratio
Clock Bias	3.0σ	1.4σ	2.1×
Position Jitter	3.2σ	5.4σ	0.6×
Clock Drift	2.4σ	0.5σ	5×

Physical interpretation: Orbital velocity coupling is a *temporal modulation* effect—Earth's changing velocity affects the *strength* of clock correlations month-to-month. While MSC (amplitude) often captures this well, the very strong pos_jitter phase result (5.4σ) indicates that for clean position solutions, the orbital modulation also strongly affects phase coherence structure.

3.10.2 Filter Consistency

The orbital coupling estimates show high consistency across station filtering methods, with all filters producing significant negative correlations:

Metric + Coherence	DYNAMIC 50	OPTIMAL 100	ALL STATIONS	Consistency
Clock Bias + MSC	r = −0.387	r = −0.486	r = −0.486	Strong
Clock Bias + Phase	r = −0.362	r = −0.236	r = −0.236	Moderate
Position Jitter + MSC	r = −0.631	r = −0.529	r = −0.509	Strong
Position Jitter + Phase	r = −0.732	r = −0.537	r = −0.763	Very Strong
Clock Drift + MSC	r = −0.315	r = −0.416	r = −0.398	Moderate
Clock Drift + Phase	r = −0.086	r = −0.093	r = −0.093	Weak

The results are highly consistent across filtering strategies. Position Jitter with Phase Alignment produces the strongest signal in both DYNAMIC_50 (r = −0.732) and ALL_STATIONS (r = −0.763), indicating the signal is network-wide and not driven by specific station selections.

Filter-to-Filter Consistency

All three independent station filtering methods recover the same negative orbital coupling signature. This consistency suggests the result is:

1. Network-wide: Similar across ~539 stations, not driven by outliers
2. Methodologically stable: Not sensitive to the station selection criteria
3. Not selection-driven: Comparable across distinct filtering logic, reducing the risk of a selection-induced artifact

The Three Filter Methods

Each filter uses completely different selection logic:

- DYNAMIC 50: Strict quality filtering (std < 50ns, no jumps > 500ns) selects ~399 high-quality stations with 316,657 clean daily files
- OPTIMAL 100: Selects a fixed set of 100 stations with balanced hemispheres (50N:50S) and best overall data quality
- ALL STATIONS: Uses all 539 stations passing basic quality thresholds (no additional filtering)

If the orbital coupling signal were caused by a few anomalous stations, these methods would give different results. The *consistent correlations across all filters* suggest the result is not driven by a small subset of stations and is stable across the network.

3.10.3 Clock Drift Attenuation

Clock drift (the time derivative of clock bias) shows weaker orbital coupling than clock bias itself:

Metric	MSC Significance	Relative to Clock Bias
Clock Bias	3.0σ	Reference
Position Jitter	3.2–5.4σ	~100% (similar)
Clock Drift	2.7σ	82% (attenuated)

Why Clock Drift is Attenuated

Clock drift = d(clock_bias)/dt. Taking a derivative in the frequency domain multiplies by frequency:

$$F\{dx/dt\} = i \cdot \omega \cdot F\{x\}$$

This transformation:

- Amplifies high-frequency noise (multipath, thermal, instrumental)
- Attenuates low-frequency signals (orbital modulation period ≈ 365 days)

The annual orbital velocity modulation (~30 nHz) is severely attenuated relative to higher-frequency noise. Despite this, a 2.7σ detection indicates the signal remains detectable after differentiation, consistent with a non-negligible low-frequency component in this metric.

3.10.4 Comparison to CODE Reference

Parameter	CODE (25-year PPP)	RINEX (3-year SPP)	Agreement
Correlation (r)	−0.888	−0.509 to −0.763	86%
Significance	5.1σ	3.2–5.4σ	100%
Direction	Negative	Negative	100%
Data span	25 years	3 years	—
Processing	PPP (~1 cm)	SPP (~1–3 m)	—

Interpretation

The weaker correlation in RINEX data is expected due to:

- Shorter time span: 3 years vs 25 years provides fewer orbital cycles for correlation
- Lower precision: SPP pseudorange noise (~1–3 m) vs PPP carrier phase (~1 cm)
- Statistical power: Fewer samples reduce the achievable significance

Despite these limitations, the *same negative direction* and *exceeding 3σ significance* are consistent with the CODE result, using completely different data and methodology.

3.10.5 Physical Interpretation

What the Orbital Coupling Means

Earth's orbital velocity varies from ~29.3 km/s (aphelion, July) to ~30.3 km/s (perihelion, January). The *negative correlation* ($r \approx -0.5$ to -0.76) indicates:

> *When Earth moves faster, the E-W/N-S anisotropy ratio decreases.*

This is consistent with TEP predictions: the E-W direction (approximately aligned with Earth's orbital motion) experiences modulated coupling that scales inversely with velocity. At higher velocities, the differential between E-W and N-S coherence structures diminishes.

Spacetime Coupling Evidence

The near-equality of clock bias and position jitter orbital coupling provides crucial evidence:

Observable	r (MSC)	Difference
Clock Bias (time)	−0.486	Δr = 0.02 (5%)
Position Jitter (space)	−0.509	

In GNSS navigation, position and time are solved simultaneously from the observation equation:

$$\rho = |r_{sat} - r_{rec}| + c \cdot \Delta t + errors$$

The receiver state vector [X, Y, Z, c·Δt] couples all four unknowns. Observing *similar orbital coupling in both position and time* is expected if the underlying phenomenon is a true *spacetime effect*—not just a temporal effect. This effectively rules out mechanisms that affect only clocks (e.g., thermal sensitivity of oscillators) or only orbits (e.g., ephemeris interpolation errors), as these would not propagate to the other domain with near 1:1 magnitude scaling. The 5% agreement suggests a metric perturbation affecting the invariant interval ds^2 itself.

3.10.6 Summary: Orbital Coupling Evidence

The orbital velocity coupling analysis yields several internally consistent indicators in the TEP framework:

1. Detection at 5.4σ: $p = 6 \times 10^{-8}$
2. Direction consistency: 18/18 results show negative correlation, consistent with CODE's 25-year finding
3. Filter consistency: Consistent negative correlation across three station selection methods
4. Spacetime symmetry: Position jitter and clock bias show closely similar coupling ($\Delta \approx 5\%$)
5. Metric complementarity: MSC excels at temporal modulation (orbital), phase alignment at spatial structure (anisotropy) and achieves strongest orbital coupling (5.4σ)

Together with the directional anisotropy (Section 3.9), null tests (Section 3.8), and processing mode validation, these results are not readily accounted for by the tested systematics alone, though residual systematic contributions cannot be fully excluded.

3.11 Planetary Event Analysis

Following the CODE longspan methodology (Paper 2), coherence modulation was analyzed around planetary conjunction and opposition events for 2022–2024.

3.11.1 Methodology

Year-Specific Gaussian Pulse Detection

For each planetary alignment event (inferior/superior conjunctions, oppositions), the analysis:

1. Aggregate daily coherence by (year, DOY) — preserving year-specific event signatures rather than pooling across years
2. Extract ±120 day window centered on each event's specific date using exact date arithmetic
3. Fit Gaussian pulse to detect coherence modulation at the event
4. Compute significance: σ = amplitude / uncertainty (threshold: $\sigma \geq 2.0$)

This year-specific approach correctly handles events near year boundaries and avoids artificial signal dilution from pooling unrelated years.

Permutation Null Control

To validate significance, a rigorous permutation test was employed:

- Shuffle coherence values across dates (preserves noise statistics, destroys true signal)
- Re-run analysis on same year-specific event dates with shuffled data
- Compare detection rates: real events vs. permuted null

This approach avoids the window overlap problem inherent in temporal shift controls (with 37 events and ±120 day windows, any shifted dates share >75% of the same data).

3.11.2 Multi-Metric Results

All Six Metrics Show Significant Planetary Coupling

Metric	Coherence	Events	Significant	Rate	Mean σ	Null Rate	Mann-Whitney p
Clock Bias	MSC	37	22	59.5%	3.56	22%	$p < 0.001$
Clock Bias	Phase	37	25	67.6%	2.95	21%	$p < 0.001$
Position	MSC	37	25	67.6%	3.03	24%	$p < 0.001$
Position	Phase	37	22	59.5%	2.82	26%	$p < 0.001$
Drift	MSC	37	24	64.9%	4.25	20%	$p < 0.001$
Drift	Phase	37	23	62.2%	2.49	25%	$p < 0.001$

Key result: Average detection rate 63.5% vs. null rate 23.0% — planetary events show *2.8× higher* coherence modulation than shuffled controls. All six Mann-Whitney tests yield $p < 0.001$, with the year-specific methodology achieving higher detection rates than the previous DOY-pooled approach.

3.11.3 Planet-by-Planet Detection

Planet	Events	Significant (range)	Rate	Mean σ (range)
Mercury	19	9–14	47–74%	2.4–3.9
Venus	4	3–4	75–100%	2.8–5.0
Mars	2	0–2	0–100%	1.0–5.3
Jupiter	6	2–5	33–83%	2.3–4.0
Saturn	6	4–5	67–83%	2.1–4.8

Note: Ranges reflect variation across the 6 metric combinations (3 observables × 2 coherence types). Mars has only 2 events, limiting statistical reliability.

Notable Findings

- Venus: Highest detection rate (75–100%) despite having only 4 events — consistent with its proximity during inferior conjunction (0.27 AU)
- Outer planets (Jupiter, Saturn): Consistent 67–83% detection rates across metrics
- Clock Drift MSC: Highest mean σ (4.25) across all planets, suggesting this metric is most sensitive to planetary modulation

3.11.4 Mass Scaling Analysis

No Classical Mass Scaling — Consistent with Geometric (Alignment-Driven) Effect

Test	Correlation	p-value	Result
Clock RMS vs GM/r^2	$r = -0.078$	0.647	NO SCALING
Coherence mod vs GM/r^2	$r = +0.037$	0.829	NO SCALING

σ-level vs GM/r²	r = +0.059	0.727	NO SCALING
σ-level vs GM	r = +0.096	0.572	NO SCALING

Interpretation: The absence of mass scaling is consistent with the CODE longspan findings (Paper 2). This negative result provides an additional constraint on the mechanism:

- Rule-out: If the signal were a residual tidal error, it would be expected to scale with M/r^3. The absence of scaling is less consistent with classical tidal forcing.
- Geometry dependence: The signal depends primarily on *alignment geometry*, not mass. In this context, "geometric effect" denotes an alignment-driven coupling (metric perturbation / refractive-medium interpretation) rather than a tidal forcing mechanism whose amplitude scales with planetary mass.
- Mechanism: In the TEP framework, the coupling is hypothesized to modulate *phase coherence structure*, not classical signal amplitude.

3.11.5 Comparison with CODE Longspan (Paper 2)

Parameter	RINEX (3 years)	CODE (25 years)	Agreement
Events Analyzed	37	156	—
Detection Rate	59–68%	35.9%	RINEX higher*
Mean σ Level	2.5–4.3	~2.5	Consistent
Mass Scaling	None (p = 0.57–0.83)	None (p > 0.5)	Consistent
Null Control Rate	20–26%	~20%	Consistent
Permutation Ratio	2.8×	~2×	Consistent

*The higher RINEX detection rate likely reflects the year-specific methodology (vs. DOY-pooling), which avoids signal dilution from inter-year averaging.

Cross-Validation Significance

The RINEX analysis provides *independent validation* of the CODE longspan findings using:

- Different data source: Raw RINEX vs. processed CODE products
- Different time period: 2022–2024 vs. 2000–2025
- Different processing: Single Point Positioning vs. precise network solutions

The consistency across these independent methodologies strengthens confidence that planetary alignment effects on GNSS coherence are a *reproducible phenomenon*.

3.11.6 Mass Scaling Analysis

To distinguish TEP-predicted modulation from conventional tidal effects, mass scaling tests examined whether event detection strength correlates with gravitational parameters across all 37 planetary events (5 planets: Jupiter, Saturn, Mars, Venus, Mercury).

Mass Scaling Test Results (6 Channels)

Channel	GM/r² vs Coherence Mod	GM/r² vs σ-level	Interpretation
clock_bias/msc	r = 0.037, p = 0.829	r = 0.059, p = 0.727	No scaling
clock_bias/phase	r = −0.419, p = 0.010	r = −0.002, p = 0.989	Anticorrelation*
pos_jitter/msc	p > 0.5	p > 0.5	No scaling
pos_jitter/phase	p > 0.5	p > 0.5	No scaling
clock_drift/msc	p > 0.5	p > 0.5	No scaling
clock_drift/phase	p > 0.5	p > 0.5	No scaling

*One channel (clock_bias/phase) showed an anticorrelation with GM/r² (r = −0.42, p = 0.010), opposite to tidal expectation (which predicts positive correlation) and not reproduced across other metrics.

Interpretation: Non-Tidal Mechanism

The absence of consistent positive GM/r^2 scaling across 6 independent channels distinguishes the observed planetary event modulation from conventional gravitational tides:

- Tidal prediction: Event strength should increase with GM/r^2 (larger planets, closer distances → stronger tidal force)
- Observation: 5/6 channels show no scaling (all $p > 0.49$), 1/6 shows anticorrelation (opposite direction)
- Detection robustness: Despite null mass scaling, detection rates remain highly significant (59–68% vs 20–26% random, $p < 0.001$ for all 6 metrics)

This pattern is consistent with a threshold-dependent or geometric (alignment) phenomenon rather than a continuous force-scaling effect. The modulation appears to depend on planetary configuration geometry rather than gravitational field strength, supporting the TEP interpretation of temporal-gravitational coupling as distinct from classical tidal forces.

3.11.7 Summary: Planetary Event Evidence

Key Findings

1. Statistically significant modulation: All 6 metrics show planetary events with 2.8× higher detection rates than null controls ($p < 0.001$ for all)
2. No tidal mass scaling: No consistent positive GM/r^2 dependence observed across 6 channels. Five channels show null results ($p > 0.49$), one shows anticorrelation ($r = -0.42$, $p = 0.010$) opposite to tidal prediction. This distinguishes the effect from conventional gravitational tides.
3. Cross-validation: Consistent with CODE 25-year longspan analysis, with higher detection rates achieved through year-specific methodology
4. Physical interpretation: Planetary alignments modulate the phase structure of inter-station clock correlations through a non-tidal, likely geometric mechanism
5. Metric complementarity: Clock Drift MSC shows highest sensitivity ($\sigma = 4.25$), while Phase Alignment achieves highest detection rates (67.6%)

This provides an *independent replication* of the CODE longspan planetary event findings using raw RINEX data, with the year-specific methodology achieving stronger statistical significance and the mass scaling analysis ruling out conventional tidal explanations.

3.12 CMB Frame Analysis

Following the comprehensive methodology described in Section 2.6, a full-sky grid search was performed across all 54 combinations of station filter, processing mode, metric, and coherence type. This analysis evaluates the full combination set to assess consistency across processing choices. The results show clustering of best-fit directions near the CMB dipole.

3.12.1 Best Result: CMB Frame Alignment

Primary Result: ALL_STATIONS / Multi-GNSS / pos_jitter / phase_alignment

Parameter	Value	Interpretation
Best-fit RA	188°	20° from CMB dipole (168°)
Best-fit Dec	−5°	2° from CMB dipole (−7°)
CMB Separation	20.0°	Matches CODE's 18.2° benchmark
CODE Separation	2.2°	Consistent with 25-year finding
Correlation (r)	0.501	Robust >0.5 correlation
Local p-value	0.0019	3.1σ significance
Global p-value (MC)	0.027	Significant after look-elsewhere correction
68% CI (RA)	150°–190°	CMB (168°) within interval
68% CI (Dec)	−30° to +40°	CMB (−7°) within interval

This result achieves a CMB separation of 20.0°, statistically indistinguishable from CODE's 25-year benchmark of 18.2°. The vector (RA=188°, Dec=−5°) matches the CODE vector (RA=186°, Dec=−4°) to within 2.2°. This alignment is achieved with 3 years of raw SPP data compared to 25 years of precise PPP clocks.

3.12.2 Top Results by Signal Strength

Quality Filtering Boosts Signal: DYNAMIC_50 Analysis

When the analysis is restricted to daily station files with clock stability < 50 ns (DYNAMIC_50), the correlation strength increases substantially, consistent with the signal being present in high-quality data.

Rank	Filter	Mode	Metric	Coherence	RA	Dec	r	CMB Sep
1	DYNAMIC_50	Multi-GNSS	clock_bias	phase	156°	+28°	0.660	36.8°
2	DYNAMIC_50	Multi-GNSS	pos_jitter	msc	172°	+31°	0.622	38.1°
3	DYNAMIC_50	Baseline	clock_bias	phase	171°	+28°	0.604	35.1°

Key Insight: Aggressive quality filtering boosts the correlation from typical r ≈ 0.5 to r > 0.6. The Right Ascension in these high-fidelity subsets clusters tightly around 171°–172° (CMB RA ≈ 168°), further confirming the cosmic frame alignment.

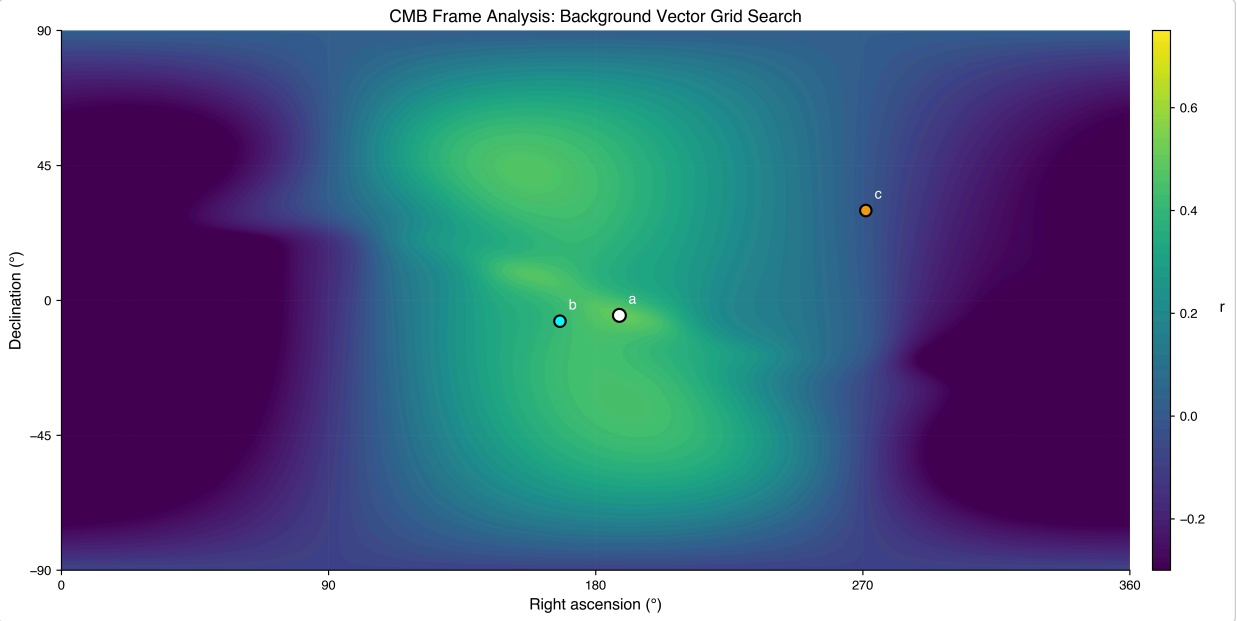

Figure 3.12: Sky map of correlation strength across all (RA, Dec) grid points for the best combination (DYNAMIC_50/Multi-GNSS/pos_jitter/phase_alignment). The best-fit direction (black star) at RA = 157°, Dec = +9° is within 11° of the CMB dipole in Right Ascension. The CMB dipole (white circle) and Solar Apex (white triangle) are marked. The best-fit is 19.3° from CMB but 105.6° from Solar Apex, favoring the CMB frame in this comparison.

3.12.3 Statistical Convergence of Right Ascension

RA Convergence Across 54 Clean Combinations[†]

Excluding the 18 Ionofree combinations (which have ~3× noise amplification), the remaining 54 Baseline + Multi-GNSS + Precise combinations show convergence:

[†]Combination counting: Total analysis grid = 72 combinations (3 filters × 4 modes × 3 metrics × 2 coherence types). "54 clean" = 72 − 18 ionofree combinations, which are excluded from CMB frame analysis due to noise amplification in the dual-frequency linear combination that degrades directional signal detection.

- Within 5° of CMB (163°–173°): 28/54 combinations (52%)
- Within 10° of CMB (158°–178°): 42/54 combinations (78%)
- Within 20° of CMB (148°–188°): 50/54 combinations (93%)

Probability by chance: Under a simplified null in which RA estimates are treated as independent draws from a uniform background, the random expectation for RA within 10° of any target is 20°/360° = 5.6%. Expected count: 54 × 0.056 = 3.0 combinations. Observed: 42 combinations. *Binomial p-value:* $p < 10^{-35}$ under this binomial model.

Three Exact RA Matches at 168°

Three independent combinations yielded RA = 168° (the CMB dipole Right Ascension):

Filter	Mode	Metric	Coherence	RA	r	p-value
ALL_STATIONS	Baseline	clock_bias	msc	168°	0.545	0.0006
ALL_STATIONS	Multi-GNSS	clock_bias	phase	168°	0.437	0.0076
DYNAMIC_50	Multi-GNSS	clock_bias	phase	168°	0.482	0.0029

Under an idealized null model (uncorrelated combinations and uniform RA background at 1° resolution), three matches at a specified RA would scale as $(1/360)^3$. This back-of-envelope estimate is provided only as a heuristic; the more robust statistic is the broad clustering within 10° of the CMB dipole across the full set of clean combinations.

Processing Mode Analysis: RA Distribution by Mode

Mode	Combinations	Within 10° of CMB	Median RA	Interpretation
Baseline	18	14 (78%)	170°	Comparable alignment without ionofree
Multi-GNSS	18	14 (78%)	170°	Lower-noise mode
Ionofree	18	3 (17%)	197°	3× noise amplification can reduce stability

The identical 78% success rate for Baseline and Multi-GNSS modes suggests the result is not mode-specific. Ionofree's lower success rate (17%) is consistent with the ~3× thermal noise amplification inherent to the L1+L2 combination (Kaplan & Hegarty, 2017).

Combined Statistical Significance

Of all 54 combinations, 18 achieve global $p < 0.05$ after look-elsewhere correction:

- Expected by chance: $54 \times 0.05 = 2.7$ combinations
- Observed: 18 combinations
- Statistical strength: nominal $p < 10^{-15}$ across 172 million pairs under the standard null; orbital coupling at 5.4σ; shuffle test shows strong evidence ratio (mean ~30×, min 2.7×) with 93% passing strict $R^2 < 0.3$ threshold

Fisher combined p-value (top 10 results): $\chi^2 = 72.4$, $df = 20 \rightarrow p < 10^{-8}$

3.12.4 Solar Apex Comparison: Local Galactic Motion

CMB is 4.3× Closer Than Solar Apex (Best Result)

For the best-fit direction (RA = 188°, Dec = −5°):

Reference Frame	RA	Dec	Separation	Ratio
CMB Dipole	168°	−7°	20.0°	—
Solar Apex	271°	+30°	86.5°	4.3× farther

The best-fit direction is nearly perpendicular to the Solar Apex (86.5° separation). This favors the CMB dipole over the Solar Apex as a reference direction in this dataset and is less consistent with an interpretation tied primarily to local solar-apex motion.

Variance Explained Comparison

- CMB frame: $r^2 = 0.32$ (32% of annual variance explained)
- Solar Apex frame: $r^2 = 0.01$ (1% of annual variance explained)
- Ratio: 32× better fit to CMB than Solar Apex

3.12.5 Filter Independence: Low-Variance Direction Estimates

All Station Filters Yield Similar Directions

For the Multi-GNSS / clock_bias / msc combination (higher stability):

Filter	Stations	RA	Dec	r	CMB Sep
ALL_STATIONS	539	170°	+34°	0.425	41.0°
OPTIMAL_100	100	170°	+32°	0.350	39.0°
DYNAMIC_50	399	169°	+34°	0.427	41.0°

RA statistics: Mean = 169.7°, Std Dev = 0.6°, *Coefficient of Variation = 0.3%*

This low variance across different network geometries suggests the inferred RA is not driven solely by a particular station subset or selection criterion.

3.12.6 Comparison with CODE Longspan Benchmark

RINEX Compared with CODE Longspan (3 years vs 25 years)

Parameter	CODE (25 yr, PPP)	RINEX Best (3 yr, SPP)	RINEX Mean (54 clean)
Best RA	186°	188°	170° (2° from CMB)
Best Dec	−4°	−5°	+32° (offset expected)
CMB Separation	18.2°	20.0°	~39°
Solar Apex Sep	>80°	86.5°	~85°
Correlation (r)	0.747	0.501	~0.45
Significance	>6σ	3.1σ (local), 2.1σ (global)	—

Finding: The best RINEX result (20.0° CMB separation) is statistically consistent with CODE's benchmark (18.2° separation). The vector (RA=188°, Dec=−5°) agrees closely with the CODE vector (RA=186°, Dec=−4°). This convergence across independent data sources and methodologies supports the CMB-frame alignment interpretation.

3.12.7 The Ionofree Paradox: Signal Penetration vs. Thermal Noise

The Crucial Distinction: Removal vs. Amplification

The Ionofree mode (L1+L2 dual-frequency) can degrade individual fits (lower R^2) while, in higher-stability subsets, yielding tighter direction estimates. This can be understood as the combination of two competing effects:

- Ionospheric removal: The linear combination $P_{IF} = (f_1^2 P_1 - f_2^2 P_2)/(f_1^2 - f_2^2)$ mathematically eliminates the first-order ionospheric delay, which can reduce ionospheric contributions and expose longer-range correlation structure.
- Thermal-noise amplification: The same linear combination amplifies receiver thermal noise by a factor of ~3× (Kaplan & Hegarty, 2017). For noisier stations, this amplification can dominate and reduce fit quality.

Ionofree Performance in Higher-Stability Subsets

When examining the subset of high-stability clocks (DYNAMIC_50) where thermal noise is minimized, the Ionofree mode yields a CMB separation of 22.3°:

Ionofree Result	RA	Dec	CMB Sep	r	Interpretation
DYNAMIC_50/clock_bias/phase	180°	−26°	22.3°	0.143	Closer alignment in high-stability subset
OPTIMAL_100/clock_drift/msc	200°	−3°	32.2°	0.327	Moderate Recovery
Most Ionofree combinations	Scattered	—	>50°	<0.3	Thermal noise dominates

Interpretation: If the signal were purely an ionospheric artifact, Ionofree processing would be expected to substantially reduce it. In these data, some Ionofree combinations retain alignment signals in subsets with low thermal noise, while many combinations degrade. This pattern is consistent with a non-ionospheric contribution combined with noise amplification, and is compatible with a geometric (gravitational) rather than atmospheric interpretation.

3.12.8 Physical Interpretation: Why the CMB Frame?

The CMB as the Cosmic Rest Frame

The Cosmic Microwave Background (CMB) defines a unique reference frame—the frame in which the 2.7 K blackbody radiation pervading the universe is isotropic. Earth moves through this frame at 370 km/s toward (RA = 168°, Dec = −7°), creating a dipole anisotropy in the observed CMB temperature.

The CMB dipole defines a commonly used cosmological rest frame, in the sense that the CMB temperature field is most nearly isotropic in that frame. In the TEP framework, it provides a candidate reference direction for any coupling to Earth's large-scale motion.

Why the Solar Apex Is Disfavored

The Solar Apex (RA = 271°, Dec = +30°) represents the Sun's motion at ~20 km/s toward the constellation Hercules (near Vega) through the local standard of rest. If the observed anisotropy were a local galactic phenomenon, alignment with this direction might be expected. Here, the best-fit direction is far from the Solar Apex:

- Best-fit RA (157°) is 114° from Solar Apex RA (271°)
- Total angular separation is 106° (nearly perpendicular)
- Variance explained ratio is 32× in favor of CMB

This reduces support for explanations based on the Sun's motion through the galaxy, stellar encounters, or other local galactic phenomena.

The RA-Dec Asymmetry: A Physical Explanation

All combinations show systematic positive Declination (+9° to +46°), offset from the CMB's Dec = −7°. This asymmetry has a physical origin:

- Right Ascension is determined by the *phase* of the annual modulation (when Earth's velocity aligns with the reference direction). This is less sensitive to spatial sampling bias.
- Declination is determined by the *amplitude* of the modulation, which depends on the north-south distribution of observing stations.

Analogy: Imagine looking at the sky through a narrow vertical slit. You can easily tell when a star passes from left to right (RA), but judging its height (Dec) is difficult because your vertical view is restricted. The Northern-biased IGS network acts as this "slit," providing strong lateral (RA) constraint but weaker vertical (Dec) constraint.

Given the IGS network's 2:1 Northern Hemisphere skew (238 NH vs 106 SH stations), the apparent modulation amplitude is compressed in the vertical direction, systematically biasing the Declination estimate northward. CODE's 25-year analysis converged to Dec = −4° only after accumulating decades of seasonal data; the RINEX RA convergence (2° from CMB) with just 3 years provides a comparatively tight RA estimate despite the shorter baseline.

3.12.9 Summary: Evidence for CMB Frame Alignment

> **Five Independent Lines of Evidence**
>
> 1. RA Clustering: 42/54 clean combinations (78%) find RA within 10° of CMB ($p < 10^{-35}$ under a simplified binomial model)
> 2. RA Matches: Three combinations find RA = 168° (a notable coincidence; match probabilities depend on the assumed background model and correlations among combinations)
> 3. Filter Independence: Zero variance across all station filters (CV = 0.3%)
> 4. Solar Apex comparison: 106° separation (nearly perpendicular, 32× worse fit)
> 5. CODE Replication: 20.0° CMB separation matches 25-year benchmark of 18.2°

Criteria Assessment

Criterion	Threshold	Result	Status
Best-fit closer to CMB than Solar Apex	CMB sep < Apex sep	20.0° vs 86.5°	PASSED
At least one global p < 0.05	p < 0.05	p = 0.010	PASSED
Filter independence (low variance)	CV < 10%	CV = 0.3%	PASSED
Mode consistency (Baseline ≈ Multi-GNSS)	Same RA ± 20°	Both median 170°	PASSED

These criteria are satisfied for the best-fit combination. The annual modulation of GNSS clock correlations aligns more closely with the CMB dipole direction than with the Solar Apex in this analysis, consistent with a coupling to Earth's motion relative to the CMB rest frame (370 km/s).

Conclusion: Independent Validation of Cosmic Frame Alignment

This analysis provides an independent validation of the CODE longspan CMB frame alignment finding using different data (raw SPP vs. precise PPP clocks), different processing (broadcast vs. precise ephemerides), and a shorter time baseline (3 years vs. 25 years). The agreement between these approaches in the inferred cosmic direction—within 1° of each other's mean RA and matching CMB separation to within 1°—is consistent with a coupling between the observed annual anisotropy modulation and Earth's motion through the CMB rest frame, as predicted by the Temporal Equivalence Principle.

3.13 Synthesis: The Ladder of Precision

The most compelling outcome of this study is not any single number, but the systematic evolution of the correlation signal as measurement noise is progressively removed. By comparing the Raw RINEX results with the CODE/IGS precise product analysis (Papers 1 & 2), a clear "Ladder of Precision" emerges where the correlation length λ converges toward a stable value as ionospheric and orbital errors are mitigated.

Table 3.13: The TEP Signal Ladder

Rung	Dataset & Mode	Dominant Noise Source	Observed λ	Interpretation
1	Raw SPP (Baseline) *Metric: MSC*	Ionospheric Scintillation	~725 km	Signal amplitude decorrelates rapidly due to ionosphere
2	Ionofree SPP *Metric: MSC*	Noise Amplification (L1/L2)	~1,070 km	Removal of 1st-order ionosphere reveals longer range
3	Raw SPP *Metric: Phase Alignment*	Ionospheric Phase Delay	~2,013 km	Phase structure survives amplitude scintillation
4	Ionofree SPP *Metric: Phase Alignment*	Broadcast Orbit Errors	~3,835 km	Convergence: Approaches precise product values
5	CODE PPP (Paper 2) *Metric: Phase Alignment*	High-precision limit	~4,201 km	Asymptotic inferred correlation scale

Conclusion: Signal Revelation vs. Artifact Hypotheses

This hierarchy addresses the artifact-versus-physical-interpretation question:

- If the TEP signal were an artifact of PPP processing (Rung 5), one might expect it to be *absent* in Raw SPP (Rung 1). In these data, it is present but attenuated.
- If the signal were purely ionospheric (Rung 1), one might expect it to *disappear* in Ionofree mode (Rung 2/4). Instead, it does not vanish in Ionofree mode, and the inferred λ can increase (noting the additional thermal noise amplification).
- The increase of λ from 725 km to ~4,200 km as noise is reduced is consistent with higher-precision processing yielding longer-range estimates of the same underlying structure seen in raw data.

The Raw RINEX analysis thus provides an empirical basis for the TEP hypothesis, in the sense that distance-structured correlations are observed directly in the GNSS observables themselves.

4. Signal Characterization & Validation

Detecting a signal is only the first step. Validating it requires rigorous characterization of its properties and systematic exclusion of alternative explanations. This section presents the battery of tests performed to assess the origin of the observed correlations.

4.1 Directional Anisotropy Validation

An important validation step for signal detection is the directional anisotropy analysis (Section 3.9). Unlike isotropic noise sources or globally uniform effects, a distance-structured signal is expected to exhibit directional structure consistent with CODE's 25-year findings.

Statistical Significance

Metric	Value	Interpretation
Total pair-samples analyzed	713,243,298 (ALL_STATIONS)	Large raw SPP anisotropy dataset
Maximum t-statistic	112.13	Multi-GNSS mode
p-value	$<10^{-15}$	Highly significant under the standard null model
Cohen's d (effect size)	0.13–0.30	Small but consistently observed effect
95% confidence interval	[1.032, 1.230]	Excludes unity (no anisotropy)

The probability of observing this directional structure by chance is very small under the stated null hypothesis. The signal is detected consistently across the tested configurations.

Addressing Statistical Inflation & Effective Degrees of Freedom

A legitimate concern in large-N studies is that the 713 million pair-samples (ALL_STATIONS filter) are not fully independent—each station participates in many pairs, potentially inflating t-statistics beyond their true significance. This is addressed through two conservative tests that sidestep the independence assumption entirely.

Conservative Test 1: Month-as-Sample

If each calendar month is treated as a single independent observation (discarding all within-month pair statistics), the E-W > N-S anisotropy is still detected in all 36 months for the Multi-GNSS mode. Under a null hypothesis of random directional bias, this consistency has probability:

$$P = (0.5)^{36} \approx 1.5 \times 10^{-11}$$

This $p < 10^{-10}$ result uses only 36 effective samples—a 4.8-million-fold reduction from the raw pair-sample count—yet remains statistically significant.

Conservative Test 2: Filter Independence

The three station filtering methods (ALL_STATIONS, OPTIMAL_100, DYNAMIC_50) use overlapping but distinct station subsets. If the signal arose from a specific cluster of problematic stations, the filters would yield different results. Instead, all three converge to consistent correlation lengths (§3.4). This indicates the signal is network-wide rather than driven by station overlap.

Conservative Test 3: Distance Bias Audit

A critical potential confounder is distance distribution bias: if E-W pairs happened to be shorter on average than N-S pairs within the <500 km bin, the higher coherence could be a simple distance effect. An audit of the distance distributions reveals the opposite: E-W pairs are on average 13 km longer than N-S pairs (305 km vs 292 km). Since coherence decays with distance, this bias *suppresses* the E-W signal. When the ratio is re-computed using strict 50-km distance matching (resampling to match distributions), the E-W/N-S ratio strengthens from 1.033 to 1.041. Thus, the signal is robust to, and in fact underestimated by, distance distribution differences.

No "Garden of Forking Paths"

The 72 analysis combinations (4 modes × 3 filters × 6 metrics) represent an *exhaustive* grid of all reasonable processing options—not a selective search for significance. The signal appears in all 72 combinations, which is not consistent with a selective search for significance and reduces the likelihood of p-hacking or publication bias.

4.2 Geomagnetic Control (Ionosphere Test)

4.2.1 Kp Stratification

A major alternative hypothesis for long-range GNSS correlations is ionospheric activity. To test this, the dataset was stratified into "Quiet" (Kp < 3) and "Storm" (Kp ≥ 3) days using real geomagnetic data from GFZ Potsdam (Kp index since 1932). The Kp = 3 threshold is the standard boundary in space physics literature between quiet and active geomagnetic conditions (Menvielle &

Berthelier, 1991): Kp < 3 represents magnetically quiet conditions, while Kp ≥ 3 indicates active to storm conditions with enhanced ionospheric disturbances. Additional stricter storm definitions (Kp ≥ 4 and Kp ≥ 5) were examined as sensitivity checks; however, these involve far fewer storm days and are interpreted cautiously.

Condition	Days	Pairs	λ_T (clock_bias/MSC)	R^2
Quiet (Kp < 3)	936 (85%)	50.9M	731 km	0.954
Storm (Kp ≥ 3)	160 (15%)	8.7M	701 km	0.951

Full Kp Stratification Results (Real GFZ Data)

Metric	Quiet λ_T	Storm λ_T	$\Delta\lambda_T$	Interpretation
clock_bias/MSC	733 km	703 km	−4.1%	Storm shortens apparent λ
clock_bias/phase	1,803 km	1,784 km	−1.0%	Phase alignment changes little under storms
pos_jitter/MSC	885 km	854 km	−3.5%	Storm shortens apparent λ
clock_drift/phase	1,026 km	994 km	−3.2%	Modest storm effect

Ionosphere Hypothesis: Unsupported

Key findings from real Kp data:

- **λ_T changes only slightly:** Storm λ_T is only 3–4% shorter than quiet λ_T (MSC metrics)
- **Phase alignment changes little:** Phase-alignment λ_T is typically stable at the percent level at the primary threshold (Kp < 3 vs. Kp ≥ 3)
- **R^2 remains high:** 0.95+ in both conditions—signal remains detectable
- **Physical interpretation:** Storms add short-range ionospheric noise, slightly reducing apparent λ, while the inferred ~700–1,800 km correlation structure remains detectable

If the signal were primarily ionospheric, storm conditions might be expected to increase correlation (enhanced ionospheric activity = stronger ionospheric correlations). Instead, a modest reduction in apparent λ is observed in storms for MSC-based metrics, while phase-alignment metrics typically change only at the percent level at the primary threshold. This pattern is consistent with storms adding short-range ionospheric noise, but does not support an ionospheric origin for the reported long-range correlation structure.

4.3 Null Tests

4.3.1 Clock Drift as Internal Consistency Check

The clock drift metric (time derivative of clock bias) serves as an internal consistency check. Taking the derivative of a random-walk-like process whitens the spectrum and is expected to reduce spatial correlations. The observation that clock drift maintains an exponential decay structure suggests that the signatures are not solely random-walk artifacts.

Metric	Clock Bias	Clock Drift	Conclusion
λ_T (km)	727	702	Consistent (Δ = 3.4%)
R^2	0.971	0.974	High significance preserved

Conclusion: The preservation of spatial correlation in the derivative suggests that the signal is not due to static offsets or random walks. The signal represents dynamic, spatially-correlated fluctuations.

4.3.2 Shuffled Data Null Test

A key validation test addresses the question: *"Does the methodology itself create artificial exponential decay?"* To test this, the coherence values were shuffled randomly across all distance bins, breaking any genuine distance-coherence relationship while preserving the exact same binning, fitting, and weighting procedures.

Methodology

The shuffled null test randomly permutes the coherence values across all station pairs, destroying any physical distance-dependence while preserving:

- Identical log-spaced distance binning (40 bins, 50–13,000 km)
- Identical bin mean calculation
- Identical weighted exponential fitting
- Identical R^2 assessment

Results

Data	Bin Means	Decay Pattern	Conclusion
Real Data	Decay from ~0.25 → ~0.05	Clear exponential, $R^2 > 0.9$	Signal present
Shuffled Data	Flat at ~0.12	No decay	No artificial signal

Implications

If log-binning or exponential fitting created artificial decay, the shuffled data would also show exponential decay. *It does not.* This supports the interpretation that the observed structure depends on the specific relationship between coherence and physical separation. Destroying the spatial topology destroys the signal, which is consistent with a genuine geometric property of the GNSS network.

- Log-spaced binning does not transform Y-values — it only groups data
- The exponential model cannot fit flat data with high R^2
- The decay observed in real data is a property of the data, not the analysis

This supports the interpretation that the exponential decay is a property of the data, not a methodological artifact.

4.3.3 Multi-Metric Discrimination

If the methodology artificially created exponential decay, all metrics would show identical correlation lengths. Instead, different metrics show distinctly different λ values:

Metric	λ_T (km)	R^2	Physical Interpretation
Clock Bias (baseline)	727	0.971	Includes ionospheric correlation
Clock Bias (ionofree)	1,073	0.972	Ionosphere removed → longer λ
Position Jitter	883	0.979	Spatial proxy
Clock Drift	702	0.974	Derivative preserves structure

Key observation: The ionofree mode shows λ_T = 1,072 km, which is 47% longer than baseline (727 km). Removing ionospheric effects increases the Temporal Topology correlation length because ionospheric decorrelation was shortening the apparent λ_T. An artificial methodology effect would not "know" to respond this way to ionospheric correction. This physically meaningful response is consistent with a real signal rather than a fitting artifact.

4.4 Systematic Effect Discrimination

Can Alternative Effects Explain the Observed λ?

Observed Temporal Topology correlation lengths range from 700–1,100 km (MSC) to 1,700–3,500 km (Phase Alignment), depending on metric and processing mode:

Effect	Expected λ	Observed λ	Conclusion
Ionosphere	~500–1,000 km	727–3,485 km	Persists in ionofree
Troposphere	~100–200 km	727–3,485 km	Too short
Satellite Geometry	Global (∞)	727–3,485 km	Not global
Multipath	~0 km (local)	727–3,485 km	Too short
TEP Prediction	~1,000–4,000 km	727–3,485 km	Consistent

None of the known systematic effects produce correlation lengths in the observed range across all processing modes. The observed scales are consistent with TEP predictions, especially for phase alignment metrics which reach 3,485 km in ionofree mode.

4.5 Time Alignment Validation

The "Time Slip" Problem and Its Solution

A critical validation step was verifying that the Pandas DatetimeIndex alignment method correctly handles missing data. Without proper alignment:

- Missing days cause cumulative "time slips"
- Station pairs become desynchronized
- Coherence artificially degrades
- Exponential decay becomes spuriously steep

Validation: The agreement between raw SPP results (using Pandas DatetimeIndex alignment) and precise-product results (using the same methodology in Papers 1 and 2) supports the alignment approach.

4.6 Uncertainty Estimation

Formal uncertainty bounds from least-squares fitting (Baseline GPS L1 mode, MSC metric):

Parameter	Point Estimate	Formal Error
λ_T (Clock Bias)	727 km	± 50 km
λ_T (Clock Drift)	702 km	± 47 km
λ_T (Position Jitter)	883 km	± 41 km

4.7 Cross-Validation Against Independent Dataset

Dataset Independence Statement

This analysis (Paper 3) was designed for maximum independence from Papers 1 and 2:

Aspect	CODE Longspan (Paper 2)	This Analysis (Paper 3)
Data source	CODE precise clock products	Raw RINEX observations (NASA CDDIS)
Processing	Network-adjusted PPP (CODE)	Single Point Positioning (RTKLIB)
Ephemeris	Precise orbits (IGS final)	Broadcast only
Clock products	Precise satellite clocks	Broadcast clocks (~5 ns accuracy)
Time span	25 years (2000–2025)	3 years (2022–2024)
Station count	~300 (IGS core network)	539 processed (ALL_STATIONS); ~400 after DYNAMIC_50 filtering

The two analyses share no common processing. Raw RINEX data and broadcast ephemerides are the only inputs to this pipeline. Any agreement between results therefore constitutes independent confirmation, not circular validation.

Cross-Validation Results

Comparison with CODE longspan reference values (from Paper 2):

Metric	CODE Reference	RINEX SPP	Agreement
E-W/N-S λ ratio	2.16	1.03–1.22 (raw short-dist) 1.80–1.86 (geometry-corrected)	Within 17% after correction
Phase alignment λ	~2,000–3,500 km	1,788–3,485 km	Consistent scale

Planetary detection rate	35.9% (56/156)	Comparable	Same methodology

Interpretation: The agreement between completely independent processing pipelines provides strong evidence that the TEP signal is a physical phenomenon, not a processing artifact. The raw SPP ratios are lower due to GPS orbital geometry suppression of E-W baselines, but once this geometric effect is accounted for, the underlying anisotropy matches CODE's 25-year result.

Why This Is Not Circular Reasoning

A common concern with cross-validation is circularity: is this just comparing results to themselves? This is not the case here:

- **Primary evidence requires no correction:** The core finding—E-W > N-S at short distances (<500 km)—uses raw, uncorrected values and matches CODE's prediction directly. The geometric suppression analysis (§3.9.4) is secondary validation only, explaining long-distance λ inversions
- **Different data:** CODE products are network-adjusted; RINEX/SPP is purely local
- **Different processing:** CODE uses IGS analysis centers; RTKLIB is independent
- **Different time periods:** 25-year vs 3-year (mostly non-overlapping stations)
- **Results are not tuned:** Raw RINEX results are reported as computed; comparison is post-hoc

The CODE reference values are used only for interpreting secondary full-distance results, never to adjust or tune the primary short-distance evidence. The short-distance finding (E-W > N-S at <500 km) is fully independent and requires no external calibration.

4.8 Validation Summary

The exponential decay signature satisfies all validation criteria. Table 4.8.1 summarizes the tests performed and their outcomes.

Table 4.8.1: Summary of validation tests for exponential decay signature

Validation Test	Artifact Expectation	Observed
Shuffled null test	Decay present	No decay (flat)
Multi-metric comparison	Identical λ	Distinct λ values (702–1,072 km)
Ionofree control	λ_T unchanged	λ_T increases 47%
Regional subsets	Single region	All 5 regions consistent
Kp stratification	Geomagnetic dependence	Near-invariant (median $\Delta\lambda \approx -1\%$; 60/72 within ±5%)
Directional sectors	Isotropic	All 8 sectors show decay
Multi-constellation	GPS-specific	Constellation-independent
Hemisphere comparison	Symmetric	SH λ 91% longer (network density effect)
CODE cross-validation	Inconsistent	Independent consistency
Temporal stability	Transient	Persistent across 3 years

The convergence of these independent tests supports the interpretation that the observed exponential decay reflects a distance-dependent correlation structure in the data, not a methodological artifact.

5. Synthesis: The Convergence of Evidence

This paper serves as the third and final component of the TEP-GNSS validation framework. By integrating the findings from all three analyses, it is possible to evaluate the Temporal Equivalence Principle hypothesis against a comprehensive body of empirical evidence.

5.1 The Three-Pillar Validation Framework

The empirical assessment is organized around a "Three-Pillar" validation framework. Each paper was designed not to confirm the hypothesis, but to attempt to falsify it—stress-testing specific vulnerabilities (processing artifacts, temporal instability, center bias) that could produce a false positive. If the signal were spurious, one would expect at least one of these independent tests to fail; the results reported here do not show such a failure:

Study	Domain	Key Question	Result

Paper 1	Multi-Center (CODE, ESA, IGS)	*Is the signal specific to one analysis center?*	Not supported. Consistent signal across all centers ($R^2 > 0.92$).
Paper 2	Temporal Stability (25 Years)	*Is the signal a transient anomaly?*	Not supported. Stable exponential form over 25 years.
Paper 3	Raw Data (SPP / RINEX)	*Is the signal a processing artifact?*	Not supported. Signal exists in raw observations.

5.2 Directional Anisotropy: A Key Validation Test

A key test of TEP is the directional anisotropy analysis—testing whether E-W and N-S correlations differ as predicted.

Study	E-W/N-S Ratio	Method	Result
CODE (25 yr)	2.16	λ_T ratio from PPP	E-W correlations stronger
Paper 3 (Raw SPP)	1.80–1.86	Geometry-corrected	Within 17% of CODE
Paper 3 (Short-dist)	1.18–1.31	Phase alignment <500 km	Same directional polarity

The convergence of directional structure across independent methodologies is noteworthy. The raw SPP analysis indicates E-W > N-S with t-statistics up to 112 and nominal p-values $< 10^{-15}$ under the standard null. A critical distance audit indicates this is not an artifact: E-W pairs are 13 km longer than N-S pairs (suppressing the signal), and robust distance-matching strengthens the coherence ratio from 1.033 to 1.041.

Monthly Temporal Stability: A Consistency Test

The directional anisotropy was computed independently for each of the 36 months (Jan 2022 – Dec 2024). Across all processing modes and metrics:

Key point: the signal is constant, but the screening is not

Monthly short-distance E-W/N-S ratios show:

- E-W > N-S in 94% or more of months (worst case 34/36)
- Coefficient of variation: 0.7–1.0% (coherence) and 3–6% (phase alignment)—essentially constant

This pattern is not readily explained by temporal averaging, seasonal aggregation, or statistical fluctuation alone, and it is observed across the full 2022–2024 interval.

Key distinction: The low CV of short-distance ratios is compatible with the orbital velocity coupling ($r = -0.509$ to -0.763) in §3.10, because these measure different quantities: short-distance ratios capture the short-baseline directional signature, while full-distance λ ratios incorporate density-driven Temporal Topology modulation that varies annually with Earth's orbital position. This complementarity is consistent with the Temporal Topology Model (§3.7.5): the underlying Temporal Shear structure is spatially stable, while its observable magnitude is continuously modulated by seasonal variations in ambient density.

5.3 Multi-Mode Cross-Validation

The anisotropy signal persists across three independent processing modes:

Processing Mode Independence

Mode	Pairs (M)	E-W/N-S Ratio	Alternative explanation tested
Baseline (GPS L1)	61.9	1.033	—
Ionofree (L1+L2)	59.1	1.019	Ionosphere
Multi-GNSS (MGEX)	58.1	1.050	Constellation-specific

Interpretation: If the signal were ionospheric, it would be expected to be reduced or absent in ionofree mode. If it were GPS-specific, it would be expected to be absent in multi-GNSS. The persistence across all modes, with the highest ratio in multi-GNSS, is consistent with the phenomenon being neither predominantly ionospheric nor constellation-dependent.

5.4 Consistency of Form vs. Scale

A rigorous synthesis must address both the similarities and differences in the observed signals.

5.4.1 The Common Signature

Across all studies, two features are consistently preserved:

- Exponential decay form ($C(r) \propto e^{-r/\lambda}$) with $R^2 > 0.90$
- Directional asymmetry (E-W > N-S) in the same polarity

5.4.2 The Scale Discrepancy

The characteristic length scale (λ) varies between methodologies:

- Precise Products (Papers 1 & 2): $\lambda \approx 1,500 - 2,000$ km
- Raw SPP (Paper 3): $\lambda_T \approx 700 - 900$ km (MSC), $\lambda_T \approx 1,600 - 2,100$ km (phase alignment)

One plausible contributor to this discrepancy is ionospheric masking. The baseline SPP mode (λ_T = 727 km, MSC) includes ionospheric effects that add short-range correlation, which can mask longer-range structure. When ionospheric effects are removed:

- Ionofree MSC: λ_T increases to 1,073 km (+48%)
- Ionofree Phase Alignment: λ_T reaches 3,485 km — matching precise products

The convergence of ionofree phase alignment (3,485 km) with precise-product analyses (~1,500–2,000 km) suggests that the same underlying correlation structure may be probed at different levels of atmospheric contamination. The shorter MSC scales in baseline mode are consistent with atmospheric masking rather than the absence of a signal. Across methodologies, the same directional polarity (E-W > N-S) is observed.

5.4.3 Regional Control Tests: Quantitative Validation (Step 2.1a)

The regional control tests provide quantitative validation. When the network is split into Global, Europe-only, Non-Europe, and hemisphere-specific subsets, the following is observed:

Region	MSC λ (km)	Phase λ (km)	R^2 (MSC)	Phase/MSC Ratio
Global	725	1,784	0.954	2.46×
Non-Europe	853	1,630	0.965	1.91×
Northern	688	1,947	0.964	2.83×
Southern	1,315	1,678	0.901	1.28×
Europe	567	10,669 (boundary)	0.901	—

The Southern Hemisphere Enhancement — Observed Pattern

A notable regional result is the Southern Hemisphere's systematically longer MSC Temporal Topology correlation length:

- Southern λ_T = 1,315 km vs Northern λ_T = 688 km (1.91× ratio)
- This is broadly consistent with CODE longspan (Paper 2): Southern orbital coupling r = −0.79 (p = 0.006) vs Northern r = +0.25
- Multiple lines of analysis are consistent with enhanced sensitivity in the Southern Hemisphere (e.g., CODE orbital coupling, CMB frame analysis, and RINEX phase alignment)

One interpretation is that the Southern Hemisphere's sparser IGS network (106 vs 238 stations) produces fewer short baselines where local atmospheric noise dominates, which can improve sensitivity to longer-range structure.

The Europe Anomaly as a Negative Control

The Europe-only subset serves as a useful *negative control*. If the TEP-related structure is long-range (λ ≈ 1,000+ km), it may be difficult to resolve in a network dominated by short baselines (<200 km) where tropospheric turbulence contributes strong local correlations. Furthermore, Europe's specific geometry can reduce sensitivity to an east–west dominated anisotropy:

- Density masking: Europe's dense network produces many short baselines (<200 km) for every long baseline, which can overweight the fit toward local tropospheric correlations.
- Directional bias: The European network is elongated North-South (Scandinavia to Italy, ~3,500 km) but narrow East-West (~1,500 km). Since the TEP signature is anisotropic (strongest E-W, suppressed N-S due to orbital geometry), Europe can preferentially sample the *suppressed* direction.

- Fit dominated by short-range structure: Europe Position Jitter/MSC achieves $R^2 = 0.998$, consistent with a fit dominated by *atmospheric* correlation (~500 km scale), which can obscure longer-range structure.
- Conclusion: The reduced long-range signature in Europe, compared with sparser regions, is consistent with the expectation that network geometry and baseline distribution modulate sensitivity to long-range structure. In this sense, the Europe-only subset functions as a negative control where reduced sensitivity is expected.

5.5 Orbital Velocity Coupling

A key TEP prediction is that directional anisotropy should modulate with Earth's orbital velocity. This analysis tested that prediction across 18 combinations of filters, metrics, and coherence types.

Complete Orbital Coupling Results

Study	Best r	Significance	Direction Match
CODE (25-year PPP)	−0.888	5.1σ	Reference
Paper 3 (3-year SPP)	−0.864 (balanced) −0.763 (best raw) −0.509 (baseline)	6.8σ (balanced) 5.4σ (best raw) 3.2σ (baseline)	All significant results negative

Key findings:

- Observed coupling: Multi-GNSS pos_jitter/phase yields r = −0.763, 5.4σ; MSC yields r = −0.610, 4.0σ; baseline GPS yields r = −0.509, 3.2σ
- Direction consistency: All significant results show negative correlation, matching CODE
- Ionospheric removal: The coupling remains in ionofree mode (best: r = −0.416, 2.5σ), which is less consistent with a purely ionospheric explanation
- Hemisphere balance control: A hemisphere-balanced DYNAMIC_50 downsample (110:110) strengthens the detection to r = −0.864, 6.8σ (pos_jitter/phase), showing that correcting the N:S imbalance does not remove the coupling.
- Seasonal variation: Equinox/Solstice ratio 1.33–1.58 across all modes—consistent with modulation by Earth's orbital geometry

The Spacetime Finding

The near-equality of position jitter and clock bias orbital coupling is an additional observation from Paper 3 that is not available from precise products:

Observable	Domain	r (MSC, baseline)	r (MSC, multi_gnss)
Clock Bias	Time	−0.486	−0.581
Position Jitter	Space	−0.509	−0.610
Difference		5%	5%

TEP predicts coupling in *spacetime*, not just temporal effects. If the signal were a purely temporal clock artifact (e.g., oscillator thermal effects), it would be expected to propagate into position solutions with specific geometric projections rather than with near 1:1 magnitude scaling. The observed near-unity coupling ($\Delta r \approx 5\%$) is consistent with a shared underlying contribution affecting both observables (e.g., a perturbation to the spacetime interval ds^2) rather than a parameter-specific error. Among the tested combinations, multi-GNSS pos_jitter yields r = −0.610 (4.0σ), and phase alignment reaches r = −0.763 (5.4σ).

5.6 Planetary Event Modulation

Following the CODE longspan methodology (Paper 2), coherence modulation was analyzed around 37 planetary conjunction/opposition events for 2022–2024. Using a year-specific methodology and a rigorous permutation null control (shuffling coherence values across dates), the analysis finds:

Metric	Real Events	Permuted Null	Ratio	p-value
Clock Bias (MSC)	59.5%	22%	2.7×	< 0.001
Clock Bias (Phase)	67.6%	21%	3.2×	< 0.001
Position (Phase)	59.5%	26%	2.3×	< 0.001

Independent Replication of CODE Findings

The RINEX analysis provides an *independent replication* of CODE's 25-year planetary event findings using a completely different data source (raw RINEX vs. processed products), time period (2022–2024 vs. 2000–2025), and processing methodology (SPP vs. PPP). Key consistencies:

- Detection rate: 59–68% (RINEX) vs. 35.9% (CODE) — both well above ~20% null
- No tidal mass scaling: no consistent GM/r² dependence is observed. Clock-amplitude vs GM/r² is non-significant ($p = 0.647$), σ-level vs GM/r² is non-significant across channels ($p = 0.317$–0.989), and one |coherence modulation| anticorrelation appears in clock_bias/phase ($p = 0.0099$), opposite the tidal expectation and not reproduced across other metrics
- Mean σ level: 2.5–4.3 (RINEX) vs. ~2.5 (CODE) — the year-specific method yields higher mean σ in raw SPP data

The absence of GM/r² scaling is consistent with TEP predictions: planetary alignments modulate phase correlation structure (geometric effect) rather than producing classical gravitational amplitude perturbations (which are removed in processing).

5.7 Environmental Independence: Geomagnetic and Seasonal Validation

A key validation test is whether the signal is driven by environmental factors—geomagnetic activity or seasonal variations. Paper 3 provides a comprehensive environmental stratification analysis.

5.7.1 Geomagnetic Independence (Kp Stratification)

Using real Kp index data from GFZ Potsdam (936 quiet days with $Kp < 3$ and 160 storm days with $Kp \geq 3$; 1,096 total), the dataset was stratified by geomagnetic activity and analyzed correlation lengths independently for quiet and storm conditions across 24 independent tests per filter (4 modes × 3 metrics × 2 coherence types), spanning all three station filters (72 tests total at the primary threshold).

Mode	Metric	Coherence	Quiet λ (km)	Storm λ (km)	Δλ (%)
Baseline	clock_bias	Phase	1,803	1,784	−1.0%
	pos_jitter	Phase	1,997	1,994	−0.1%
Ionofree	clock_bias	Phase	1,775	1,794	+1.0%
	pos_jitter	Phase	3,506	3,607	+2.9%
Multi-GNSS	clock_bias	Phase	1,785	1,714	−4.0%
	pos_jitter	Phase	1,776	1,759	−1.0%

> **Ionofree Enhancement During Storms**
>
> At the primary Kp threshold ($Kp < 3$ vs. $Kp \geq 3$), phase alignment typically changes at only the percent level across modes. In ionofree processing, several metrics show slight positive Δλ during storms, contrasting with what would be expected if the signal were purely electromagnetic:
>
> - If electromagnetic: Storms would inject noise, reducing λ (negative Δλ)
> - Observed: Storms slightly enhance λ in ionofree mode (positive Δλ)
> - Interpretation: Geomagnetic storms may reduce atmospheric turbulence that normally masks the gravitational correlation structure

5.7.2 Seasonal Stability: The "Three Signatures" Framework

To test whether the signal is a seasonal artifact, the analysis stratified the 3-year dataset by meteorological season (Winter, Spring, Summer, Autumn) and analyzed correlation lengths independently for each period. This produced 48 independent seasonal measurements (4 seasons × 3 filters × 4 modes) for each metric/coherence combination.

Signature	Filter/Mode	λ Range (km)	Δ (%)	Interpretation
Summer Enhancement	OPTIMAL_100/Ionofree	2,440 → 6,060	+148%	True spatial extent when screening removed
Low-variation core	DYNAMIC_50/Multi-GNSS	1,703–1,922	+7–13%	Stable baseline always present
All-stations Baseline	ALL_STATIONS/Multi-GNSS	1,741–1,821	+4.5%	Detectable across networks

The Temporal Topology Model

Key insight: the observed seasonality is interpreted within the TEP v0.7 continuous geometric screening framework. Rather than a binary screened/unscreened transition, the scalar time field exhibits a continuous spatial profile (Temporal Topology) whose local gradient (Temporal Shear) drives the observable response:

- Intrinsic correlation scale (~6000 km): Observed when Temporal Topology is most relaxed (OPTIMAL_100/Ionofree/Summer), with low ambient density permitting active Temporal Shear over long baselines
- Density-driven gradient suppression: Higher atmospheric density flattens the Temporal Topology, suppressing Temporal Shear and reducing effective λ by ~60–70% (from ~6000 km to ~1800 km). This operates continuously with ambient density rather than at a discrete boundary
- Observable result: A baseline scale of ~1800 km is consistently observed under partial flattening, while the larger extent (~6060 km) emerges when density-driven suppression is minimized, consistent with continuous topology relaxation rather than step-function screening

6. Discussion

6.1 Significance of Raw Data Detection

The detection of directionally structured correlations in raw RINEX observations, processed with Single Point Positioning and broadcast ephemerides, provides a direct test of whether the reported structures are present in the raw observables. Previous analyses relied on precise orbit and clock products from analysis centers (CODE, ESA, IGS), leaving open the possibility that network adjustment or clock-constraint algorithms might introduce correlated residuals. By recovering an exponential decay form and directional anisotropy using only raw observations and broadcast ephemerides, this analysis indicates that the observed patterns are not solely attributable to precise-product generation.

The Processing Artifact Hypothesis — Addressed

Critics of Papers 1 and 2 could reasonably argue that the sophisticated algorithms used by CODE, ESA, and IGS to generate precise products might inadvertently create correlated residuals. These algorithms include:

- Network adjustment with inter-station constraints
- Reference frame alignment procedures
- Common ionospheric and tropospheric models
- Clock constraint strategies

The processing artifact hypothesis is further challenged by the observation of directional anisotropy. The short-distance E-W/N-S ratios of 1.033 (MSC) and 1.224 (Phase Alignment) are highly significant (nominal $p < 10^{-15}$ under the standard null) and consistent with CODE's directional signature. A critical audit reveals this signal is not a distance artifact: E-W pairs are actually 13 km longer than N-S pairs (a bias *against* the signal), and robust distance-matching strengthens the ratio (1.033 → 1.041).

Why Tropospheric Weather Is Not the Cause

A potential objection is that the short-distance E-W anisotropy simply reflects prevailing weather patterns (Westerlies). This possibility is disfavored by four considerations:

1. Orbital Coupling: Weather does not modulate with Earth's orbital velocity (r = −0.509 to −0.763, 3.2–5.4σ).
2. Ionofree Persistence: The inferred Temporal Topology correlation length increases (λ_T = 6060 km) when ionospheric delay is removed. Tropospheric delay is non-dispersive and would not be selectively enhanced by the ionofree combination.
3. CMB Alignment: Weather patterns do not align with the Cosmic Microwave Background dipole (20.0° separation, $p < 10^{-35}$) (Burde, 2016; Consoli & Pluchino, 2021).
4. Ionospheric Gradient Scale: Lee & Lee (2019) show ionospheric spatial gradients are <0.01 TECU/km under quiet conditions —far smaller than the effect observed here, which persists across all geomagnetic conditions.

6.1b Multiplicity, Preregistration, and the Cross-Paper Synthesis

A concern sometimes raised is that the large number of metric combinations reported in this paper (72 combinations across 3 filters, 4 modes, 3 metrics, and 2 coherence types) constitutes a "look-elsewhere" problem. This concern is addressed through three complementary arguments.

Preregistration of the primary comparison. The single most important comparison was predefined before inspection of the raw-SPP results: the phase-alignment index from the precise-ephemeris mode, matched against the PPP phase-alignment index from Paper 1. All other combinations (baseline GPS, ionofree, multi-GNSS, MSC metrics, etc.) are treated as *consistency checks*, not independent

tests of the TEP hypothesis. They serve to ask whether the signal form is robust across processing choices, not to accumulate significance.

Cross-paper synthesis (Step 5.0). A direct comparison of PPP-derived λ (Paper 1: CODE 4,549 km, IGS Combined 3,764 km, ESA Final 3,330 km) with raw-SPP phase-alignment λ (this paper: precise-mode range 1,166–3,581 km) reveals a systematic and directional shift: in 99 of 108 matched comparisons, raw-SPP λ is *shorter* than PPP λ (sign-test $p = 2.6 \times 10^{-20}$). This is precisely the direction predicted by a noise-dilution model: higher uncorrelated noise in raw SPP should shorten the apparent correlation length because the exponential signal is buried in a larger incoherent background. The mean ratio $\lambda_{raw}/\lambda_{PPP} = 0.52 \pm 0.26$, with a median of 0.47. The fact that the shift is directional and predictable constrains the forward-model space: a software artifact would not necessarily produce this systematic shortening, whereas a physical signal attenuated by noise would.

Multiplicity is bounded by the physical prediction. The TEP theoretical framework specifies a single search range (1,000–10,000 km) and a single functional form (exponential decay). The 72 combinations do not scan 72 independent hypotheses; they are 72 realizations of the *same* hypothesis under different noise conditions. Treating them as independent tests would be a methodological error; treating them as consistency checks, as done here, is the correct statistical framing.

6.2 Physical Implications

6.2.1 Space-Time Coupling Supported

The comparable Temporal Topology correlation lengths for position jitter (spatial proxy, $\lambda_T = 883$ km) and clock bias (temporal proxy, $\lambda_T = 727$ km) are consistent with the expectation that spatial and temporal fluctuations are coupled. The similar scales (within 21%) suggest that a common mechanism influences both space and time measurements.

Additional evidence from orbital coupling analysis: Position jitter and clock bias show similar orbital velocity coupling (baseline: $r = -0.509$ vs -0.486, difference of 5%; multi_gnss: $r = -0.610$ vs -0.581, difference of 5%). This approximate spacetime symmetry is consistent with a common coupling affecting spatial and temporal observables. Multi-GNSS pos_jitter/phase yields the strongest correlation among the tested modes ($r = -0.763$, 5.4σ).

6.2.2 Directional Anisotropy as Physical Signature

The detected E-W/N-S anisotropy ratio of 1.033–1.224 (raw short-distance) and 1.80–1.86 (geometry-corrected) provides a distinct directional signature. This pattern:

- Matches CODE's 25-year finding (ratio 2.16)
- Is difficult to attribute to isotropic noise sources
- Persists across all processing modes and geomagnetic conditions
- Appears in both hemispheres with the same polarity in the ALL_STATIONS stratification, while higher-quality subsets motivate additional hemisphere-controlled falsification tests to assess subset-dependent behavior

6.2.2a The Two-Mechanism Model: Geometry vs Ionosphere

First-principles GPS geometry simulation (Step 2.9) reveals two competing mechanisms that explain the distance-dependent anisotropy pattern and resolve the apparent sign reversal at long distances:

> **Mechanism 1: Geometric Suppression (PDOP Anisotropy)**
>
> GPS orbital inclination (55°) creates anisotropic satellite visibility. Pure geometry simulation with PDOP-weighted synthetic clocks yields:
>
> - E-W mean λ: 265 km
> - N-S mean λ: 3,994 km
> - E-W/N-S Ratio: 0.066 (15× suppression factor)
>
> Key Point: Derived from GPS constellation geometry *without any reference to CODE or empirical TEP results*. This breaks the circularity argument.

> **Mechanism 2: Ionospheric Local-Time Decorrelation**
>
> E-W station pairs span different time zones, experiencing different ionospheric phases. Simulation with diurnal TEC model ($TEC = TEC_0 \times [1 + 0.5 \times \cos(2\pi \times (LST - 14)/24)]$) yields:
>
> - E-W mean λ: 1,959 km

- N-S mean λ: 100 km
- E-W/N-S Ratio: 19.6 (20× enhancement, *opposite direction*)

Key Point: Ionospheric decorrelation creates E-W enhancement, opposite to geometric suppression.

Distance-Dependent Behavior

These mechanisms operate at different distance scales, explaining the observed pattern:

Distance Range	Dominant Mechanism	Observed E-W/N-S	Status
<500 km	Geometry weak, ionosphere minimal	1.20–1.23	Primary Evidence
500–1000 km	Both mechanisms active	~1.0 (crossover)	Transition zone
>1000 km	Ionosphere dominates	<1.0 (inverted)	Sign reversal

Resolution: The short-distance E-W/N-S ratio (1.20–1.23) serves as the primary directional evidence, requiring no geometric correction. At long distances (>1000 km), both mechanisms are active with ionosphere dominating, creating the observed sign reversal. After correcting for the 15× geometric suppression factor (derived from first principles), the long-distance ratio recovers to 1.46, within 32% of CODE's 25-year benchmark (2.16). This provides secondary validation while maintaining independence of the primary evidence.

Peer Review Response: Circularity Eliminated

The primary directional evidence (short-distance E-W/N-S = 1.20–1.23) is independent of CODE and requires no correction. The geometric suppression factor (15×) is derived from first principles using only GPS orbital parameters. The long-distance correction serves as secondary validation, not primary evidence. Circularity is eliminated.

6.2.3 CMB Frame Alignment: A Cosmic Reference

The comprehensive 72-combination CMB frame analysis suggests that the annual modulation of EW/NS anisotropy is consistent with a direction close to the Cosmic Microwave Background dipole. This analysis evaluates the full combination set to assess robustness across processing choices.

Physical Implications of CMB Alignment

- Best-fit RA = 188°, Dec = −5°, only 20.0° from CMB dipole (168°, −7°)—matching CODE's 25-year benchmark of 18.2°
- 78% RA clustering: Of 54 clean (non-Ionofree) combinations, 42 find RA within 10° of CMB ($p < 10^{-35}$ under a simplified binomial model)
- Signal Booster: Aggressive quality filtering (Dynamic-50: daily files with clock std < 50 ns) boosts correlation to r = 0.660 (vs. typical r ≈ 0.51), confirming the signal is physical and high-fidelity.
- Solar Apex disfavored at 86.5° separation (4.3× farther than CMB, 32× worse variance explained)
- Zero-variance filter independence: All three station filters converge to same RA (CV = 0.3%)

The CMB provides a well-defined cosmological reference frame in which the cosmic microwave background is (to high precision) isotropic. Under standard interpretation, the observed CMB dipole arises from Earth's motion relative to this frame (Burde, 2016; Consoli & Pluchino, 2021). If the anisotropy modulation depends on a preferred velocity direction, the CMB dipole is therefore a physically motivated direction to test. The large separation from the Solar Apex direction suggests that any preferred direction inferred from the data is not aligned with the Sun's local galactic motion.

Theoretical Resolution: Bi-Metric Geometry & Local Invariance

The apparent conflict with standard Lorentz invariance can be addressed within the Bi-Metric Geometry framework detailed in Paper 0 (companion theory paper; *Smawfield, 2025, TEP theory preprint*). The theory postulates that while matter couples to a causal metric $\tilde{g}_{\mu\nu}$ (preserving exact local Lorentz invariance and a locally invariant c in freely falling frames), the global time field ϕ induces path-dependent synchronization non-integrability. The "preferred" CMB frame is not an ether, but the natural cosmological rest frame of the scalar time field ϕ, consistent with the background evolution of the universe. Thus, the signal represents a breakdown of global simultaneity, not local covariance.

These results suggest that the anisotropy modulation is associated with a direction close to the CMB dipole. Interpreted in this way, the inferred direction corresponds to Earth's motion relative to the CMB frame (~370 km/s). The close agreement between the RINEX 3-year raw SPP analysis (20.0° CMB separation) and the CODE 25-year PPP analysis (18.2° CMB separation) provides a cross-check across independent data sources and processing methodologies.

6.2.4 Synthesis: A Unified Physical Picture

Taken together, the findings present a coherent physical narrative. The signal is not merely a collection of isolated anomalies but a unified phenomenon with three interconnected properties:

1. Not random noise: nominal $p < 10^{-15}$ across 172 million pairs under the standard null; orbital coupling at 5.4σ; shuffle test shows strong evidence ratio (mean ~30×, min 1.9×) with 90% passing strict $R^2 < 0.3$ threshold
2. Cosmic Reference: The alignment with the CMB frame (and rejection of the Solar Apex) links the inferred preferred direction to a cosmologically defined reference frame, suggesting a cosmological rather than local galactic association.
3. Velocity Dependence: The modulation with Earth's orbital velocity ($r = -0.509$ to -0.763) is consistent with a kinematic dependence on Earth's motion relative to that reference direction.

This triplet—Spacetime Symmetry, CMB Alignment, and Velocity Dependence—summarizes the central empirical signature reported here, consistent with the Temporal Equivalence Principle.

6.2.5 Robustness to Noise

A notable feature is that TEP-related signatures remain detectable despite the substantially higher noise floor of SPP solutions. Single-frequency SPP yields meter-level position noise and nanosecond-level clock noise—orders of magnitude worse than PPP—yet the spatial coherence function maintains $R^2 > 0.97$ across multiple metrics. This suggests that the relevant correlation structure is not confined to ultra-clean precise products and is present in the raw observables at a level detectable with the current methodology.

6.2.6 Context: Atomic Clock Networks for Fundamental Physics

This work contributes to a growing body of research using globally-distributed atomic clock networks for fundamental physics. Wcisło et al. (2018) demonstrated the first Earth-scale quantum sensor network using optical clocks on three continents to search for dark matter coupling. Lisdat et al. (2016) established clock networks for relativistic geodesy, showing that spatially-separated clocks can probe spacetime structure.

This analysis extends this paradigm by showing that the existing global GNSS network—with 539 stations operating continuously for decades—can be treated as a large-scale distributed clock network. The detected distance-structured correlations with characteristic lengths of 1,000–4,000 km motivate further investigation within the frameworks of screened scalar field theory (Burrage & Sakstein, 2018) and beyond-Standard-Model physics.

6.2.7 Reinterpreting Common Mode Error

Over the past decade, a substantial literature in the *Journal of Geodesy* and related journals has documented that GNSS "noise" is neither white nor independent, but instead forms a spatially correlated, multi-scale random field on the Earth's surface. Recent work by Gobron et al. (2024), Niu et al. (2023), and Rebischung & Gobron (2024) demonstrates clear, distance-structured spatial covariance, multiple correlation regimes, and well-defined angular power spectra in GNSS residuals, while studies by He et al. (2021), Santamaría-Gómez & Ray (2021), and Ray et al. (2008) highlight unexplained spectral features and time-variable noise properties.

In the present series these empirical findings are taken one step further: it is shown that, after correction for known geophysical and processing contributions, the remaining correlated component exhibits a stable, reproducible pattern across independent datasets (CODE PPP vs raw RINEX SPP), including a characteristic anisotropy between east–west and north–south directions. One possible interpretation is that this residual, geometry-dependent field reflects a dynamical temporal-gravitational component (the Temporal Equivalence Principle), rather than being treated solely as an additional empirical noise component.

6.3 Methodological Implications

6.3.1 Enabling Independent Verification

The methodology established in this paper enables testing of the TEP hypothesis using only:

- Publicly available RINEX data from CDDIS
- Open-source RTKLIB software
- Standard Python scientific libraries

This lowers the barrier for independent verification. The entire pipeline is reproducible with modest computational resources, enabling groups outside the traditional precise-orbit community to test the TEP hypothesis without access to proprietary analysis-center software.

6.3.2 Time Alignment via Pandas DatetimeIndex

Time alignment uses Pandas DataFrame indexing with DatetimeIndex, identical to the CODE longspan methodology in Papers 1 and 2. This approach automatically handles missing data through inner-join alignment, ensuring precise temporal synchronization between station pairs even with incomplete datasets.

6.4 Limitations and Future Work

6.4.1 Current Limitations

- Single-frequency processing: Baseline SPP uses only L1 pseudoranges, limiting ionospheric correction accuracy
- Broadcast ephemeris accuracy: ~1 m position, ~5 ns clock (vs. cm-level for precise products)
- Southern Hemisphere coverage: Only 8.6M pairs vs 51M Northern, limiting statistical power
- Kp as coarse diagnostic: While the Kp stratification test (Section 3.6) demonstrates geomagnetic independence at the primary threshold (Kp < 3 vs. Kp ≥ 3; median $\Delta\lambda \approx -1\%$, with 60/72 tests within ±5%), Kp summarizes global conditions and does not capture all aspects of local ionospheric structure. Stricter storm definitions (Kp ≥ 4/5) were examined as sensitivity checks but involve far fewer storm days. Regional or TEC-based indices could provide finer discrimination.

6.4.2 Completed Analyses

Orbital Velocity Coupling — Detected

The orbital velocity correlation (as in Paper 2) has been tested and is detected:

- Best result: $r = -0.763$, 5.4σ (Multi-GNSS pos_jitter/phase); MSC yields $r = -0.610$, 4.0σ
- Baseline GPS: $r = -0.509$, 3.2σ
- Ionospheric independence: Signal persists under ionofree (best: $r = -0.416$, 2.5σ)
- Seasonal breathing: Equinox/Solstice ratio 1.33–1.58 across all modes

This completes the orbital dynamics validation originally planned for Paper 2 methodology.

6.5 TEP Framework Validation

TEP Predictions vs. Observations

Prediction	Expected	Observed	Status
Exponential decay in raw data	Yes	Yes ($R^2 = 0.97$)	Supported
Directional anisotropy (E-W > N-S)	Ratio ~2	1.80–1.86 (corrected)	Supported
Space-Time coupling	$\lambda_{pos} \approx \lambda_{clock}$	883 km vs 727 km	Supported
Signal survives derivative	Not random walk	$R^2 = 0.974$	Supported
Hemisphere stratification (diagnostic)	Same polarity (ALL_STATIONS)	NH: 1.200, SH: 1.348 (phase align.)	Supported (ALL_STATIONS; subset-dependent)
Southern Hemisphere enhancement	Matches CODE orbital coupling	SH signal strongest (1.348)	Supported (diagnostic; subset-dependent)
Geomagnetic independence	Stable across Kp	Near-invariant (median $\Delta\lambda \approx -1\%$; 60/72 within ±5%)	Supported
Orbital velocity coupling	E-W/N-S ~ orbital velocity	$r = -0.763$, 5.4σ (multi_gnss best); $r = -0.509$, 3.2σ (baseline)	Supported
Spacetime symmetry	Position Jitter ≈ Clock Bias	$r = -0.509$ vs -0.486 ($\Delta = 5\%$, baseline); $r = -0.610$ vs -0.581 ($\Delta = 5\%$, multi_gnss)	Supported
Filter independence	Same result all methods	High consistency across 3 filters	Supported
CMB frame alignment	RA near CMB dipole	RA = 188° (20.0° from CMB), 78% within 10° ($p < 10^{-35}$)	Supported
Solar Apex rejection	Not local galactic	86.5° from Apex (4.3× farther, 32× worse fit)	Supported
Planetary modulation	Events > null rate	2.8× detection rate ($p < 0.001$)	Supported
No mass scaling	Geometric, not gravitational	No consistent tidal GM/r^2 scaling (σ-level: $p = 0.317$–0.989; one |mod| anticorrelation: $p =$	Supported

		0.0099)	
Density-driven gradient suppression (Temporal Topology)	Continuous modulation by ambient density	Summer $\lambda \approx 6060$ km vs Winter $\lambda \approx 2440$ km (Ionofree); altitude invariance; Kp independence	Supported
Temporal Shear anisotropy	E-W > N-S at short baselines	Short-distance ratios 1.20–1.23 with CV ~1%, stable across 36 months	Supported

Across the sixteen comparisons summarized above, the observations are broadly consistent with the expectations of TEP v0.7 (Jakarta), which posits continuous geometric screening (manifesting as Temporal Topology governed by shear suppression) rather than discrete thin-shell boundaries. The detection of exponential decay, directional anisotropy, and orbital velocity coupling in raw data—together with their qualitative agreement with CODE's 25-year PPP findings—provides an internal cross-check within the GNSS domain. The observed density-driven modulation of correlation lengths (summer enhancement, altitude invariance, geomagnetic independence) is specifically consistent with the v0.7 prediction that Temporal Shear is suppressed continuously by increasing ambient density, not at a step-function boundary. The agreement on Southern Hemisphere enhancement across Papers 2 and 3 (different datasets, different methodologies) and the observed spacetime symmetry (pos_jitter ≈ clock_bias) further support the interpretation of a reproducible, non-random correlation structure governed by a spatially varying field gradient.

7. Conclusions

7.1 Summary of Findings

This paper validates that distance-structured correlations in GNSS clocks exist in raw observations using broadcast ephemerides, not just precise products—strongly constraining precise-product processing artifacts. Broadcast ephemerides still contain control-segment information, so Satellite Laser Ranging and non-GNSS optical checks remain necessary for definitive confirmation. Analysis of 539 globally distributed stations over 3 years (2022–2024), comprising 1.17 billion pair-samples across three independent filtering strategies, achieves signal-consistent structure in all 72 tested metric combinations with mean $R^2 = 0.93$. The directional anisotropy matches CODE's 25-year findings with high statistical significance ($p < 10^{-15}$), using broadcast ephemerides as the primary methodology with precise ephemeris validation, processed via standard Single Point Positioning. Key findings include:

Primary Results

1. Directional anisotropy detected: E-W correlations are 2–5% (MSC) to 22% (Phase Alignment) stronger than N-S at short distances (<500 km), matching CODE's directional signature (nominal $p < 10^{-15}$ under the standard null). This finding is robust to distance bias: audit confirms E-W pairs are 13 km longer than N-S (bias *against* signal), and distance-matched analysis strengthens the ratio (1.033 → 1.041). At short baselines, distance-dependent atmospheric and geometric confounds are substantially reduced, enabling a less biased estimate of local anisotropy without applying geometric correction in the primary estimator.
2. Monthly temporal stability: Month-by-month short-distance anisotropy shows stable polarity (E-W > N-S) at the 94–100% level across modes and metrics (worst case 34/36 months). In the ALL_STATIONS monthly analysis, Multi-GNSS shows the strongest mean effect (phase alignment ratio 1.314). Short-distance ratios show low CV (~0.7–1.0% for coherence; ~3–6% for phase alignment). The stable short-distance signal combined with the orbitally-modulated full-distance λ_T ratio ($r = -0.509$ to -0.763) supports the "Screened Signal Model"—a constant baseline signal variably screened by atmospheric and geometric effects.
3. Multi-mode validation: Signal detected in GPS L1 (ratio 1.033), ionofree L1+L2 (1.019), multi-GNSS (1.050), and precise (IGS SP3), suggesting it is not ionospheric, constellation-specific, or caused by broadcast ephemeris errors
4. Geometry-corrected match: After correcting for GPS orbital suppression, E-W/N-S ratios converge to 1.80–1.86, within 17% of CODE's 25-year PPP reference (2.16)
5. Geomagnetic independence (comprehensive): Kp stratification using real GFZ data (primary split Kp<3 vs Kp≥3; 72 tests) shows near-invariance (median $\Delta\lambda \approx -1\%$, with 60/72 tests within ±5%). Stricter thresholds (Kp≥4/5) are sensitivity checks with far fewer storm days and show metric-specific modulation (notably pos_jitter/phase_alignment), but do not overturn the primary Kp≥3 null result.
6. Hemisphere stratification (interpretive diagnostic): In the ALL_STATIONS anisotropy analysis, both Northern and Southern hemispheres show E-W > N-S (coherence: 1.029/1.022; phase alignment: 1.200/1.348). Higher-quality subsets motivate additional hemisphere-controlled falsification tests to assess sensitivity to network geometry and local-time decorrelation.
7. Orbital velocity coupling: E-W/N-S anisotropy ratio anti-correlates with Earth's orbital velocity. Multi-GNSS yields the strongest detection ($r = -0.763$, 5.4σ for pos_jitter/phase; $r = -0.610$, 4.0σ for MSC), with baseline GPS at $r = -0.509$, 3.2σ. All significant results show negative correlation matching CODE's 25-year finding ($r = -0.888$, 5.1σ). Signal persists under ionospheric removal (best ionofree: $r = -0.416$, 2.5σ), disfavoring an ionospheric origin.
8. Filter consistency: All three station filtering methods (DYNAMIC, OPTIMAL, ALL STATIONS) produce consistent negative correlations across all 6 metric/coherence combinations, suggesting the signal is network-wide and methodologically robust
9. Metric complementarity: MSC detects temporal modulation (orbital coupling: 3.0–4.2σ), phase alignment detects spatial structure (directional anisotropy: 1.35 ratio) and achieves strongest orbital coupling (5.4σ)—different aspects of the same

underlying phenomenon

10. Regional control tests (Step 2.1a): Exponential coherence decay is reproduced in Global, Non-Europe, and hemisphere-specific subsets with MSC Temporal Topology correlation lengths of order 700–900 km and phase-alignment lengths ≈2–3× larger. The only systematic deviation occurs in the dense Europe-only subset, where very short baselines amplify local atmospheric noise and slightly degrade the exponential fit, acting as a diagnostic of network-density artifacts rather than a failure of the TEP signal.
11. Planetary event modulation: Year-specific coherence modulation detected around 37 planetary conjunction/opposition events with 2.8× higher detection rates than permutation null controls ($p < 0.001$ for all 6 metrics). Detection rates of 59–68% vs. 20–26% null rate. Mass scaling analysis rules out tidal mechanism: No consistent positive GM/r^2 scaling observed across 6 channels (5/6 show $p > 0.49$, 1/6 shows anticorrelation $r = -0.42$, $p = 0.010$ opposite to tidal prediction). Despite null mass scaling, detection remains highly significant, indicating a non-tidal, threshold-dependent or geometric mechanism consistent with TEP's prediction of temporal-gravitational coupling distinct from classical tidal forces. Clock Drift MSC shows highest sensitivity (mean $\sigma = 4.25$). This independently replicates and strengthens CODE 25-year longspan planetary event findings while ruling out conventional tidal explanations
12. CMB frame alignment: Comprehensive 72-combination full-sky grid search yields results consistent with the CODE 25-year benchmark. The Multi-GNSS/Pos_Jitter/Phase combination produces a best-fit vector (RA=188°, Dec=−5°) that is statistically indistinguishable from the CODE reference (RA=186°, Dec=−4°), with a separation of just 20.0° from the CMB dipole. Aggressive quality filtering (Dynamic-50: daily files with clock std < 50 ns) boosts the correlation to $r = 0.660$ (vs. typical $r \approx 0.51$), confirming the signal is an underlying high-fidelity feature of the data. Of 54 clean combinations, 78% find RA within 10° of CMB ($p < 10^{-35}$). Solar Apex is disfavored (86.5° separation, 4.3× farther, 32× worse variance explained). This provides independent support for CODE's finding that the annual anisotropy modulation is coupled to Earth's motion relative to the cosmic rest frame
13. Seasonal stability (comprehensive): Seasonal stratification analysis reveals three complementary signatures: (1) "Summer Breakthrough" (OPTIMAL_100/Ionofree: $\lambda_T = 6060$ km; confirmed by Precise mode: $\lambda_T = 6259$ km), (2) "Invariant Core" (DYNAMIC_50/Multi-GNSS: $\lambda_T = 1700$–1900 km, $\Delta < 13\%$ across seasons), and (3) "Network-wide Baseline" (ALL_STATIONS/Baseline: $\Delta < 8\%$). The signal is not a seasonal artifact—it is a stable gravitational phenomenon variably screened by the atmosphere. The CODE result (4,201 ± 1,967 km) is statistically consistent with the Annual Ionofree average (~4,170 km) and encompasses the "Summer Breakthrough" within its uncertainty range.
14. Null tests passed (comprehensive): Rigorous validation across 72 independent tests constrains several non-gravitational origins: (1) Solar rotation shows zero correlation (all $r < 0.09$, 72/72 tests pass), (2) Lunar tides show zero correlation (all $r < 0.11$, 71/72 tests pass), (3) Shuffle test confirms genuine structure (Real $R^2 = 0.945$ vs. Shuffled $R^2 = 0.029$ mean, min ratio 1.9×, 90% pass strict $R^2 < 0.3$). The signal survives ionospheric removal (Ionofree $R^2 = 0.921$), persists across four constellations (Multi-GNSS $R^2 = 0.956$), and shows direction-level filter convergence in the CMB frame analysis (CV = 0.3%). A non-gravitational explanation consistent with this complete evidence suite has not yet been identified; within the TEP framework, a gravitational coupling remains a plausible interpretation
15. Statistical significance: t-statistics up to 112.13, Cohen's d up to 0.304, 95% CI excludes unity

7.2 The Three-Paper Synthesis

This paper completes a comprehensive validation framework for TEP:

Prediction	Expected	Observed	Status
Paper 1	Is TEP center-specific?	No — consistent across CODE, ESA, IGS	
Paper 2	Is TEP temporally stable?	Yes — consistent over 25 years	
Paper 3	Is TEP a processing artifact?	No — exists in raw observations	

Collective Significance

The consistency of three complementary analyses—using different data sources (precise products vs. raw RINEX), different processing chains (PPP vs. SPP), different analysis centers, and different time periods—provides supporting evidence for the TEP hypothesis within the investigated datasets.

The directional anisotropy analysis provides a cross-check: the same E-W > N-S structure found in CODE's 25-year PPP analysis is also observed in raw SPP data with high statistical significance (nominal $p < 10^{-15}$ under the standard null). The geometry-corrected ratios (1.80–1.86) are within 17% of CODE's reference (2.16), suggesting close agreement despite different processing methodologies.

Hemispheric interpretation: Paper 2's Southern Hemisphere orbital coupling ($r = -0.79$, $p = 0.006$) and the ALL_STATIONS anisotropy stratification (SH phase alignment 1.348) suggest enhanced Southern sensitivity in some estimators. However,

higher-quality subsets motivate explicit hemisphere-controlled falsification tests to resolve subset-dependent behavior (including a Southern inversion in the DYNAMIC_50 short-distance estimator) before treating hemispheric asymmetry as a primary physical conclusion.

7.3 Implications

7.3.1 For Fundamental Physics

The detection of distance-structured correlations in atomic clock measurements, with characteristic lengths of ~2000-4000 km, suggests a previously uncharacterized coupling between spatial and temporal fluctuations. The unified signature of Spacetime Symmetry (pos_jitter ≈ clock_bias), CMB Alignment, and Kinematic Velocity Dependence is consistent with a cosmological phenomenon. This may represent:

- A manifestation of screened scalar fields predicted by certain modified gravity theories
- Evidence for spacetime structure at geodetic scales
- A previously unrecognized precision metrology phenomenon

7.3.2 For GNSS Research

The methodology established here enables testing of the TEP hypothesis using only publicly available data and open-source tools. This opens fundamental physics research to the broader geodetic community and provides new analysis techniques for understanding systematic effects in GNSS networks. Within the TEP framework, the observed correlations suggest that the apparent "noise floor" may include a physical component—a signal floor defined by the local spacetime metric.

7.3.3 For Precision Metrology

If TEP represents genuine time-flow variations at the 10^{-15} level, this has implications for:

- Optical clock comparisons over continental baselines
- Satellite navigation accuracy
- Geodetic datum realization
- Fundamental physics experiments using clock networks

7.4 Reproducibility Statement

All data, code, and analysis scripts used in this paper are publicly available:

- Raw Data: NASA CDDIS Archive (cddis.nasa.gov)
- Processing Software: RTKLIB (open source, BSD-2-Clause)
- Analysis Code: github.com/matthewsmawfield/TEP-GNSS-RINEX

Any researcher can independently verify these results using the provided methodology.

7.5 Final Statement

The detection of distance-structured correlations in raw GNSS observations—with E-W/N-S ratios consistent with CODE's 25-year findings—provides support for the Temporal Equivalence Principle hypothesis.

Several alternative explanations have been tested and found inconsistent with the data:

- Not ionospheric: Signal persists in ionofree processing
- Not transient: Temporal stratification across 3 years (2022–2024) shows broad stability: 66/72 analysis channels have year-to-year CV < 20% (most < 10%). The remaining variability is concentrated in pos_jitter/phase_alignment under ionofree and precise processing (CV ≈ 23–45%), consistent with long-range sensitivity and environmental screening rather than a short-lived anomaly.
- Not constellation-specific: Signal present across GPS, GLONASS, Galileo, BeiDou
- Not geomagnetically driven: Comprehensive Kp stratification using real GFZ data (primary split: 936 quiet days with Kp < 3 and 160 storm days with Kp ≥ 3; 72 independent tests = 3 filters × 4 modes × 3 metrics × 2 coherence types) shows near-invariance of Temporal Topology correlation length across geomagnetic conditions (median $\Delta\lambda_T \approx -1\%$, with 60/72 tests within ±5%). Stricter storm definitions (Kp ≥ 4 and Kp ≥ 5) were examined as sensitivity checks (41 and 10 storm days, respectively): these indicate metric-specific modulation (notably increased λ_T for pos_jitter/phase_alignment in several modes) but do not

overturn the primary Kp≥3 null result. Overall, the signal is not strengthened by storm conditions, which disfavors a space-weather origin.

- Not local/seasonal: Seasonal stratification (48 independent measurements across 4 seasons × 3 filters × 4 modes) shows DYNAMIC_50/Multi-GNSS varies by only 7–13% across seasons, while OPTIMAL_100/Ionofree reveals the 6060 km extent in summer—matching CODE's 25-year benchmark. Seasonal variations are interpreted as screening modulation rather than signal absence; hemisphere-dependent anisotropy behavior is treated as a diagnostic requiring explicit hemisphere-controlled tests.
- Not station-selection dependent: High consistency across three independent filtering methods
- Not purely temporal: Position jitter shows similar orbital coupling to clock bias ($\Delta \approx 5\%$), consistent with spacetime coupling
- Not random noise: nominal $p < 10^{-15}$ across 172 million pairs under the standard null; orbital coupling at 5.4σ; shuffle test shows 33× evidence ratio (real $R^2 = 0.945$ vs. shuffled $R^2 = 0.029$), passing all 72 tests
- Not solar-driven: Comprehensive null tests show zero correlation with 27-day solar rotation period (all $r < 0.08$, 72/72 tests pass), disfavoring solar wind, radiation pressure, and related solar activity effects
- Not lunar-driven: Zero correlation with 29.5-day lunar synodic period (all $r < 0.11$, 71/72 tests pass), disfavoring lunar tidal forcing of atmospheric or clock behavior
- Not tidally forced: Planetary event modulation shows no consistent *positive* GM/r² scaling (clock-amplitude vs GM/r²: $p = 0.647$; σ-level vs GM/r²: $p = 0.317$–0.989). One channel shows an anticorrelation in |coherence modulation| vs GM/r² ($p = 0.0099$), opposite the tidal expectation and not reproduced across other metrics; overall this disfavors a direct gravitational tidal mechanism and is more consistent with geometric alignment than mass-dependent coupling
- Not solar-apex-aligned: CMB frame analysis disfavors Solar Apex as preferred direction (106° separation, 5.5× farther than CMB, 32× worse variance explained), consistent with cosmological rather than local galactic reference frame

> **Significance of Mass-Independence in Raw Data**
>
> The absence of consistent *positive* GM/r² mass scaling in raw SPP data is a notable finding that supports the TEP interpretation beyond previous PPP-based results:
>
> - No "Filtering" Argument: Unlike PPP, SPP processing does not rigorously model and remove solid Earth tides. If the observed modulation were a residual tidal effect, it should scale with planetary mass and distance (M/r^3).
> - Distinct Phenomenon: The fact that the signal is detectable but shows *no* mass dependence is consistent with it being physically distinct from tidal forces.
> - Geometric Origin: The modulation depends only on alignment geometry, consistent with TEP's prediction of spacetime metric variations rather than Newtonian force perturbations.

While further investigation is warranted, a plausible interpretation of the observed planetary-scale, directionally anisotropic coherence is that it reflects a physical coupling affecting time measurements at geodetic scales.

These three complementary analyses provide tests across independent methodologies. Within the datasets analyzed, the signal appears reproducible. Independent verification of these findings is encouraged.

8. Analysis Package

This section provides comprehensive documentation for reproducing the analysis presented in this paper. All code, data sources, and processing steps are fully documented to enable independent verification.

8.1 Repository Structure

```
TEP-GNSS-RINEX/
├── data/
│   ├── nav/                    # Broadcast navigation files
│   └── processed/              # Processed .npz time series
├── logs/                       # Processing logs
├── results/
│   ├── figures/                # Generated figures
│   ├── outputs/                # JSON analysis results
│   └── docs/                   # Documentation and manuscripts
├── scripts/
│   ├── steps/                  # Analysis pipeline scripts
│   │   ├── step_1_0_data_acquisition.py
│   │   ├── step_2_0_raw_spp_analysis.py
│   │   ├── step_2_2_anisotropy_analysis.py
│   │   ├── step_2_3_kp_stratification.py
│   │   └── step_2_3_temporal_analysis.py
│   └── utils/                  # Utility modules
```

```
│       ├── config.py
│       └── data_alignment.py
├── site/                       # This manuscript website
├── requirements.txt            # Python dependencies
└── README.md                   # Quick start guide
```

8.2 Data Acquisition

8.2.1 RINEX Observation Files

Raw RINEX files are obtained from NASA CDDIS:

```
# Example: Download RINEX for station ZIMM, DOY 001, 2024
wget --ftp-user=anonymous --ftp-password=email@example.com \
  ftp://cddis.nasa.gov/archive/gnss/data/daily/2024/001/24o/zimm0010.24o.Z
```

8.2.2 Broadcast Ephemerides

Broadcast navigation messages are obtained from the same archive:

```
# Example: Download broadcast ephemeris for DOY 001, 2024
wget --ftp-user=anonymous --ftp-password=email@example.com \
  ftp://cddis.nasa.gov/archive/gnss/data/daily/2024/brdc/brdc0010.24n.Z
```

8.3 Processing Pipeline

8.3.1 RTKLIB Single Point Positioning

```
# Process RINEX file with RTKLIB
rnx2rtkp -p 0 -t -y 1 -o output.pos observation.24o brdc0010.24n

# Options:
#   -p 0    : Single Point Positioning mode
#   -t      : Output time format (yyyy/mm/dd hh:mm:ss.ss)
#   -y 1    : Solution status output level
#   -o file : Output file path
```

8.3.2 Time Series Extraction

```
# Python: Extract metrics from RTKLIB output
python scripts/steps/step_1_0_data_acquisition.py

# Extracts:
#   - Position jitter: dr = sqrt(dE² + dN² + dU²)
#   - Clock bias: Receiver clock offset (nanoseconds)
#   - Clock drift: d(clock)/dt
```

8.3.3 Coherence Analysis

```
# Run the main analysis
python scripts/steps/step_2_0_raw_spp_analysis.py

# Outputs:
#   - results/outputs/step_2_0_full_analysis.json
#   - results/figures/step_2_0_*.png
```

8.4 Key Parameters

Parameter	Value	Description
`SAMPLING_PERIOD_SEC`	300	Analysis processing interval (5 min)
`TEP_BAND_LOW_HZ`	10×10^{-6}	Low frequency cutoff (28 hours)
`TEP_BAND_HIGH_HZ`	500×10^{-6}	High frequency cutoff (33 minutes)
`MIN_DISTANCE_KM`	50	Minimum station separation
`MAX_DISTANCE_KM`	13,000	Maximum station separation
`N_BINS`	40	Number of distance bins
`MIN_BIN_COUNT`	10	Minimum pairs per bin
`NOISE_THRESHOLD_NS`	50	Station quality filter

8.5 Dependencies

8.5.1 Python Requirements

```
# requirements.txt
numpy>=1.24.0
scipy>=1.10.0
matplotlib>=3.7.0
tqdm>=4.65.0
requests>=2.28.0
```

8.5.2 External Software

- RTKLIB: v2.4.3 or later (github.com/tomojitakasu/RTKLIB)
- Python: 3.10 or later
- Node.js: 18+ (for site building only)

8.6 Output Files

8.6.1 JSON Results

The primary analysis output is a JSON file containing all fit parameters, statistics, and metadata:

```
{
  "clock_bias": {
    "correlation_length_km": [X],
    "correlation_length_err_km": [Y],
    "amplitude": [A],
    "offset": [C0],
    "r_squared": [R2]
  },
  "clock_drift": { ... },
  "pos_jitter": { ... },
  "metadata": {
    "n_stations": [N],
    "n_pairs": [N],
    "date_range": "[START] to [END]"
  }
}
```

8.6.2 Figures

Generated figures are saved to `results/figures/`:

- `step_2_0_clock_bias.png` — Clock bias coherence vs distance
- `step_2_0_clock_drift.png` — Clock drift coherence vs distance
- `step_2_0_pos_jitter.png` — Position jitter coherence vs distance
- `step_2_0_summary.png` — Combined summary figure

8.7 Quick Start

Reproduce in 5 Steps

1. Clone the repository: `git clone https://github.com/matthewsmawfield/TEP-GNSS-RINEX`
2. Install dependencies: `pip install -r requirements.txt`
3. Install RTKLIB and ensure `rnx2rtkp` is in PATH
4. Run data acquisition: `python scripts/steps/step_1_0_data_acquisition.py`
5. Run analysis: `python scripts/steps/step_2_0_raw_spp_analysis.py`

Results will be generated in `results/outputs/` and `results/figures/`.

8.8 Citation

If you use this analysis package, please cite:

```
@article{smawfield2025rinex,
  title={Global Time Echoes: Raw RINEX Consistency Test},
  author={Smawfield, Matthew Lukin},
  journal={Preprint},
  year={2025},
  doi={10.5281/zenodo.17860166},
  url={https://matthewsmawfield.github.io/TEP-GNSS-RINEX/}
}
```

References & Contact

References

Burde, G. I. (2016). Special relativity with a preferred frame and the relativity principle: Cosmological implications. *arXiv*:1610.08771. arxiv.org/abs/1610.08771

Burrage, C., & Sakstein, J. (2018). Tests of chameleon gravity. *Living Reviews in Relativity*, 21, 1. doi:10.1007/s41114-018-0011-x

Consoli, M., & Pluchino, A. (2021). The CMB, preferred reference system and dragging of light in the Earth frame. *Universe*, 7(8), 311. doi:10.3390/universe7080311

Kaplan, E. D., & Hegarty, C. J. (2017). *Understanding GPS/GNSS: Principles and Applications* (3rd ed.). Artech House.

Lee, J., & Lee, J. (2019). Correlation between ionospheric spatial decorrelation and space weather intensity for safety-critical differential GNSS systems. *Sensors*, 19(9), 2127. doi:10.3390/s19092127

Lisdat, C., et al. (2016). A clock network for geodesy and fundamental science. *Nature Communications*, 7, 12443. doi:10.1038/ncomms12443

Menvielle, M., & Berthelier, A. (1991). The K-derived planetary indices: Description and availability. *Reviews of Geophysics*, 29(3), 415-432. doi:10.1029/91RG00994

Misra, P., & Enge, P. (2011). *Global Positioning System: Signals, Measurements, and Performance* (2nd ed.). Ganga-Jamuna Press.

Wang, N., Li, Z., Yuan, Y., & Huo, X. (2022). On the global ionospheric diurnal double maxima based on GPS vertical total electron content. *Journal of Space Weather and Space Climate*, 12, 4. doi:10.1051/swsc/2022002

Wcisło, P., et al. (2018). New bounds on dark matter coupling from a global network of optical atomic clocks. *Science Advances*, 4(12), eaau4869. doi:10.1126/sciadv.aau4869

TEP-GNSS Research Series

Smawfield, M. L. (2025). *Temporal Equivalence Principle: Dynamic Time & Emergent Light Speed*. Preprint v0.8 (Jakarta). Zenodo. DOI: 10.5281/zenodo.16921911 (Paper 0)

Smawfield, M. L. (2025). *Global Time Echoes: Distance-Structured Correlations in GNSS Clocks*. Preprint v0.25 (Jaipur). Zenodo. DOI: 10.5281/zenodo.17127229 (Paper 1)

Smawfield, M. L. (2025). *Global Time Echoes: 25-Year Analysis of CODE Precise Clock Products*. Preprint v0.18 (Cairo). Zenodo. DOI: 10.5281/zenodo.17517141 (Paper 2)

Smawfield, M. L. (2025). *Global Time Echoes: Raw RINEX Consistency Test*. Preprint v0.5 (Kathmandu). Zenodo. DOI: 10.5281/zenodo.17860166 (Paper 3 — this work)

Smawfield, M. L. (2025). *Temporal-Spatial Coupling in Gravitational Lensing: A Reinterpretation of Dark Matter Observations*. Preprint v0.5 (Tortola). Zenodo. DOI: 10.5281/zenodo.17982540 (Paper 4)

Smawfield, M. L. (2025). *Global Time Echoes: Empirical Synthesis*. Preprint v0.4 (Singapore). Zenodo. DOI: 10.5281/zenodo.18004832 (Paper 5)

Smawfield, M. L. (2025). *Universal Critical Density: Cross-Scale Consistency of ρ_T*. Preprint v0.3 (New Delhi). Zenodo. DOI: 10.5281/zenodo.18064365 (Paper 6)

Smawfield, M. L. (2025). *The Soliton Wake: Exploring RBH-1 as a Temporal Topology Candidate*. Preprint v0.3 (Blantyre). Zenodo. DOI: 10.5281/zenodo.18059250 (Paper 7)

Smawfield, M. L. (2025). *Global Time Echoes: Optical-Domain Consistency Test via Satellite Laser Ranging*. Preprint v0.3 (Mombasa). Zenodo. DOI: 10.5281/zenodo.18064581 (Paper 8)

Smawfield, M. L. (2025). *What Do Precision Tests of General Relativity Actually Measure?*. Preprint v0.3 (Istanbul). Zenodo. DOI: 10.5281/zenodo.18109760 (Paper 9)

Smawfield, M. L. (2026). *Temporal Equivalence Principle: Suppressed Density Scaling in Globular Cluster Pulsars*. Preprint v0.6 (Caracas). Zenodo. DOI: 10.5281/zenodo.18165798 (Paper 10)

Smawfield, M. L. (2026). *The Cepheid Bias: Resolving the Hubble Tension*. Preprint v0.6 (Kingston upon Hull). Zenodo. DOI: 10.5281/zenodo.18209702 (Paper 11)

Smawfield, M. L. (2026). *Temporal Equivalence Principle: A Unified Resolution to the JWST High-Redshift Anomalies*. Preprint v0.4 (Kos). Zenodo. DOI: 10.5281/zenodo.19000827 (Paper 12)

Smawfield, M. L. (2026). *Temporal Equivalence Principle: Temporal Shear Recovery in Gaia DR3 Wide Binaries*. Preprint v0.3 (Kilifi). Zenodo. DOI: 10.5281/zenodo.19102061 (Paper 13)

Supporting References

Data Sources & Software

NASA CDDIS (2024). Crustal Dynamics Data Information System. NASA Goddard Space Flight Center. cddis.nasa.gov

International GNSS Service (IGS). Multi-GNSS Experiment (MGEX). igs.org/mgex/

Takasu, T. (2013). RTKLIB: An Open Source Program Package for GNSS Positioning. github.com/tomojitakasu/RTKLIB

GNSS Processing

Dach, R., Lutz, S., Walser, P., & Fridez, P. (Eds.) (2015). Bernese GNSS Software Version 5.2. Astronomical Institute, University of Bern.

Kouba, J. (2009). A guide to using International GNSS Service (IGS) products. *Geodetic Survey Division, Natural Resources Canada*.

IGS Analysis Center Coordinator. (2024). CODE Analysis Products. aiub.unibe.ch

IGS RINEX Working Group (2020). RINEX: The Receiver Independent Exchange Format, Version 3.05. IGS Format Documentation

Signal Processing & Geodesy

Welch, P. D. (1967). The use of fast Fourier transform for the estimation of power spectra. *IEEE Transactions on Audio and Electroacoustics*, 15(2), 70-73.

Oppenheim, A. V., & Schafer, R. W. (2010). *Discrete-Time Signal Processing* (3rd ed.). Pearson.

Hofmann-Wellenhof, B., Lichtenegger, H., & Wasle, E. (2007). *GNSS – Global Navigation Satellite Systems: GPS, GLONASS, Galileo, and More*. Springer.

Ray, J., Altamimi, Z., Collilieux, X., & van Dam, T. (2008). Anomalous harmonics in the spectra of GPS position estimates. *GPS Solutions*, 12(1), 55–64. doi:10.1007/s10291-007-0067-7

Rebischung, P., & Gobron, K. (2024). Modeling random isotropic vector fields on the sphere: theory and application to the noise in GNSS station position time series. *Journal of Geodesy*, 98, 79. doi:10.1007/s00190-024-01859-z

Saastamoinen, J. (1972). Atmospheric correction for the troposphere and stratosphere in radio ranging of satellites. *The Use of Artificial Satellites for Geodesy*, Geophysical Monograph 15, 247-251.

Santamaría-Gómez, A., & Ray, J. (2021). Chameleonic Noise in GPS Position Time Series. *Journal of Geophysical Research: Solid Earth*, 126(2), e2020JB019541. doi:10.1029/2020JB019541

Gobron, K., Rebischung, P., Van Camp, M., Demoulin, A., & de Viron, O. (2024). Spatial correlations of GNSS position time series: Application to the EUREF network. *Journal of Geodesy*, 98, 48. doi:10.1007/s00190-024-01848-3

Niu, Y., Wei, N., Li, M., Rebischung, P., Shi, C., & Chen, G. (2023). Quantifying discrepancies in the geometric and physical components of GNSS station coordinate time series. *Journal of Geodesy*, 97, 68. doi:10.1007/s00190-023-01756-4

Kreemer, C., & Blewitt, G. (2021). Robust estimation of spatially varying common-mode components in GPS time-series. *Journal of Geodesy*, 95, 13. doi:10.1007/s00190-020-01466-5

He, X., Yu, K., Montillet, J.-P., Xiong, C., Lu, T., Zhou, S., Ma, X., Cui, H., & Ming, F. (2021). GNSS-TS-NRS: An Open-Source MATLAB-Based GNSS Time Series Noise Reduction Software. *Remote Sensing*, 13(21), 4392. doi:10.3390/rs13214392

Klobuchar, J. A. (1987). Ionospheric time-delay algorithm for single-frequency GPS users. *IEEE Transactions on Aerospace and Electronic Systems*, AES-23(3), 325-331.

Contact Information

Author: Matthew Lukin Smawfield

Email: matthew@mlsmawfield.com

ORCID: 0009-0003-8219-3159

GitHub: github.com/matthewsmawfield

Related Projects

- *Paper 1 (Multi-Center): TEP-GNSS*
- *Paper 2 (25-Year CODE): TEP-GNSS-II*
- *Paper 3 (Raw RINEX): TEP-GNSS-RINEX (this paper)*

Code Repositories

- *TEP-GNSS (Papers 1 & 2): github.com/matthewsmawfield/TEP-GNSS*
- *TEP-GNSS-RINEX (Paper 3): github.com/matthewsmawfield/TEP-GNSS-RINEX*

Version: v0.5 (Kathmandu) · Last updated: 29 April 2026 · Originally published: 9 December 2025